AUTONOMOUS UNLOADING SYSTEM FOR HEAD-FEEDING COMBINE ROBOT

HIROKI KURITA

2013

Laboratory of Field Robotics

Division of Environmental Science and Technology

Graduate School of Agriculture

Kyoto University

ABSTRACT

This dissertation discusses the development of an autonomous unloading system for a head-feeding combine harvester. To provide an overview of this research and its contribution, a brief summary is given below; based on the keywords: *head-feeding combine harvester*, *combine robot*, *unloading operation*, *unloading auger*, *spout*, *visual servoing*, *fiducial marker*, *ARToolKit*, *inverse kinematics*, *fiducial marker searching*, *autonomous unloading system*.

A *head-feeding combine harvester* is a specialized agricultural machine, developed in Japan, for harvesting rice. Automation of agricultural processes has attracted the attention of researchers' for a long time. Recent progress in the development and availability of navigation systems has fostered rapid progress in automated agricultural vehicles. With regard to the head-feeding combine, to date a few prototypes have been developed with robotic operations. The project team at the Laboratory of Field Robotics, Kyoto University, has been engaged in one such development of a *combine robot*; they have demonstrated that such a robot can autonomously travel along the target path with sufficient accuracy and that it can successfully harvest rice crops.

Such a combine robot will also be required to autonomously perform the *unloading operation*; discharge the grain from its grain tank to a grain container via its *unloading auger*. There are several challenges to automate this unloading operation: The combine robot has to detect the grain container and determine and adjust with sensory devices its positional relationship to the grain container. Based on its relative position, the combine will then need to control its unloading auger in such a way that the *spout* from the unloading auger is positioned at an appropriate point to unload grain directly into the container without any spillage or loss.

The project team has addressed these challenges with *visual servoing* techniques. A machine vision system was developed in which a USB camera was used as the sensor. A planar board was set up on the grain container as a *fiducial marker* to establish the relative position of the combine augur to the board using image processing algorithms from the *ARToolKit* software library. By identifying the position of the grain container; the augur of the combine harvester can be programmed to adjust its position relative to the container. The unloading auger was then modeled as a robot manipulator. The target state of the unloading

auger was determined by *inverse kinematics*. Experimental results have shown that the positioning accuracy, based on this developed machine vision system, was within desired specifications.

The combine robot needs to efficiently search for and accurately determine the position of the fiducial marker. To optimize *fiducial marker searching*, the field of view of the auger camera was numerically simulated. Based on the simulation results, a camera was installed at the optimal position on the combine robot, enabling an efficient search procedure to be implemented. Subsequent experimental results have shown that the combine robot can efficiently search for and accurately detect the position of the fiducial marker.

For actual paddy field applications, a new machine-vision based positioning method was proposed. Experimental results have shown that the combine robot can accurately position its spout to the appropriate three-dimensional target point. These developments were then integrated into an *autonomous unloading system*, and field tested in actual rice paddy fields, to verify the performance of the proposed system. Results from these field tests demonstrate that an autonomous unloading system has been successfully developed.

ACKNOWLEDGEMENTS

First of all, the author expresses his utmost gratitude and appreciation to his supervisor Dr. Michihisa IIDA, Professor of Laboratory of Field Robotics, Kyoto University, for his valuable and thoughtful guidance, advice, encouragement and patience in the duration of the author's research.

The author also expresses his grateful thanks to the dissertation committee, Dr. Naoshi KONDO, Professor of Kyoto University and Dr. Hiroshi SHIMIZU, Professor of Kyoto University, for their suggestive and helpful comments.

The author expresses his sincere gratitude to Dr. Mikio UMEDA, Emeritus Professor of Kyoto University, for his kind and comprehensive guidance in the duration of bachelor program and master's program of the author.

The author wishes to express his deep gratitude to Dr. Masahiko SUGURI, Assistant Professor of Kyoto University and Mr. Ryohei MASUDA, Assistant Professor of Kyoto University, for their helpful suggestion and advice on this research. The author thanks Dr. Chan-Seok RYU, who was formerly the senior member of Laboratory of Field Robotics and had been promoted to Associate Professor of Geyongsang National University, Korea, for the various advices on the research and on the whole academic life.

The author would like to show his sincere appreciation to Dr. Garry PILLER, Professor of Kyoto University and to Dr. Josse DE BAERDEMAEKER, Professor of Katholieke Universiteit Leuven. They kindly spared their precious time and energy to proofread the manuscript and managed to polish the English expressions in this thesis.

The author shows his appreciation to Dr. Katsuhiko TAMAKI, Chief Researcher of Farm Mechanization Division, National Agricultural Research Center (NARC), Dr. Masahiro SAITO, Senior Researcher of Farm Mechanization Division, NARC, and the other researchers who belong to Farm Mechanization Division of NARC for their critical comments on this research. The author also shows his appreciation to Dr. Kazuyoshi NONAMI, the manager of research and experimental department of Mitsubishi agricultural machinery Co., Ltd, for providing the technical information on the combine harvester used in this research.

The author expresses his deep sense of gratitude to all of the members in Laboratory of Field Robotics, Kyoto University. Ms. Masami KUBO, the secretary of the laboratory, always cared about the author and helped his academic life. The author shared joys and sorrows with his two comrades: Mr. Hiroyuki ONOYAMA always helped the author with his logical thinking and cheered up the author with his humor and illimitable appetite. Mr. Wonjae CHO helped the author with his deep insight into machine vision and his brilliant programming skill. The author strongly hopes that they may complete their researches and finish their doctoral programs successfully. Mr. Ryo UCHIDA and Mr. Huaping ZHU, students of the laboratory, made a great contribution for the completion of this research. The author also expresses his deep gratitude to the other laboratory members, past and present, especially to Ryo SASAKI, for their help in his study and school life.

Finally, the author expresses his heartfelt gratitude and highest respect to his father, Nishiki KURITA and his mother, Yukari KURITA. What the author is today, he owes to them. The author also wishes to express his deep gratitude to other family members; his grandfathers, Ryoshun HANAOKA, Kaijo HIROKAWA and Keisai KURITA; his grandmothers, Yoshie HANAOKA, Fujiko HIROKAWA and Mizue KURITA; his brother, Yoshihiro; his sisters, Mayako and Yu; his little nieces, Hino and Hana. Without their help, this dissertation would have never been completed.

CONTENTS

NOMENCLATURE

Symbol	*Denotation*	*Chapter*
η	steering control	2
ϕ_k	heading angle	2
d_k	lateral error	2
ϕ_{dk}	heading error	2
v_k	travelling speed	2
ψ_k	orientation error from the point to be reached 1 s later (see Fig. 2.8)	2
k_1, k_2	control gain	2
L_1, L_2	lateral distance before and after first 45° turning	2
(c, u, v)	image coordinate system	3
(O, U, V, W)	Euclidean world coordinate system	3
(O_c, U_c, V_c, W_c)	camera-based coordinate system	3
(O_b, U_b, V_b, W_b)	calibration board-based coordinate system	3
s	scale factor	3
$\boldsymbol{P}$	perspective projection matrix	3
$\boldsymbol{K}$	camera's internal parameters matrix	3
f	focal length	3
k_u, k_v	scale factor	3
s_k	skew factor	3
u_0, v_0	coordinates of the optical center	3
$\boldsymbol{R}$	rotation matrix	3
$\boldsymbol{t}$	translation vector, $[t_u, t_v, t_w]^T$	3
a_1, a_2, b_1, b_2	coefficients of fitted line	3
P_{ij}	(i, j) entry of matrix $\boldsymbol{K}$	3
$\boldsymbol{n}_1$, $\boldsymbol{n}_2$	normal vector of a plane including fitted lines	3
$\boldsymbol{V}_1$, $\boldsymbol{V}_2$	outer product of a pair of normal vectors	3

Symbol	*Denotation*	*Chapter*
$\boldsymbol{v}_1$, $\boldsymbol{v}_2$	unit vector of $\boldsymbol{V}_1$, $\boldsymbol{V}_2$	3
$[U_i', V_i', W_i']^T$	i th vertices' coordinates of the fiducial marker	3
$[U_i, V_i, W_i]^T$	coordinates of $[U_i', V_i', W_i']^T$ after rotation	3
$[u_i, v_i]^T$	projection of vertices onto image plane	3
Σ_0, Σ_1, Σ_2	coordinate system assigned on combine	3, 4, 5
Σ_{Camera}	coordinate system assigned on camera	3
Σ_{Marker}	coordinate system assigned on fiducial marker	3, 5
θ_1, θ_2	joint angle of unloading auger	3, 4, 5
l_a, l_b, l_c, l_d, l_e	offset distance	3, 4, 5
${}^n\boldsymbol{T}_m$	homogeneous transformation matrix from Σ_m to Σ_n	3, 5
${}^n\boldsymbol{r}_{\boldsymbol{m}}$	position vector of point $\boldsymbol{m}$ on Σ_n	3, 5
α	camera's elevation angle	3, 4
$[x_0, y_0, z_0]^T$	abbreviation of ${}^0\boldsymbol{r}_{Spout}$	3, 5
h_{fr}	height of farm road from paddy ground	4
h_c	height of Joint 1	4
h_{kt}	height of pickup truck (roof)	4
D	depth of field ($D_{min} < D < D_{max}$)	4
L_{min}, L_{maj}, Y_{min}, Y_{maj}, β, γ, γ', δ, y_c	see Fig. 4.4-(a) and Fig. 4.6-(a)	4
Y_1, Y_2, $H(\theta_2)$, $F(\theta_2)$, Δl, l_Δ	see Fig. 4.4-(b) and Fig. 4.6-(b)	4
X_{min}, X_{maj}	see Fig. 4.5	4
ϕ_V, ϕ_H	half of vertical and horizontal AOV	4
ΔL	forward traveling distance	5
Σ_0'	coordinate system on combine after forward traveling	5
${}^{0'}\boldsymbol{r}_{\boldsymbol{m}}$	position vector of point $\boldsymbol{m}$ on Σ_0'	5
$\tilde{\theta}_1$, $\tilde{\theta}_2$	estimated proper joint angle after forward traveling	5
Z_{Error}	estimated positioning error in vertical direction	5
ε	acceptable error in vertical direction	5

ABBREVIATION

MAFF	Ministry of Agriculture, Forestry and Fisheries
GPS	Global Positioning System
INS	Inertia Navigation System
RTK-GPS	Real-Time Kinematic GPS
HST	Hydrostatic Transmission
VRS	Virtual Reference Station
PDA	Personal Digital Assistance
GNSS	Global Navigation Satellite System
ECU	Electric Control Unit
DBW	Drive-By-Wire
PC	Personal Computer
CAN	Control Area Network
PWM	Pulse Width Modulation
R/C SW	Radio Control Switch
RMSE	Root Mean Square Errors
3D	Three-Dimensional
2D	Two-Dimensional
ADC	Analogue-to-Digital Converter
DOF	Degree Of Freedom
USB	Universal Serial Bus
FOV	Field Of View
AOV	Angle Of View
SURF	Speeded-Up Robust Features

LIST OF TABLES

LIST OF FIGURES

No.	Title	Page

No.	Title	Page

AUTONOMOUS UNLOADING SYSTEM FOR HEAD-FEEDING COMBINE ROBOT

CHAPTER 1

GENERAL INTRODUCTION

1.1. Background

Research and development of agricultural machinery in Japan has led to the introduction of mechanized systems and a reduction in working hours, especially in rice cultivation [1]. The main purpose of this research has been to make agricultural work quicker and lighter.

Figure 1.1 illustrates trends in the population and average age of farmers in Japan. Currently the situation in Japan is one where fewer workers are engaged in agriculture and those who are engaged, are aging rapidly [2]-[4]. The food self-sufficiency rate in Japan remains low compared to other developed countries, as shown in Fig. 1.2. and 1.3 [5]. Moreover, the Japanese government is being pressured to accept agricultural free trade agreements by foreign countries. Recently, the Japanese government has been discussing participating in talks on the Trans-Pacific Partnership (TPP); a proposed huge free-trade area around the Pacific Rim. Free trade has been a hot issue since the 1980s and it will remain a point of discussion over the next decades. Nevertheless, it is quite certain that there exists a slow but steady trend from *protective* trade to *liberal* trade. Thus, Japanese agriculture will be increasingly exposed to harsher global competition.

It will be necessary for Japanese agriculture to improve agricultural productivity in order to meet these challenges. Field robots in agriculture will play an important role in improving the efficiency of agricultural operations and alleviating the shortages in the workforce.

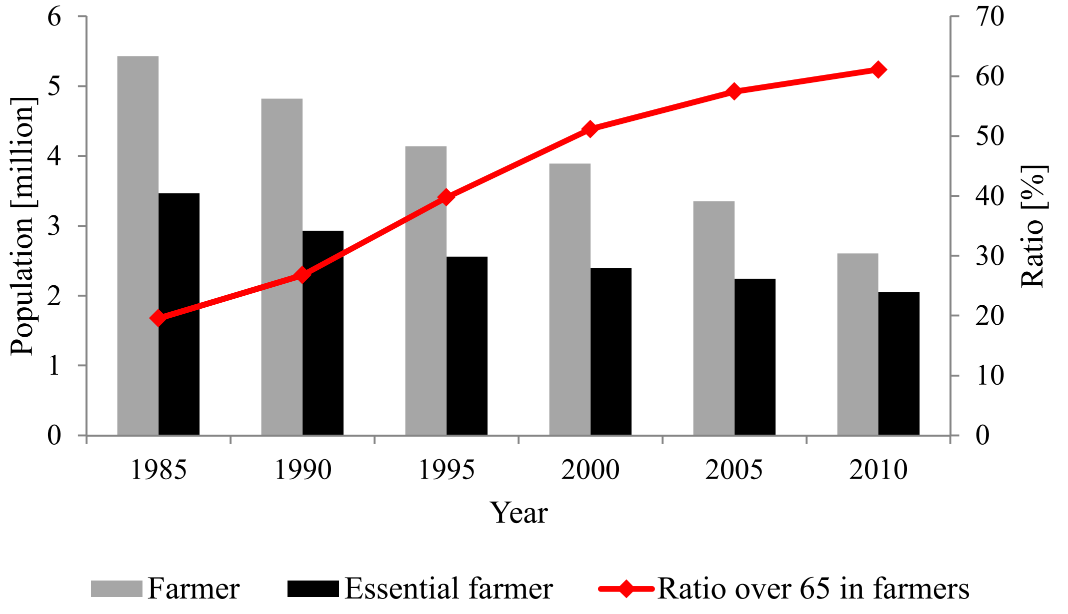

Fig. 1.1. Workforce trend in Japanese agriculture [2]-[4].

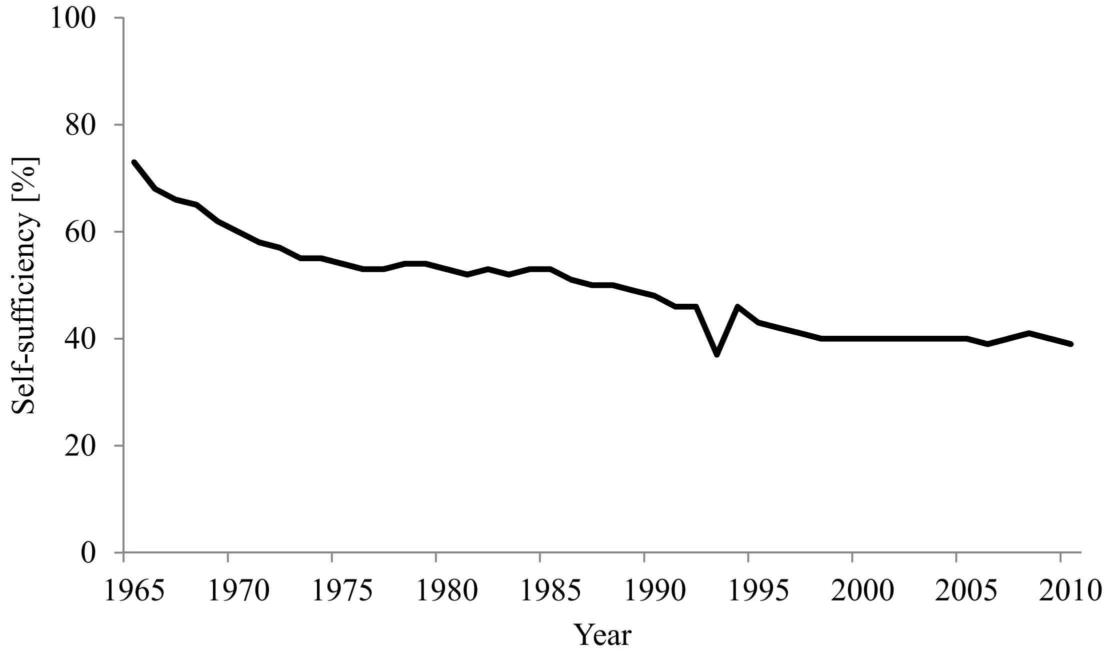

Fig. 1.2. Self-sufficiency of Japan in food (calorie base) [5].

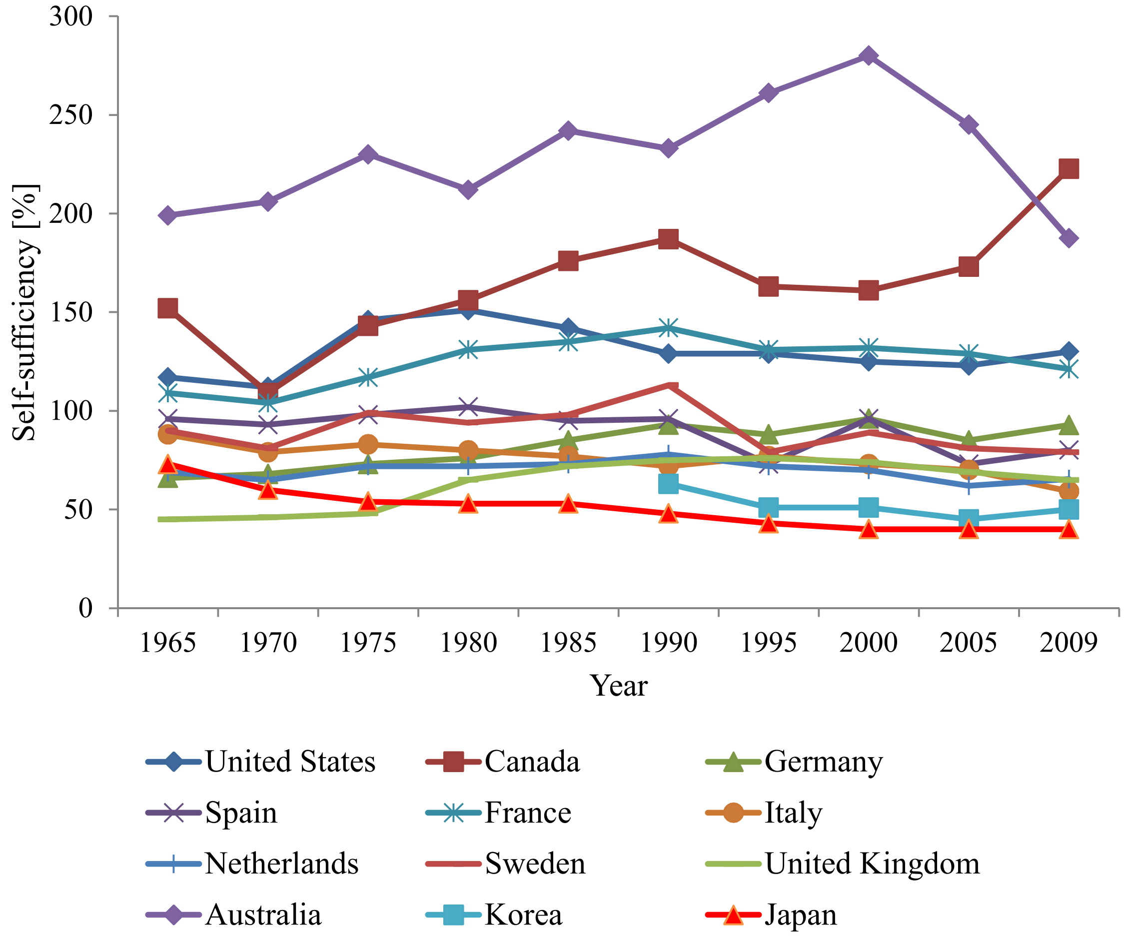

Fig. 1.3. Self-sufficiency of developed countries in food (calorie base) [5].

In fact, Japanese agriculture has two different aspects, depending on the region (see Fig. 1.4). In Hokkaido, the large northern island of Japan, farm households cultivate, on average, an area of 22.34 ha [4]. The dominant crops are rice, wheat, potato, soybeans, and so on [6]. Large-sized tractors and conventional combine harvesters are mainly used in this region. In other words, agriculture in Hokkaido resembles Western style, large-scale agriculture. On the other hand, in the rest of the Japanese Archipelago, farm households cultivate just 1.49 ha on average [4]. Around 62% of the arable land is utilized for rice paddy fields, and the rest for various other crops [4]. These fields are usually small and dispersed widely. These small fields cannot bear heavy or large sized agricultural machinery. For this reason, relatively small-sized agricultural machinery is used in most parts of Japan.

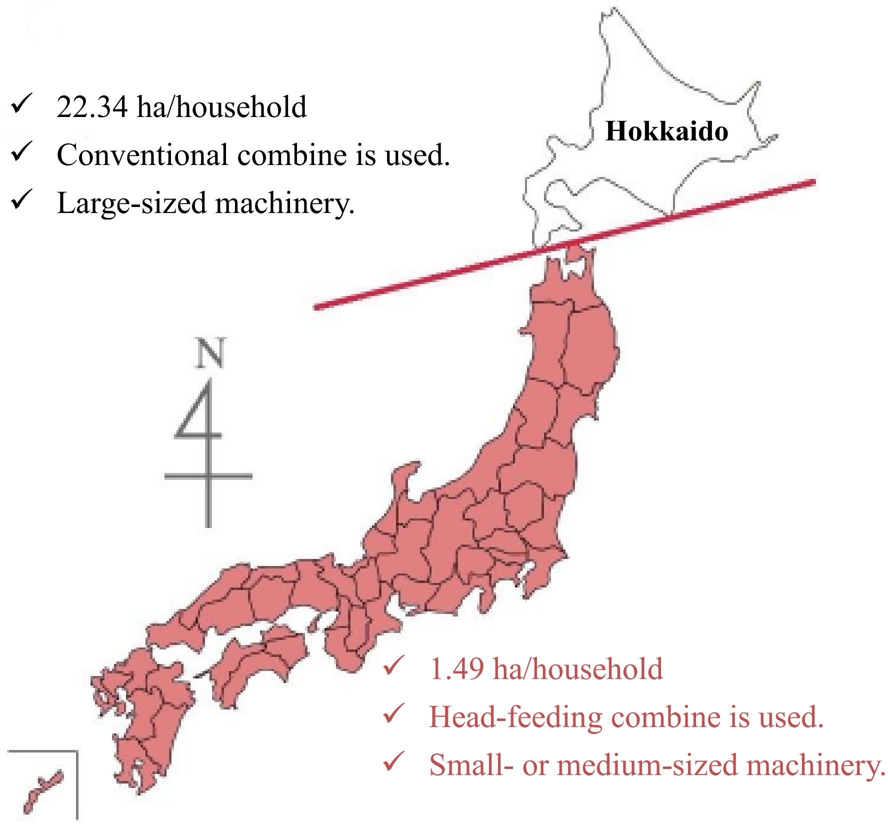

Fig. 1.4. Two aspects of Japanese agriculture.

To ensure sustainability of Japanese agriculture into the future, the following strategies are required: 1) aggregation of farmland, 2) development of robotic and automated systems and 3) introduction of new technologies. To realize a more competitive agricultural industry, it will be necessary to aggregate agricultural land and to increase the cultivation of crops by robots and automated machines; this is because the farmer population continues to decline. In addition, it is also important to efficiently automate approaches to agricultural work, even those operations that rely on farmer's skill and experience gained over time, in order to simplify the entry of potential, young farmers into agriculture. Thus, further development of automated agricultural machinery in Japan is becoming of even greater importance [7]-[10]. Hence, the Ministry of Agriculture, Forestry and Fisheries (MAFF) in Japan is promoting research projects on agricultural robots. In these projects, advanced robotic farming systems will be developed by combining field robots and the internet. We have taken part in robotizing a head-feeding combine harvester (hereafter referred to as a combine) that is used to harvest rice and wheat in small-sized fields.

1.2. Advanced Robotic Farming System

As mentioned above, it will be important in the future that a small number of farmers can cultivate crops by field robots in many small and dispersed fields. For this purpose, numerous agricultural robots, such as tractors, rice transplanters, and combine have been developed. The tractor robot autonomously tills the field, and then the rice transplanter robot plants rice seedlings in the field. At harvest time, a combine robot will harvest rice automatically. These robots will need navigation sensors, such as a global positioning system (GPS) and an inertia navigation system (INS), so they can automatically travel along a target path. Thus, the farmer will be able to simultaneously operate multiple robots.

The combine robot will offer a more labor-saving harvesting system, especially for these dispersed fields. Figure 1.5 shows a conceptual diagram of an integrated harvesting system [7].

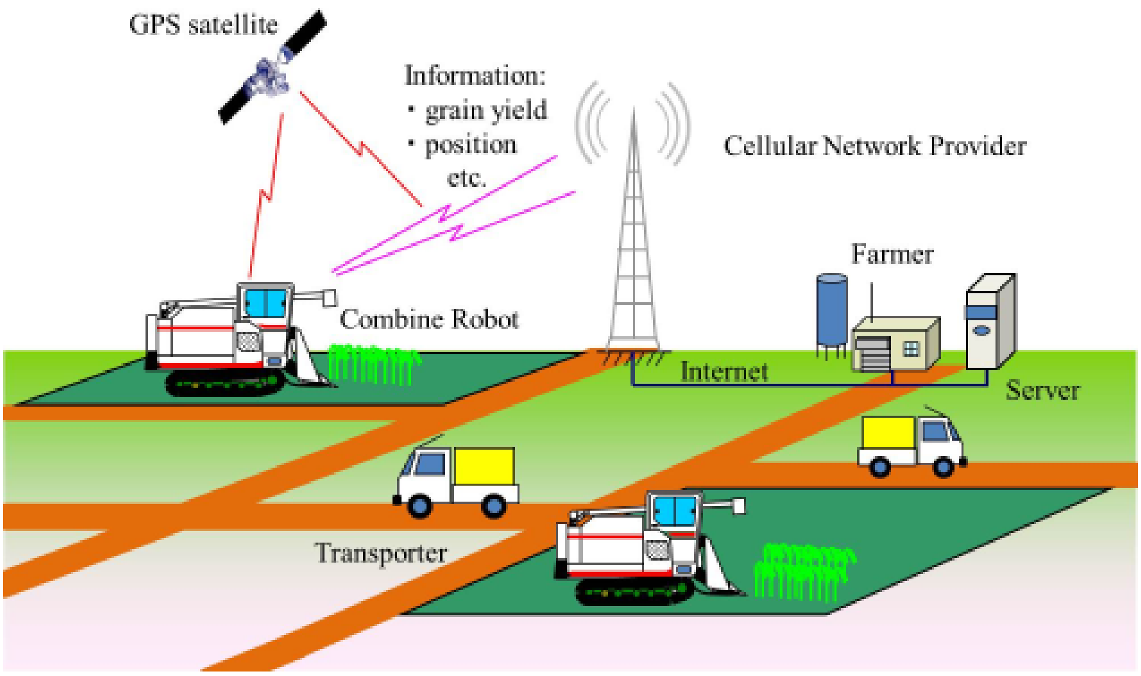

Fig. 1.5. Conceptual diagram of integrated harvesting system.

This system consists of a combine robot and a grain transporter. Fewer farmers will be required to manage the system, since the combine robot is expected to perform most of field harvesting operations automatically. Farmers will be able to obtain an overview and detailed information about each component in the system, such as operating efficiency, grain yield, the status of the machine, and so on through the internet. This will free farmers from tedious operations; so they can pay most of their attention to the management of the system, and not to the operation of the individual machines.

Currently, the combine robot can harvest rice crops while it is autonomously travelling along a target path in the field. However, human operators are needed to manually unload the grain from combine grain tank when it is full into a separate grain storage container. In order to fully automate the harvesting operation, it will be necessary for the robot to unload grain autonomously. If the combine robot can unload grain autonomously, it will be able to harvest an entire field crop without the help of the farmer. Therefore, this study aims to develop an autonomous unloading system for the combine robot using machine vision.

1.3. Unloading Operation

During actual rice harvest operations in the paddy field, grain is unloaded into a separate grain container when the grain storage tank in the combine harvester becomes full. The grain storage container is generally mounted on a pickup truck parked beside the paddy. After this unloading operation is completed, the grain is transported to a local rice-processing facility, such as a rice center or a rice dryer facility. Figure 1.6 shows a typical scene of the unloading operation being performed by farmers.

Usually, two workers are engaged in this process: one as an operator of the combine and the other as the truck driver. During the unloading operation, the operator parks the combine beside the pickup truck with the grain storage container mounted on the back, and then he maneuvers the unloading auger of the combine above the grain storage container, and discharges the grain into the container. After that, he resumes harvesting the remaining rice crop. Meanwhile, the driver transports the grain to a rice-processing facility; usually located nearby. If this process is being performed by only one worker, each time he transports the grain to the facility he must stop harvesting. A combine robot would enable a worker to simultaneously manage the harvesting and transport the harvested grain, thus halving the person hours involved in this operation. In the context of the integrated harvesting system mentioned in Section 1.1, the harvesting and unloading operation would be performed by combine robots, while a driver would transport the grain from the field to the rice-processing facility.

In addition, a skilled operator is required to quickly, and accurately position the auger to an appropriate point above the storage container. Thus, automation of the unloading process is important not only for reducing the manual labor required, but also for the need for a skilled operator. Consequently, an automatic unloading system would reduce the workload and operate the machine safely, without the need for a skilled and experienced operator.

Fig. 1.6. Unloading operation.

1.4. Objectives and Overview

This research aims to develop an autonomous unloading system for a head-feeding combine robot. The objectives of this thesis are as follows:

1. To provide an overview of the head-feeding combine robot used in this research.

2. To develop a control system for the unloading auger, and image processing algorithms for the detection of the grain storage container.

3. To optimize camera positioning, so as to cover as wider a field of view as possible.

4. To actually demonstrate in field conditions a working, autonomous, unloading system.

The contents of each chapter are briefly described below.

The development of a head-feeding combine robot and prototype specifications are explained in Chapter 2. This will determine the platform on which the autonomous unloading system is to be installed. In order to develop an autonomous unloading system, the machine-vision arrangement to be used is presented in Chapter 3. This is necessary in order to obtain the target joint angles for the unloading auger. The arrangement or method utilises a planar fiducial marker for estimating the relative position between the combine and the grain storage container, into which the grain will be unloaded. The kinematic model of the unloading auger is also discussed. The challenges involved in searching for the fiducial marker are discussed in Chapter 4. Then, in a further iteration, the method presented in Chapter 3 is modified for more accurate and practical spout positioning. The presented methods are integrated into an autonomous unloading system and trialed under actual rice paddy field conditions. Details of this trial are discussed in Chapter 5. Finally, in Chapter 6 the conclusions of the thesis are outlined.

REFERENCES

[1] Tamaki, K: Agriculture and robot –from the past to the future-. Journal of Agricultural Science, Tokyo University of Agriculture, vol. 50, no. 4, 83-94, 2006.

[2] Ministry of Agriculture, Forestry and Fisheries: Annual Report on Food, Agriculture and Rural Areas in Japan, 2009 (Last accessed on 01/04/2013). http://www.maff.go.jp/e/annual_report/2009/index.html

[3] Ministry of Agriculture, Forestry and Fisheries: Report on Results of 2010 World Census of Agriculture and Forestry in Japan (Last accessed on 01/04/2013). http://www.e-stat.go.jp/SG1/estat/ListE.do?bid=000001037762&cycode=0

[4] The 86th Statistical Yearbook of Ministry of Agriculture, forestry and Fisheries (2010-2011) (Last accessed on 01/04/2013). http://www.maff.go.jp/e/tokei/kikaku/nenji_e/86nenji/index.html

[5] Ministry of Agriculture, Forestry and Fisheries: Self-sufficiency in the world (Last accessed on 01/04/2013). http://www.maff.go.jp/j/zyukyu/zikyu_ritu/013.html

[6] Corp acreage in Hokkaido 2006, (in Japanese) (Last accessed on 01/04/2013). http://www.pref.hokkaido.lg.jp/ns/nsk/nousakumotutoukei.htm

[7] Iida, M., Uchida, R., Zhu, H., Ohdoi, K., Suguri, M., Kurita, H., Masuda, R. and Inamura, T: Development of head-feeding combine robot. Proceedings of the 6th International Symposium on Machinery and Mechatronics for Agriculture and Biosystems Engineering (ISMAB) 2012, Jeonju, Korea, 2012.

[8] Noguchi, N. and Terao, H: Path planning of an agricultural mobile robot by neural network and genetic algorithm. Computers and Electronics in Agriculture vol. 18, issues 2-3, 187-204, 1997.

[9] Ishida, M., Imou, K., Okado, A., Takenaga, H., Honda, Y., Itokawa, N. and Shibuya, Y: Autonomous tractor for forage production. Journal of the Japanese Society of Agricultural Machinery vol. 60, no. 2, 59-66, 1998.

[10] Nagasaka, Y., Umeda, N., Kanetani, Y., Taniwaki, K. and Sasaki, Y: Automated rice transplanter using global positioning and gyroscopes. Computers and Electronics in Agriculture, vol. 43 issue 3, 223-234, 2004.

CHAPTER 2

GRAIN HARVESTING ROBOT

2.1. Introduction

Autonomous agricultural robots, which perform farming operations, have been developed in Japan for some decades now, such as the tractor robot [1], [2], the rice-transplanting robot [3], the combine robot [4]-[6], and the wagon robot [7]. These robots have a real-time kinematic global positioning system (RTK-GPS) and gyroscopes. The RTK-GPS is convenient and sufficiently accurate for navigating an agricultural robot along a target path. However, the heading angle for the robot cannot be accurately determined by GPS alone, thus, a gyroscope or a compass has typically been used to determine this.

This chapter reviews the head-feeding combine robot that has been developed by the Laboratory of Field Robotics, Kyoto University [8]. This robot is based on a commercially available four-row head-feeding combine harvester that has been remodeled to autonomously travel along a target path. For navigation sensors, this prototype is equipped with an RTK-GPS and a GPS compass. Steering and right-angle turning-control algorithms were developed to control the position and orientation of the combine with respect to the target path. In addition, a path planning algorithm has been developed that creates a counter-clockwise spiral path pattern for harvesting operations. Finally, harvest trials were conducted in a rice paddy field to examine the performance of the path-following controller of the combine robot. Before detailing the specifications of the combine robot, it would first be helpful to provide a brief introduction to the head-feeding combine harvester.

The harvester and the binder were independently developed. Both functions were then integrated into a self-propelled vehicle, known as a combine harvester [9]. In Japan, this evolved from the 1960s into a head-feeding combine harvester; a more specialized combine for rice harvesting [10]. The head-feeding combine can be roughly divided into a number of parts; namely, *pick-up*, *cutting*, *conveying*, *threshing*, *separating*, *cleaning* and *straw chopping devices* (see Fig. 2.1).

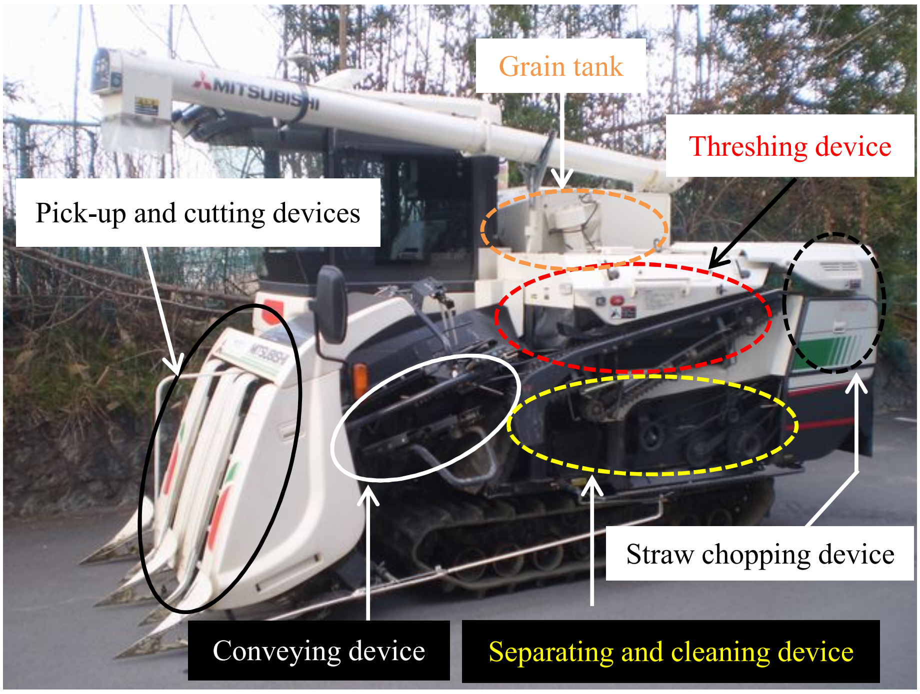

Fig. 2.1. Structure of head-feeding combine harvester.

During harvesting, the rice plants are first aligned by pick-up tines so as to keep their heads aligned and then the entire plants are cut with a *reciprocating cutter bar*. Figure 2.2 shows the main parts for conveying, threshing, separating and cleaning the cut rice. To keep the heads of the harvested rice plants aligned, they are held in place with chains and belts; their heads with *an upper conveying chain* (**a**) and the lower stalk with *a carrying chain of harvested crop bundle* (**b**). Next they are passed on to *a feed chain* (**c**) that holds only their lower stalks. Thus, rice plants enter the threshing device with their heads aligned, and only their heads are fed between *a threshing cylinder and a concave* and threshed with the teeth of *the threshing cylinder* (**d**). The threshed grain falls through the *concave* (**e**).

Figure 2.3 illustrates the threshing, separating and cleaning devices inside the combine.

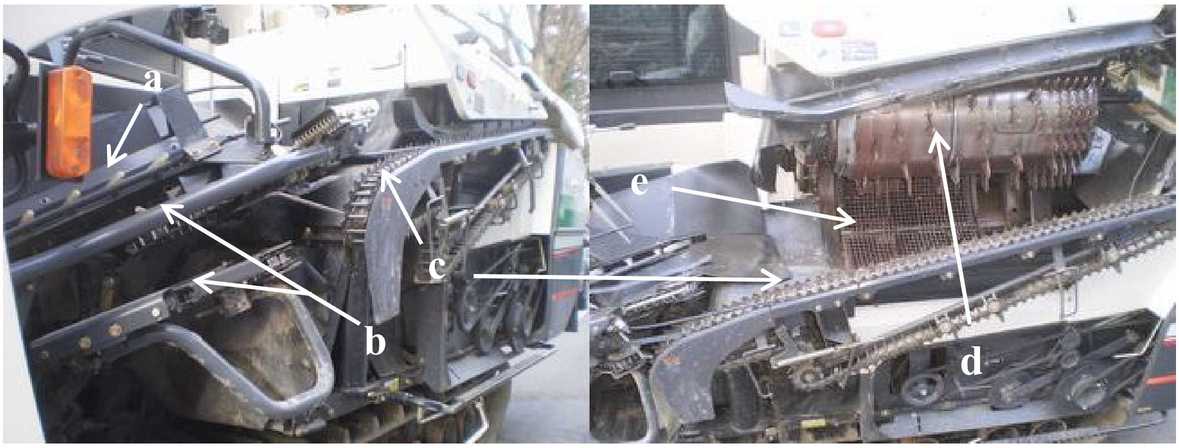

Fig. 2.2. Devices for conveying, threshing, separating and cleaning.

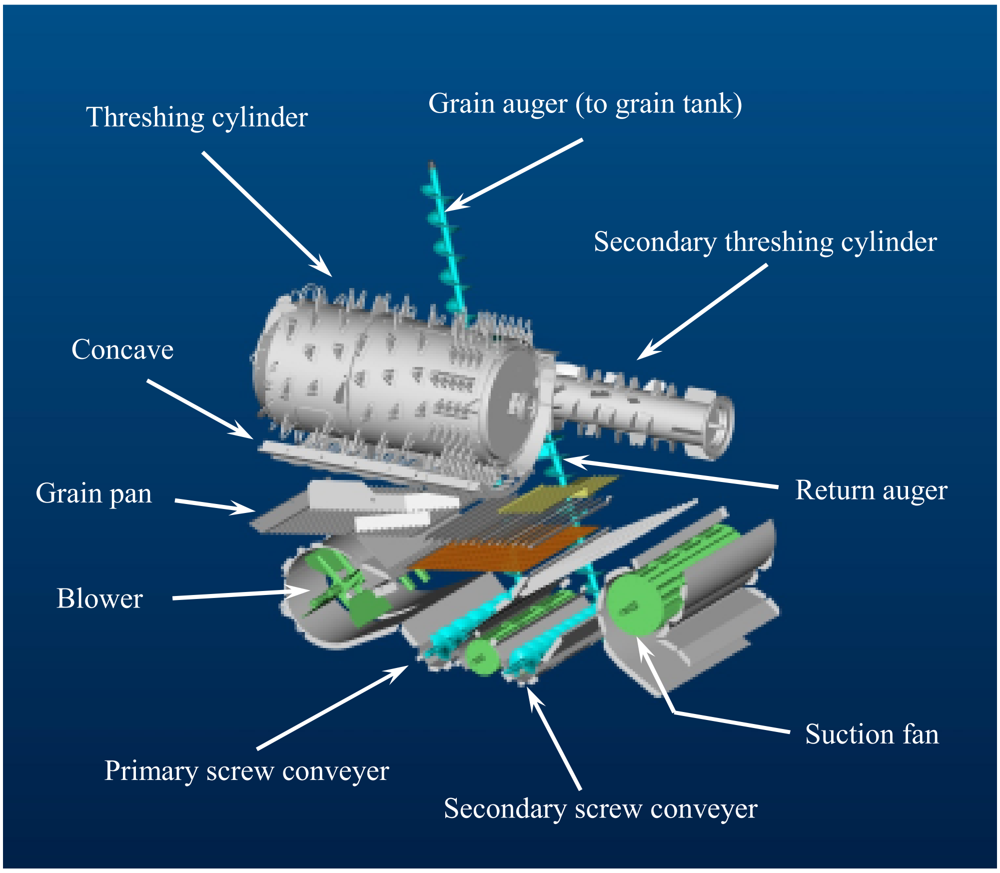

Fig. 2.3. Threshing, separating and cleaning devices inside combine harvester. (By courtesy of Mitsubishi Agricultural Co. Ltd.)

The threshed grain is then separated into fine grain and chaff by means of a grain pan, a blower, and a sieve. The rest of the threshed grain that cannot pass through the concave is directly sent to a secondary threshing device. Chaff is discharged from the machine and the remaining grain returned to the grain pan through a *return auger*. Finally, clean grain is sent to and stored in the grain tank (see Fig. 2.1).

According to a report [10], head-feeding combine harvesters have a high operating accuracy; less than 0.5% of grain is damaged and less than 3% of the grain is lost. And it is said that head-feeding combines are superior for rice harvesting, compared to conventional combine harvesters; there have 2 - 9% grain damage and 5 - 7% grain loss.

2.2. Combine Robot

2.2.1. Base Machine

Figure 2.4 shows an image of the combine robot, which is equipped with a RTK-GPS antenna and a GPS compass on its roof. The base machine used for the development of the combine robot is a four-row head-feeding combine (Mitsubishi Agricultural Machinery Co. Ltd., VY50CLAM).

Fig. 2.4. Head-feeding combine robot.

Table 2.1. Specifications of combine robot.

Model		VY50CLAM
Dimensions [mm]	Length	4,350
	Width	2,050
	Height	2,600
Weight [kg]		3,055
Engine	Type	4-cycle, water-cooled diesel
	Output [kW(PS)/rpm]	36(49)/2,800
Crawler track [mm]	Length	1,670
	Width	450
	Tread	1,030
Transmission Speed [m/s]	Low	0 - 0.88
	Middle	0 - 1.40
	High	0 - 2.28
Swath width [mm]		1,450 - 1,500
Grain tank [L]		1,500

In paddy fields in Japan, rice plants are planted in rows spaced 0.3 m apart. Thus, the normal swath width of the header of the combine robot is 1.2 m (= 0.3 m × 4 rows). Table 2.1 shows the specifications of the combine robot used in this study. The power output of its engine is 36 kW (49 PS). The combine has three speed ranges: low, middle and high. In the middle range, the maximal harvesting speed is 1.4 m/s. However, it usually harvests rice at a speed of 0.6 - 0.8 m/s. Because this combine uses a hydrostatic transmission (HST), its speed varies continuously. The capacity of the grain tank is 1,500 L.

2.2.2. Navigation Sensors

The navigation sensors used are an RTK-GPS (Topcon Co. Ltd., Legacy-E+) and a GPS compass (Hemisphere Co. Ltd., V110). They are shown in Fig. 2.5

To obtain an absolute and accurate position of the combine, a virtual reference station (VRS) system was used to compensate the signal errors produced by the RTK-GPS. A personal digital assistance (PDA) (Hewlett-Packard Co. Ltd., iPAQ hx2190b) and a mobile phone (Docomo Co. Ltd., FOMA P2403) were used for reference stations, both installed with global navigation satellite system (GNSS) software. Using this VRS-RTK method, a positioning accuracy within ± 30 mm is achieved.

Fig. 2.5. Navigation sensors.
GPS and antenna (left), and GPS compass (right).
(By courtesy of Topcon Co. Ltd. and Hemisphere Co. Ltd.)

The GPS compass has a dual GPS antenna, a differential GPS beacon module, a single-axis gyro, and a tilt sensor. These components are placed in a single enclosure that requires only one power / data cable connection. The heading accuracy of the GPS compass was within 0.50° RMS.

The RTK-GPS and the GPS compass measure the position and heading direction of the combine robot, respectively, at a rate of 20 Hz. Their specifications are summarized in Table 2.2 and Table 2.3.

Table 2.2. Specifications of RTK-GPS.

GPS

Model		Topcon Legacy-E+
Dimensions [mm]	Length	240
	Width	110
	Height	35
Weight [g]		660
Power input [V DC]		6 - 28

RTK accuracy

L1**	Horizontal	± (10 mm + 1.0 ppm × *Dist*) m.s.e
	Vertical	± (15 mm + 1.0 ppm × *Dist*) m.s.e
L1/L2**	Horizontal	± (10 mm + 1.0 ppm × *Dist*) m.s.e
	Vertical	± (15 mm + 1.0 ppm × *Dist*) m.s.e
Refresh rate [Hz]		20

Antenna

Dimensions [mm]	Length	141.6
	Width	141.6
	Height	35.7
Weight [g]		492
Power input [V DC]		2.7 - 12

Dist is measured distance.

**Carrier frequency.

Table 2.3. Specifications of GPS compass.

GPS compass		
Model		Hemisphere V110
Dimensions [mm]	Length	600
	Width	160
	Height	180
Weight [kg]		1.5
Power input [V DC]		10 - 36
Refresh rate [Hz]		20
Accuracy	Orientation	< 0.3° RMS
	Pitch / Roll	< 1.0° RMS

2.2.3. Control System

Figure 2.6 shows the architecture of the control system of the combine robot. The original combine has two electric control units (ECU-A and ECU-B) used for traveling, steering, cutting, threshing, separating/cleaning, unloading, and operating an emergency engine-stop system. The ECUs communicate with each other via a RS-232C port. The operating systems, except for the traveling-operation system to move forward or backward, are drive-by-wire (DBW). To control these operating systems in the combine robot, the software of the ECUs are reprogrammed.

A laptop personal computer (PC) is used as the main computer for the combine robot. Our project team designed and developed two additional ECUs (ECU-KU1 and ECU-KU2) equipped with microcomputers (Renesas, SH7136F) to process navigation data and control commands. ECU-KU1 and ECU-KU2 communicate with each other via a control area network (CAN) bus, while ECU-A and ECU-KU1 communicate with each other via a RS-232C port. In addition, the PC and ECU-KU1 communicate via a RS-232C port.

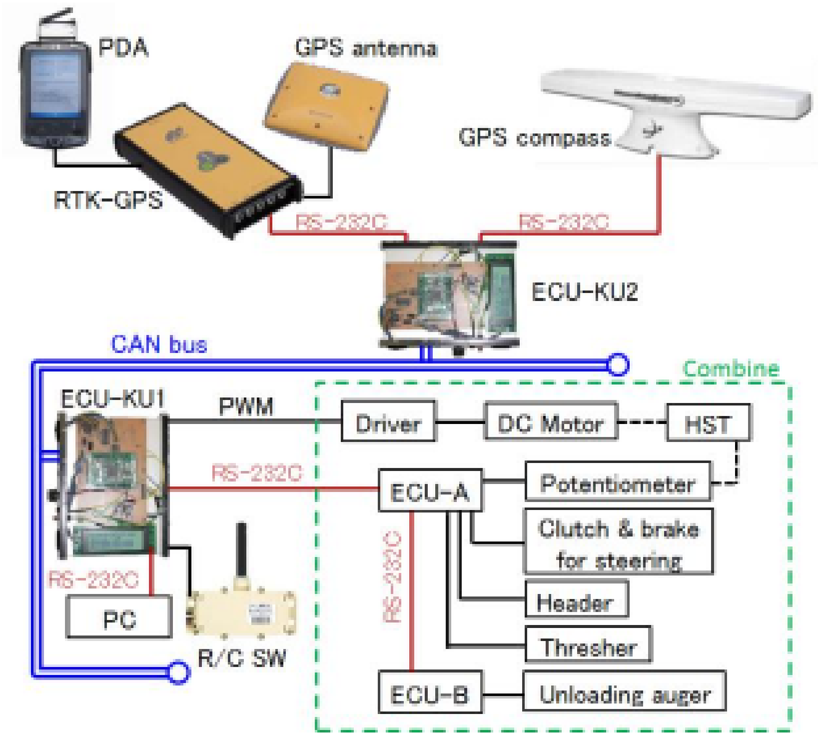

Fig. 2.6. Control system of combine robot.

To control the traveling operation, the speed-control mechanism of the combine are modified, as shown in Fig. 2.7. This mechanism consists of a DC motor, gears, a potentiometer and ECU-KU1. The motor drives the main lever, which is connected to the swath plate of the HST through the gear train. The lever position, which is detected by the potentiometer, is used as a feedback input signal for ECU-KU1. ECU-KU1 controls the rotational angle of the motor by applying pulse-width modulation (PWM).

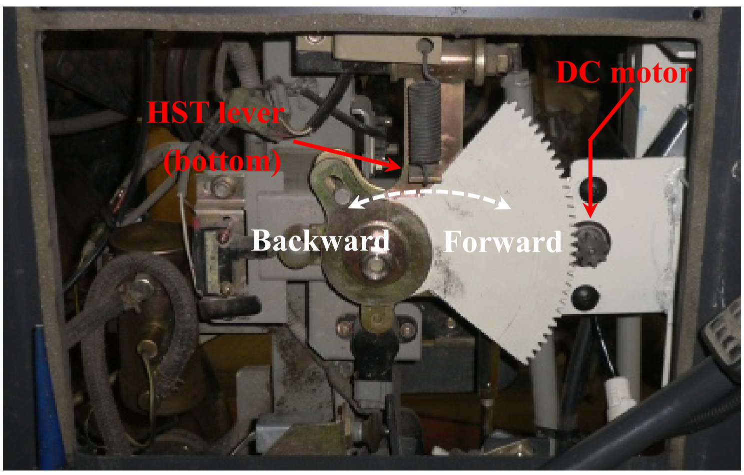

Fig. 2.7. Speed control mechanism driven by DC motor.

The GPS and the GPS compass send position and heading information of the combine, respectively, to the ECU-KU2, which in turn sends this data to the ECU-KU1. Next, the ECU-KU1 merges the received data with the status data of the combine and transmits it in a binary format to the PC. The PC uses this data to compute the control values (steering, speed, and other operation commands), which are sent to the ECU-KU1. In response, the ECU-KU1 controls the position of the main lever and sends the command values to the ECU-A for combine operation. When the ECU-A receives the steering control values from the PC, it controls the hydraulic valves of the left and right clutches and brakes in the transmission. Similarly, the ECU-A also controls the header- and thresher-operating systems. The unloading auger system is controlled by the ECU-B. In the case of an emergency, a radio control switch (R/C SW) can be used to stop the engine of the combine.

2.3. Robotic Harvesting

2.3.1. Steering Control for Straight Path Following

Figure 2.8 shows the relative position and direction of the combine robot with respect to the target path. The position (x_k, y_k) and heading angle ϕ_k of the vehicle are shown in an x-y coordinate system fixed on the ground. Steering control η is determined from lateral error d_k, heading error ϕ_{dk}, and travelling speed v_k. The lateral error d_k is the distance between the current position of the combine and the nearest point P on the target path. The heading error ϕ_{dk} is the angle defined in Fig. 2.8. The look-ahead distance depends on the traveling speed of the combine. In this study, the look-ahead distance is assumed to be equal to the distance the combine travels in 1 s, i.e., v_k. The point on the target path, which is at a distance of v_k from the current position, is defined as Q. If the target path is straight, the angle ψ_k is defined as

$$\psi_k = \sin^{-1}\left(\frac{d_k}{v_k}\right). \tag{2.1}$$

Here, if ψ_k is sufficiently small, Eq. (2.1) can be approximately as follows:

$$\psi_k \approx \frac{d_k}{v_k}. \tag{2.2}$$

The steering control η of the combine is determined from ϕ_{dk} and ψ_k as

$$\begin{aligned} \eta &= k_1\phi_{dk} + k_2\psi_k \\ &= k_1\phi_{dk} + k_2\frac{d_k}{v_k}, \end{aligned} \tag{2.3}$$

where k_1 and k_2 are the control gains, which were determined by performing preliminary test runs.

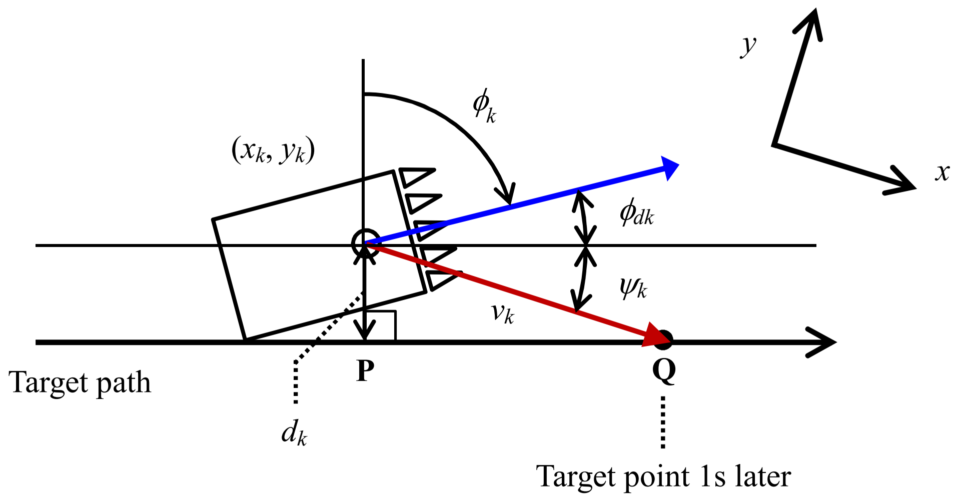

Fig. 2.8. Vehicle's relative position and heading angle against target path.

Thus, it can be expected that this steering-control algorithm will adaptively minimize the lateral and heading angle errors of the combine according to its traveling speed.

2.3.2. Turning Control at Corners

The Japanese head-feeding combine used in this study has a driving seat on the right side of its body, and its header and cutting device are shifted to the left side. Hence, the combine is best suited to harvest crops along a counter-clockwise path so that the header is aligned with the rows of the crops. Therefore, assume that the target path pattern for harvesting operations on a rectangular field is a counter-clockwise spiral path, combined with straight travel and right-angle turns, as shown in Fig. 2.9. This target path is called the *round-harvesting operation* path.

The head-feeding combine requires a wide area for turning at the corners of the field. Thus, before starting the round-harvesting operation, human operators manually harvest four laps of the outermost crop to obtain a sufficient area for turning. Then, the combine robot automatically harvests the rest of the crop.

For transition to the next harvesting strip, the combine has to turn left at the corner. Figure 2.10 illustrates the turning method at a corner in a rectangular field.

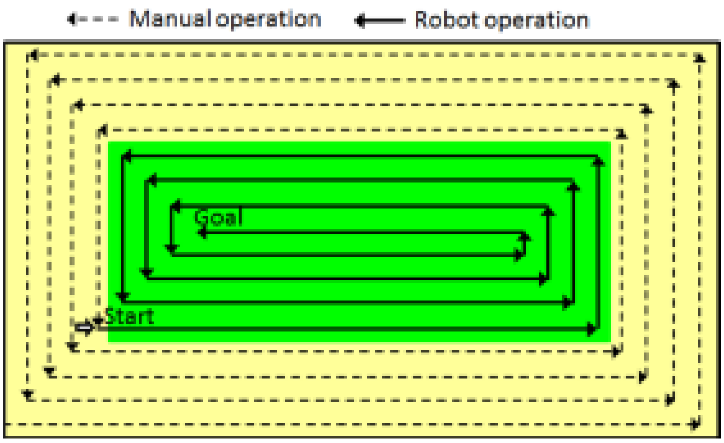

Fig. 2.9. Round-harvesting operation by applying counter-clockwise spiral path.

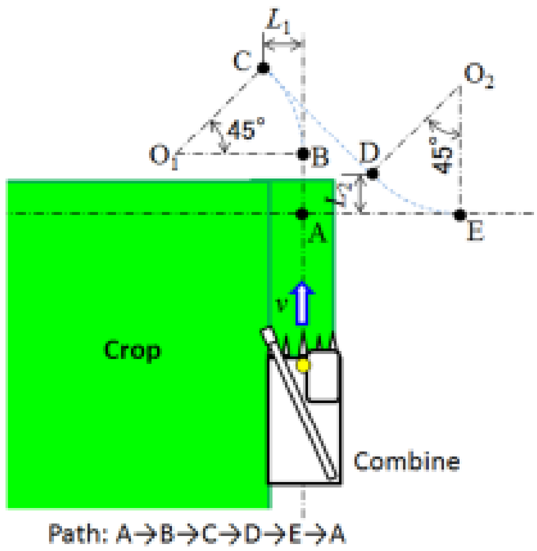

Fig. 2. 10. Turning method at corners.

Points A to E represent target points that the combine has to reach. Point A represents the intersection of the current and next straight paths. After the combine moves forward to point B, it turns to the left at a turning angle of 45°. The turning angle is obtained via the GPS compass. When the combine arrives at point C, the RTK-GPS determines the distance L_1. Next, the combine travels straight backwards to point D, where distance L_2 is equal to distance L_1. Finally, the combine turns to the right with a turning angle of 45º. After turning at the corner, the combine robot begins harvesting the crop along the next straight path.

2.4. Results and Discussion

To examine the performance of the path-following control algorithm, harvesting tests were conducted using the combine robot at a rice paddy field in Nantan City, Kyoto Prefecture, Japan. First, a human operator harvested the four outermost laps of the crop so that the combine robot could automatically turn corners in the field while performing the round-harvesting operation. Next, the combine robot harvested three laps of crop along the target path defined for the round-harvesting operation. The travel speed of the combine robot was set to 0.6 m/s.

Figure 2.11 shows the target path and actual track of the combine robot measured by the RTK-GPS while autonomously harvesting the rice crop.

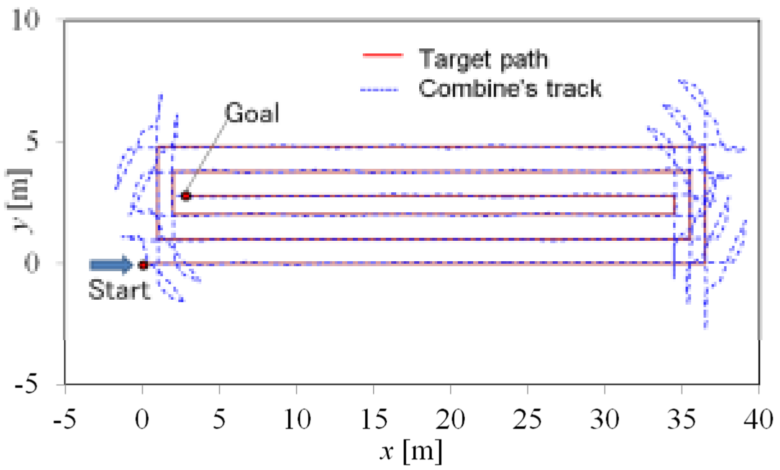

Fig. 2.11. Target path and actual track of combine.

During this experiment, the combine robot harvested 11 straight strips and performed 10 right-angle corner turns in the field. The combine robot harvested rice along straight paths at an average travel speed of 0.59 m/s. The speed control of the combine robot was satisfactory when harvesting along a straight path.

To evaluate the performance of the combine robot, the lateral and heading errors were considered. Since the divider of the combine must pass between rows of rice that are spaced 0.3 m apart, the lateral error at the top of the divider must be less than 0.15 m. The distance between the GPS antenna and the top of the divider is 1 m. Hence, if the lateral and heading errors at the GPS antenna position are less than 0.1 m and 2.0º, respectively, (0.1 m + 1 m × sin(2º) = 0.135 m < 0.15 m), the combine can harvest crops without leaving unharvested crop.

Table 2.4 shows the root mean square errors (RMSE) of the lateral and heading errors for travel along a straight path. All RMSE values of the lateral and heading errors are less than 0.1 m and 2.0º, respectively. This indicates that the straight-path-following control provides the combine robot with sufficient accuracy to harvest rice crops.

Table 2.4. RMSE of lateral and heading errors while traveling along straight path.

Strip No.	Lateral error RMSE [m]	Heading error RMSE [º]
1	0.039	0.84
2	0.031	1.66
3	0.034	1.27
4	0.042	1.50
5	0.029	0.69
6	0.052	1.89
7	0.039	1.38
8	0.059	1.85
9	0.039	1.01
10	0.065	1.06
11	0.040	1.52

Table 2.5 shows the lateral and heading errors after the right-angle turns. The lateral and heading errors vary after the combine turns at a corner. The maximal values of the lateral and heading errors were 0.245 m and 7.96º, respectively. This variation in the errors is due to different soil conditions at the point of turning, and the errors and time delay introduced by the compass. In addition, the turning-control algorithm focuses on correcting the heading angle rather than the position. As a result, compass errors and time delays introduce errors in

turning control. When the combine approached the starting point of the crop row, however, the lateral and heading errors converged to less than 0.1 m and 2.0º, respectively. Consequently, when the combine robot travelled along the target path, it autonomously harvested the crop without leaving any unharvested rice plants.

Table 2.5. Lateral and heading errors after turning at corners.

Turn No.	Lateral error [m]	Heading error [º]
1	-0.034	-0.79
2	0.131	3.71
3	0.245	7.96
4	0.085	1.38
5	0.101	3.15
6	0.195	4.81
7	0.239	7.08
8	0.175	4.28
9	0.032	1.76
10	0.178	3.23

2.5. Conclusions

In this study, a commercial four-row head-feeding combine was modified into a combine robot. To detect the position and heading angle of the vehicle, a RTK-GPS and a GPS compass were used as navigation sensors. Two ECUs were developed to communicate with the ECUs of the combine, the RTK-GPS, and GPS compass, and to control traveling speed. Next, an experiment was conducted during which the combine robot harvested a rice crop in a rectangular field. The results of the experiment demonstrate that the developed combine robot traverses the target path with small lateral and heading errors and can automatically harvest the rice crop.

REFERENCES

[1] Kise, M., Noguchi, N., Ishii, K. and Terao, H: Field mobile robot navigated by RTK-GPS and FOG (Part3) (in Japanese). Journal of Japanese Society of Agricultural Machinery, vol. 64, no. 2, 102-110, 2002.

[2] Takai, R., Barawid, O. Jr., Ishii, K. and Noguchi, N: Development of Crawler-Type Robot Tractor based on GPS and IMU, Preprint of the IFAC International Conference on AGRICONTROL 2010, A3-5, Kyoto, Japan, 2010.

[3] Nagasaka, Y., Umeda, N., Kanetani, Y., Taniwaki, K. and Sasaki, Y: Automated rice transplanter using global positioning and gyroscopes. Computers and Electronics in Agriculture, vol. 43 issue 3, 223-234, 2004.

[4] Iida, M. and Yamada, Y: Rice harvesting operation using an autonomous combine with a GPS and a FOG. *Proceedings* of the Conference of Automation Technology for Offroad Equipment 2006, ASAE, 125-131, 2006.

[5] Iida, M., Uchida, R., Zhu, H., Kurita, H., Suguri, M. and Masuda, R: Development of robot combine harvester equipped with GPS and compass. *Proceedings* of the 4th Asian Conference on Precision Agriculture (ACPA2011), Obiiro, Japan, O-23, 2011.

[6] Iida, M., Uchida, R., Zhu, H., Kurita, H., Suguri, M. and Masuda, R: Development of robotic head-feeding combine. *Proceedings* CD of the CIGR International Symposium on "Sustainable Bioproduction –Water, Energy, and Food" (CIGR2011), Tokyo, Japan, 20HOS3-06, 2011.

[7] Suguri, M., Karita, K. and Nishiike, Y: RTK-GPS based autonomous crawler wagon control, Proceedings of the Automation Technology for Off-road Equipment (ATOE2004), 360-368, 2004.

[8] Iida, M., Uchida, R., Zhu, H., Suguri, M., Kurita, H. and Masuda, R: Path-following control for a head-feeding combine robot. Engineering in Agriculture, Environment and Food, Accepted October 12, 2012.

[9] Culpin, C: Farm Machinery (12th Edition). Blackwell Scientific Publications Ltd., Oxford, England, 222-236, 1992.

[10] Ezaki, H: Grain Harvester (in Japanese). ISEBU, Ibaraki, Japan, 89-140, 1986.

CHAPTER 3

MACHINE VISION SYSTEM FOR POSITIONING AUGER SPOUT

3.1. Introduction

Recently in Japan, research and development of autonomous agricultural machinery has attracted researchers' attention [1]-[7]. In particular, prototypes of a combine harvester have been developed that follow the target path and harvest crops with sufficient accuracy [8], [9]. There are a few research reports for autonomous unloading of forage harvesters [10]-[12]. For head-feeding combine harvester, however, the automation of the unloading operation has not been reported yet.

To automatically discharge grain into the grain storage container, the most important issues revolve around locating the grain container (or the transporter) and the control system to appropriately position the combine's unloading auger. Commercial, medium-sized, head-feeding combines are already equipped with a color camera, such as an auger camera and rear-viewing camera. Thus, automation using image processing requires little hardware modification and is less expensive than other methods. Hence, the use of image processing techniques is a good approach to solve the challenge of locating the grain storage container.

The research belongs to the field of *"visual servoing"*. It involves the use of one or more cameras and a computer vision system to control the position of a device, such as a robotic arm, relative to a part, which requires detecting, tracking, servoing and grasping [13]. Similar problems that require visual servoing have been studied in the field of *"virtual reality"* or *"augmented reality"*. There is, mathematically, no difference in obtaining the relative position of a robotic manipulator to that of some other target (visual) object. The task of identifying specific objects in an image and determining their position and orientation is referred to as "camera pose estimation". Thus, work in these fields is highly related to our study [14], [15]. In particular, a software library called *"ARToolKit"* yields a robust and speedy solution for three-dimensional (3D) object tracking [16]-[21], which also can be a clue to solve the problem of auger positioning.

The objectives of this chapter are to develop a methodology that can achieve two functions: First, the detection of the grain storage container and the relative position of the combine and the fiducial marker, using image processing techniques. Second, the calculation of the target joint angles of the combine's unloading auger, so that the auger spout is accurately positioned relative to a target point to unload grain.

In this chapter, camera pose estimation and the use of ARToolKit library are described first. Then, a kinematic model and the inverse kinematic problem of positioning the unloading auger are presented. The accuracy required for the autonomous unloading operation is also discussed. After that, the detection of the fiducial marker and positioning control of the unloading auger are tested in the field. Based on the results, the positioning accuracy and the effectiveness of the methodology are discussed.

3.2. Machine Vision

In this section, common knowledge regarding visual servoing and augmented reality is briefly summarized. After that, a function of ARToolKit is explained and demonstrated with a simple application.

3.2.1. Camera Pose Estimation

a) Camera Model

In this study, a standard pinhole camera model [22], [23] is adopted. Image acquisition can be also modeled as a 3D perspective projection to the image plane, as illustrated in Fig.

3.1. In this perspective projection model, a 3D point $\boldsymbol{M} = [U, V, W]^T$ in the Euclidean world coordinate system (O, U, V, W) corresponds to a two-dimensional (2D) point $\boldsymbol{m} = [u, v]^T$ on the image coordinate system (c, u, v) using the following transformation. The coordinate system (O_c, U_c, V_c, W_c) is the camera-based coordinate system, whose W_c axis corresponds to the optical axis.

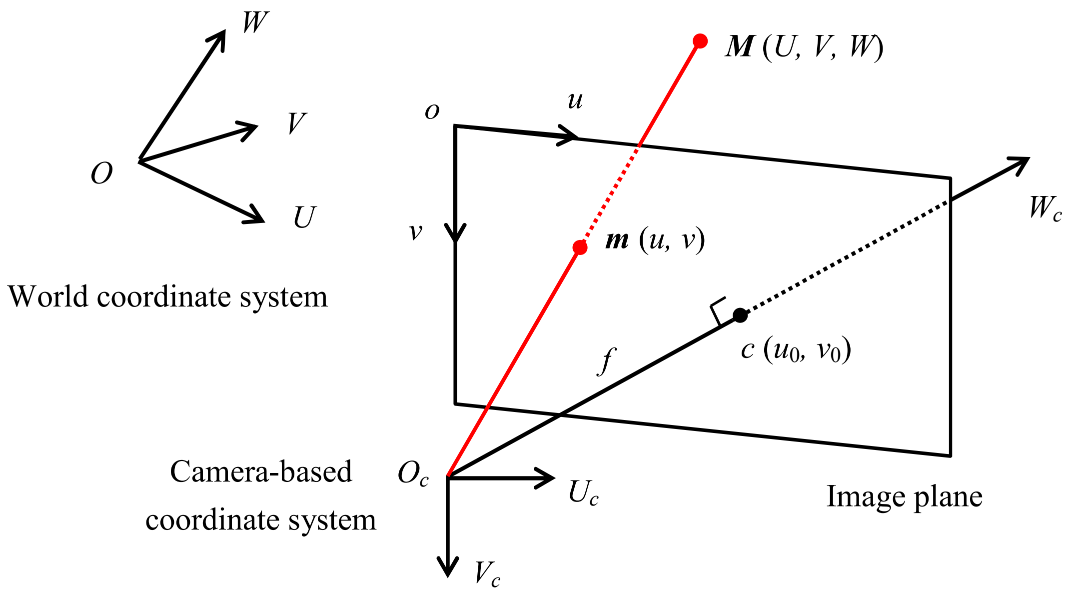

Fig. 3.1. Perspective projection based on pinhole camera model.

$$s\tilde{\boldsymbol{m}} = \boldsymbol{P}\tilde{\boldsymbol{M}}, \tag{3.1}$$

where s is an arbitrary scale factor, $\tilde{\boldsymbol{m}} = [u, \quad v, \quad 1]^T$ and $\tilde{\boldsymbol{M}} = [U, \quad V, \quad W, \quad 1]^T$ are the homogeneous coordinates of point $\boldsymbol{m}$ and $\boldsymbol{M}$. The camera matrix $\boldsymbol{P}$ has 3 × 4 elements and can be decomposed as:

$$\boldsymbol{P} = \boldsymbol{K}\,[\boldsymbol{R} \quad \boldsymbol{t}], \tag{3.2}$$

where matrix $\boldsymbol{K}$ has 3 × 3 elements and $[\boldsymbol{R} \quad \boldsymbol{t}]$ is a 3 × 4 matrix. The matrix $\boldsymbol{K}$ contains intrinsic parameters of a camera and is thereby called the camera internal parameters matrix. $[\boldsymbol{R} \quad \boldsymbol{t}]$, the other component of $\boldsymbol{P}$, is called the external parameters matrix. It is formed from $\boldsymbol{R}$, the rotation matrix, and $\boldsymbol{t}$, the translation vector.

b) Camera Calibration

$\boldsymbol{K}$ is represented as:

$$\boldsymbol{K} = \begin{bmatrix} k_u f & s_k & u_0 \\ 0 & k_v f & v_0 \\ 0 & 0 & 1 \end{bmatrix}, \tag{3.3}$$

where f is the focal length of the camera, k_u and k_v are the scale factor in the u and v directions, and s_k is a skew factor that represents the slant between axes u and v. u_0 and v_0 are the coordinates of the point c, the intersection of the optical axis and the image plane (see Fig. 3.1). In general, a camera is said to be calibrated when the matrix $\boldsymbol{K}$ is identified. An excellent technique for camera calibration using a planar calibration board has been developed in the field of computer science [24], [25].

First, a calibration board is prepared with grid lines. The coordinates of all the cross points on the grid are known in the board-based coordinate system (O_b, U_b, V_b, W_b). Now, the coordinate of a point is written as $[U_b, V_b, W_b]^T$. The point is detected using image processing and represented as $[u, v]^T$ on the image coordinate system, and at the same time represented as $[U_c, V_c, W_c]^T$ on the camera-based coordinate system (c.f. Fig. 3. 1). Then, these coordinates are related as follows:

$$\begin{bmatrix} su \\ sv \\ s \\ 1 \end{bmatrix} = \widetilde{\boldsymbol{K}} \begin{bmatrix} U_c \\ V_c \\ W_c \\ 1 \end{bmatrix} = \widetilde{\boldsymbol{K}} \widetilde{[\boldsymbol{R} \quad \boldsymbol{t}]} \begin{bmatrix} U_b \\ V_b \\ W_b \\ 1 \end{bmatrix}$$
$$\Leftrightarrow \begin{bmatrix} su \\ sv \\ s \\ 1 \end{bmatrix} = \begin{bmatrix} k_u f & s_k & u_0 & 0 \\ 0 & k_v f & v_0 & 0 \\ 0 & 0 & 1 & 0 \\ 0 & 0 & 0 & 1 \end{bmatrix} \begin{bmatrix} r_{11} & r_{12} & r_{13} & t_u \\ r_{21} & r_{22} & r_{23} & t_v \\ r_{31} & r_{32} & r_{33} & t_w \\ 0 & 0 & 0 & 1 \end{bmatrix} \begin{bmatrix} U_b \\ V_b \\ W_b \\ 1 \end{bmatrix}, \tag{3.4}$$

where $\widetilde{\boldsymbol{K}}$ and $\widetilde{[\boldsymbol{R} \quad \boldsymbol{t}]}$ are the homogeneous coordinate representation for $\boldsymbol{K}$ and $[\boldsymbol{R} \quad \boldsymbol{t}]$, respectively. With an adequate number of the correspondences between $[u, v]^T$ and $[U_b, V_b, W_b]^T$, the internal parameters matrix $\boldsymbol{K}$ can be estimated.

Since $\boldsymbol{K}$ is an intrinsic parameter for a camera, it is not affected by the position or the pose of the camera. Thus, $\boldsymbol{K}$ can be estimated off-line for each camera.

c) External Parameters Matrix

The external parameters matrix $[\boldsymbol{R} \quad \boldsymbol{t}]$ represents, from the geometric viewpoint, the transformation from the world coordinate system to the camera-based coordinate system. Hence,

$$\boldsymbol{M}_c = \boldsymbol{R}\boldsymbol{M} + \boldsymbol{t}. \tag{3.5}$$

The problem is to determine $\boldsymbol{R}$ and $\boldsymbol{t}$ when a camera is calibrated. There are various approaches to this problem, since the purpose and the constraints differ between applications. Under the condition of this study the use of some fiducials can facilitate the solving of this problem. Among these approaches, a series of methods based on planar fiducials has become popular because of the robustness and the lower cost of the required computing power [16], [26]. ARToolKit is a publicly available software library which offers a solution based on rectangular and planar fiducial markers.

3.2.2. ARToolKit

Here, the pose estimation procedure in ARToolKit is explained based on the method reported by Kato and Billinghurst [16] and a simple application using the library is demonstrated. The fiducial marker is designed as shown in Fig. 3.2.

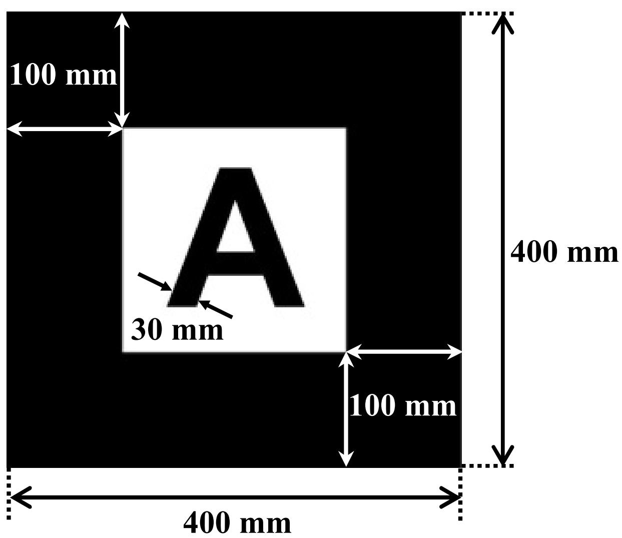

Fig. 3.2. Fiducial marker.

First, after thresholding the input image, a black rectangular enclosure in which an arbitrary pattern is included is extracted. In this thesis, a letter 'A' is used as the pattern to be recognized (see Fig. 3.2). Then, the geometrical information of the black rectangle, namely, four vertices and four line segments, is parameterized and stored. A pair of parallel sides in a fiducial marker is projected onto the image. They are fitted by two line segments, the equations of which in the image coordinate system are as follows:

$$\begin{cases} a_1 u + b_1 v + c_1 = 0. \\ a_2 u + b_2 v + c_2 = 0. \end{cases} \tag{3.6}$$

Let P_{ij} be the (i, j) entry of matrix $\boldsymbol{K}$. A 3D point $\boldsymbol{M}_c = [U_c, V_c, W_c]^T$ on the camera-based coordinate system is related to a 2D point $\boldsymbol{m} = [u, v]^T$ by Eq. (3.4) as follows:

$$\begin{bmatrix} su \\ sv \\ s \\ 1 \end{bmatrix} = \begin{bmatrix} P_{11} & P_{12} & P_{13} & 0 \\ 0 & P_{22} & P_{23} & 0 \\ 0 & 0 & P_{33} & 0 \\ 0 & 0 & 0 & 1 \end{bmatrix} \begin{bmatrix} U_c \\ V_c \\ W_c \\ 1 \end{bmatrix}. \tag{3.7}$$

When $\boldsymbol{M}_c$ is one of the four vertices stored, the corresponding $\boldsymbol{m}$ should satisfy Eq. (3.6). By substituting $[u, v]^T$ in Eq. (3.6), the equations of the planes that contains each side and the optical center can be represented as Eq. (3.8), respectively, on the camera-based coordinate system.

$$\begin{cases} a_1 \left(\dfrac{P_{11} U_c + P_{12} V_c + P_{13} W_c}{P_{33} W_c} \right) + b_1 \left(\dfrac{P_{22} V_c + P_{23} W_c}{P_{33} W_c} \right) + c_1 = 0. \\ a_2 \left(\dfrac{P_{11} U_c + P_{12} V_c + P_{13} W_c}{P_{33} W_c} \right) + b_2 \left(\dfrac{P_{22} V_c + P_{23} W_c}{P_{33} W_c} \right) + c_2 = 0. \end{cases} \tag{3.8}$$

$$\Leftrightarrow \begin{cases} a_1 P_{11} U_c + (a_1 P_{12} + b_1 P_{22}) V_c + (a_1 P_{13} + b_1 P_{23} + c_1) W_c = 0. \\ a_2 P_{11} U_c + (a_2 P_{12} + b_2 P_{22}) V_c + (a_2 P_{13} + b_2 P_{23} + c_2) W_c = 0. \end{cases}$$

From Eq. (3.7) and (3.8), the normal vectors to each plane, $\boldsymbol{n}_1$ and $\boldsymbol{n}_2$, are obtained. The outer product of these two vectors, $\boldsymbol{V}_1$, gives the directional vector of the parallel line segment. For another pair of line segments, $\boldsymbol{V}_2$ is similarly calculated. The unit vectors $\boldsymbol{v}_1$ and $\boldsymbol{v}_2$ are obtained by normalising $\boldsymbol{V}_1$ and $\boldsymbol{V}_2$, respectively. $\boldsymbol{v}_1$ and $\boldsymbol{v}_2$ are not exactly orthogonal because of the image processing error. Thus, they are compensated such that they are orthogonal. Let them be $\hat{\boldsymbol{v}}_1$ and $\hat{\boldsymbol{v}}_2$ each, and their outer product be $\hat{\boldsymbol{v}}_3$. Then, the rotation component of the external parameters, $\boldsymbol{R}$, is represented as follows:

$$\boldsymbol{R} = [\hat{\boldsymbol{v}}_1^t \quad \hat{\boldsymbol{v}}_2^t \quad \hat{\boldsymbol{v}}_3^t]. \tag{3.9}$$

Next, the translation vector $\boldsymbol{t} = [t_u, t_v, t_w]^T$ is calculated. Now, let the four vertices of the fiducial marker be $[U_i', V_i', W_i']^T$ (for $i = 1, \ldots, 4$). Each point is rotated by $\boldsymbol{R}$ into $[U_i, V_i, W_i]^T$ (for $i = 1, \ldots, 4$). After the translation by $\boldsymbol{t}$, each point is represented as $[U_i + t_u, V_i + t_v, W_i + t_w]^T$ (c.f. Eq. (3.5)). And let the corresponding 2D point on the image coordinate system be $[u_i, v_i]^T$ (for $i = 1, \ldots, 4$). Then, by substituting these parameters, Eq. (3.4) gives,

$$\begin{bmatrix} su_i \\ sv_i \\ s \\ 1 \end{bmatrix} = \begin{bmatrix} P_{11} & P_{12} & P_{13} & 0 \\ 0 & P_{22} & P_{23} & 0 \\ 0 & 0 & 1 & 0 \\ 0 & 0 & 0 & 1 \end{bmatrix} \begin{bmatrix} U_i + t_u \\ V_i + t_v \\ W_i + t_w \\ 1 \end{bmatrix}. \tag{3.10}$$

Let it be rearranged about t_u, t_v and t_w as follows:

$$\begin{cases} su_i = P_{11}(U_i + t_u) + P_{12}(V_i + t_v) + P_{13}(W_i + t_w) \\ su_i = P_{22}(V_i + t_v) + P_{23}(W_i + t_w) \\ s = W_i + t_w \end{cases}.$$

$$\Leftrightarrow \begin{cases} P_{11}t_u + P_{12}t_v + (P_{13} - u_i)t_w = W_i u_i - P_{11}U_i - P_{12}V_i - P_{13}W_i \\ P_{22}t_v + (P_{23} - v_i)t_w = W_i v_i - P_{22}V_i - P_{23}W_i \end{cases}. \tag{3.11}$$

$$\Leftrightarrow \begin{bmatrix} P_{11} & P_{12} & P_{13} - u_i \\ 0 & P_{22} & P_{23} - v_i \end{bmatrix} \begin{bmatrix} t_u \\ t_v \\ t_w \end{bmatrix} = \begin{bmatrix} W_i u_i - P_{11}U_i - P_{12}V_i - P_{13}W_i \\ W_i u_i - P_{22}V_i - P_{23}W_i \end{bmatrix}.$$

For any $i = 1, \ldots, 4$, Eq. (3.11) is defined, and thereby eight equations are obtained for three unknowns. Then, the translation vector is calculated by least squares method.

Figure 3.3 shows an exemplary application making use of the library. Fiducial markers are shown in Fig. 3.3-(a) and virtual objects are overlaid onto them based on the estimated position and orientation of the camera as in Fig. 3.3-(b). In this application, the estimated pose (i.e., the external parameters matrix) relative to the marker is used for precise rendering.

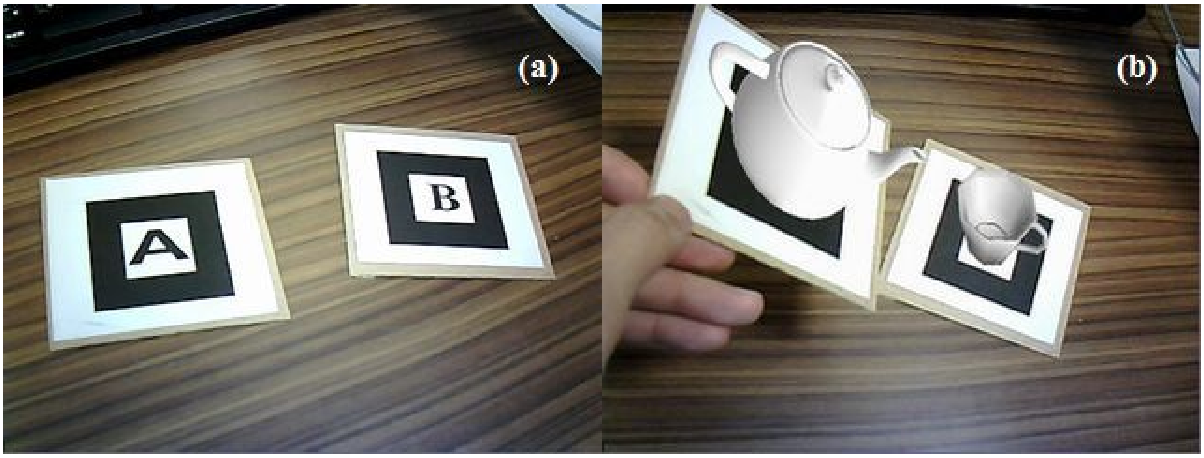

Fig. 3.3. Exemplar application of ARToolKit.
(a). Fiducial markers; (b). Overlaid virtual objects.
*Teacup and teapot are rendered using OpenGL.

3.3. Unloading Auger

As referred to in Section 2.1, the harvested and cleaned grain is stored in the grain tank of the combine harvester. This grain is then discharged into the grain storage container via the unloading auger. This section describes in detail the mechanism of the unloading auger and the control for the robotic unloading operation. Then, the kinematic model of the unloading auger is derived.

3.3.1. Mechanism and Control

Figure 3.4 illustrates the mechanism of the unloading auger. Upon commencement of unloading, grain is sent from the grain tank to the unloading auger. It is then conveyed upward by a screw auger and flows out of the spout. As shown in Fig. 3.4, the unloading auger has two axes, around which it turns left and right, or up and down. These joints are actuated by a DC motor and a hydraulic cylinder, respectively.

The turning angle in the left-right direction is acquired by a potentiometer, which was already mounted on the commercial combine. To obtain the turning angle in the up-down direction, we installed another potentiometer (see Fig. 3.4). Figure 3.5 shows the control system of the unloading auger. Each joint angle, left-right turning or up-down turning, is measured by the potentiometers. The measured voltage, varying from 0 to 5 V, is converted with a 10-bit analogue-to-digital converter (ADC) into a digital value. Thus, the resolution is 0.00489 (= $5 / (2^{10} - 1)$) [V/div]. Table 3.1 presents the motion range, the resolution and the speed for each joint. To avoid chattering, ± 5 div is assigned as a dead band.

Table 3.1. Motion range, resolution and speed for each joint.

	Motion range [°]	Resolution [°/div]	Speed [°/s]
Joint 1	$-110 < \theta_1 < 200$	0.30	38.3
Joint 2	$0 < \theta_2 < 45$	0.05	20.7 (up) 10.7 (down)

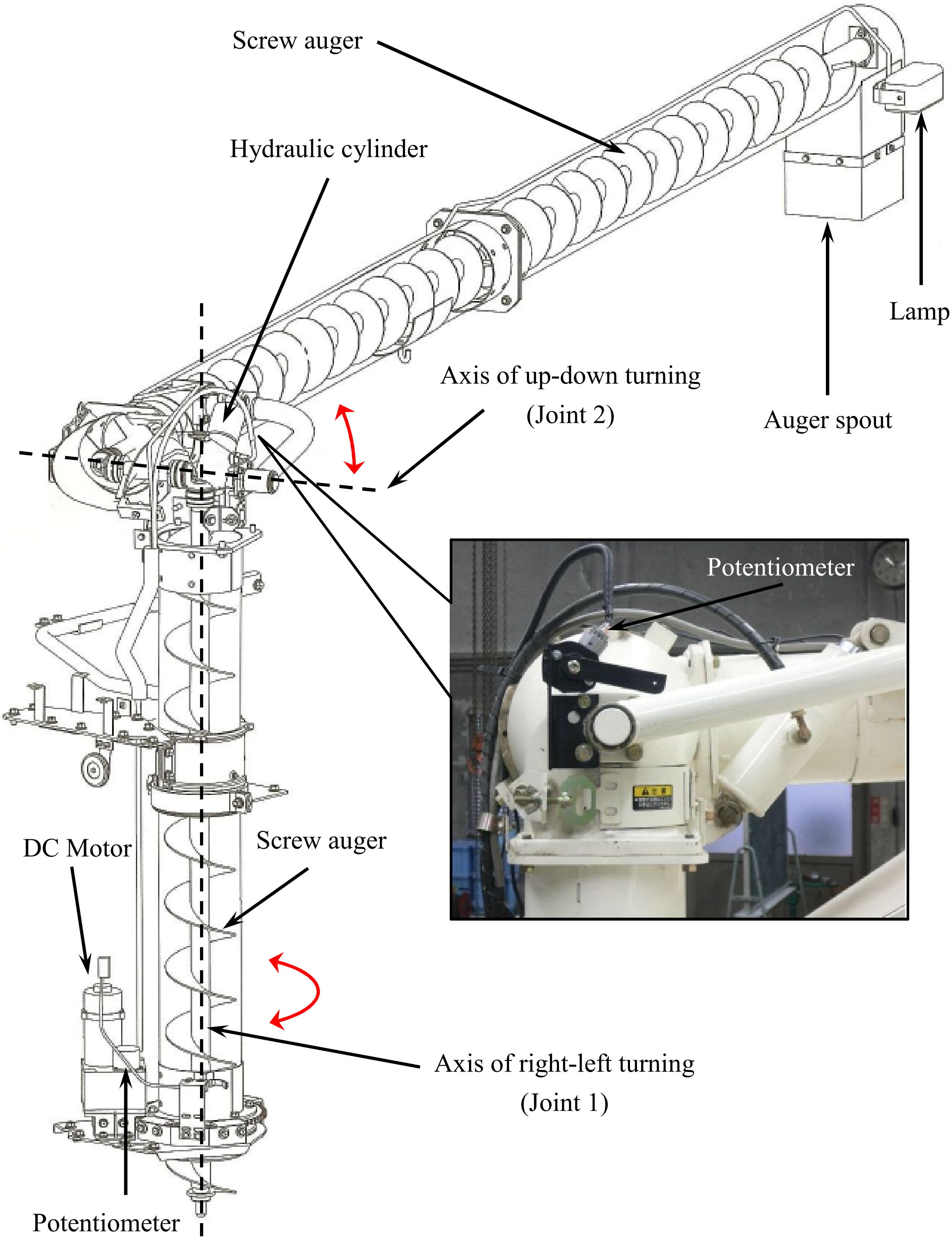

Fig. 3.4. Mechanism of unloading auger.

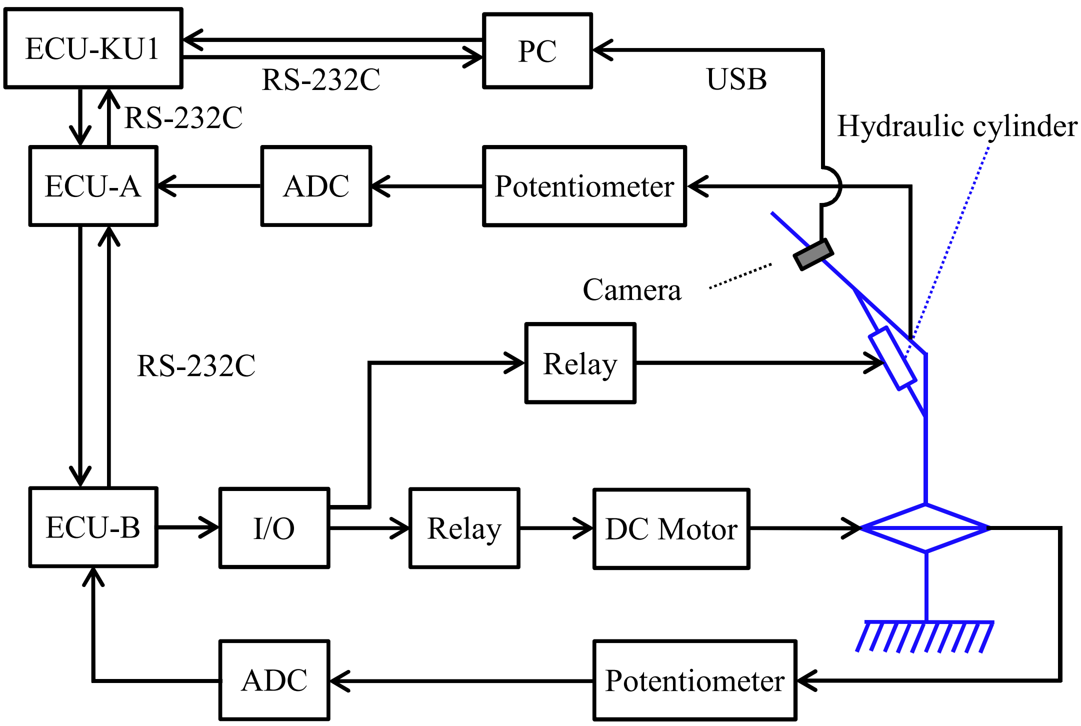

Fig. 3.5. Control system of unloading auger.

3.3.2. Kinematic Model

The unloading auger of the combine used in this study is modeled as a two-degrees-of-freedom (2-DOF) manipulator that consists of two joints (Joint1 and Joint2). As illustrated in Fig. 3.6 and Fig. 3.7, a right-handed coordinate system is assigned to the combine, whose x axis heads along the body in the opposite direction of the head of the combine and z axis points upward in a vertical direction. Let this combine-based coordinate system be Σ_0 in this study. The state of the unloading auger is determined by the two joint angles. Let them be θ_1 and θ_2, hereinafter. As shown in Table 3.1, joint 1 rotates at an angle of $-110° < \theta_1 < 200°$. Grain can be discharged in a range from $-110° < \theta_1 < 90°$. However, the unloading range in this study was limited to $0° < \theta_1 < 90°$ (see Fig. 3.8). This was firstly because the actual unloading task takes place within this range and secondly because the available freedom of the unloading auger is extremely restricted in the range from $-110° < \theta_1 < 0°$. Joint 2 rotates at an angle from $0° < \theta_2 < 45°$ (see Fig. 3.9).

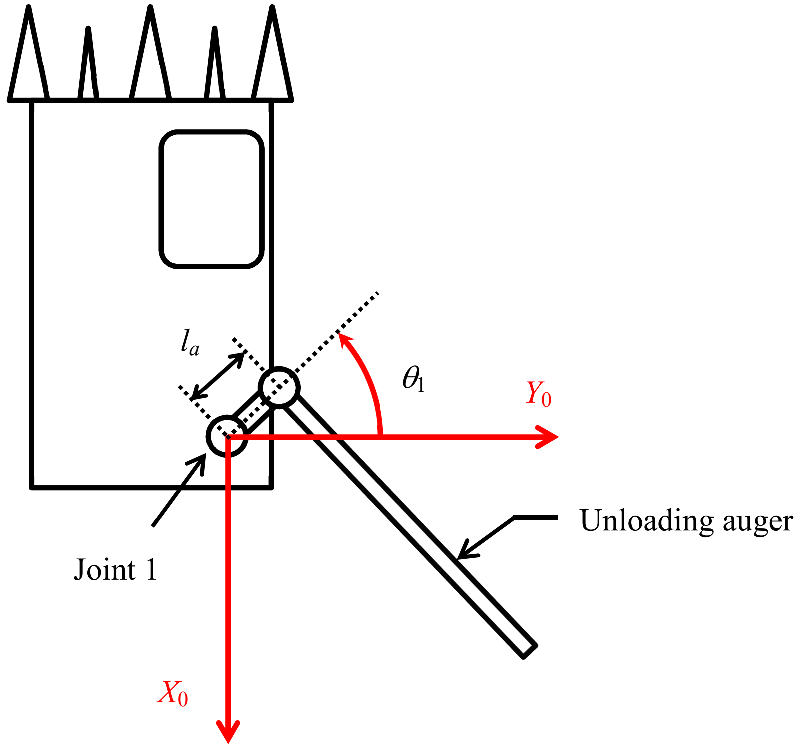

Fig. 3.6. Top view of combine harvester and coordinate system Σ_0.

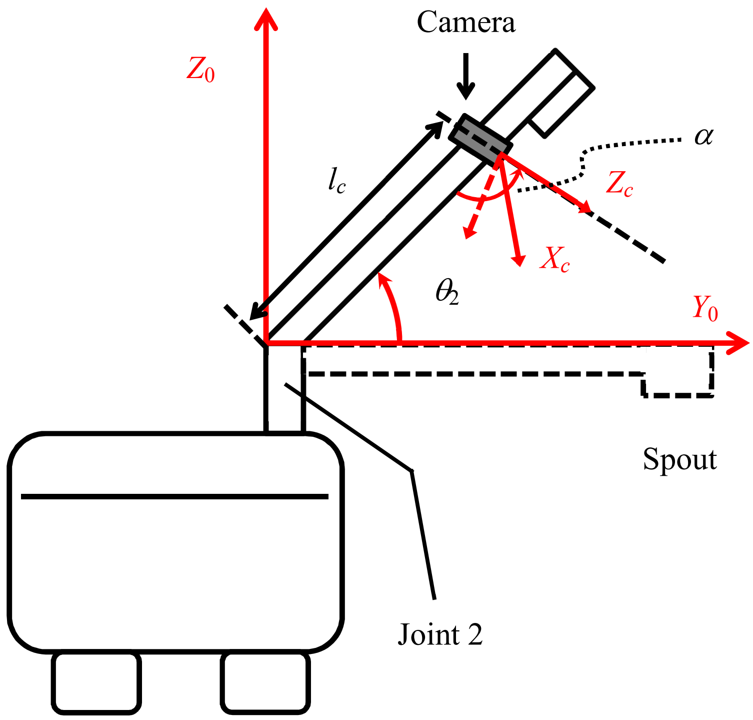

Fig. 3.7. Rear view of combine harvester and coordinate system Σ_0.

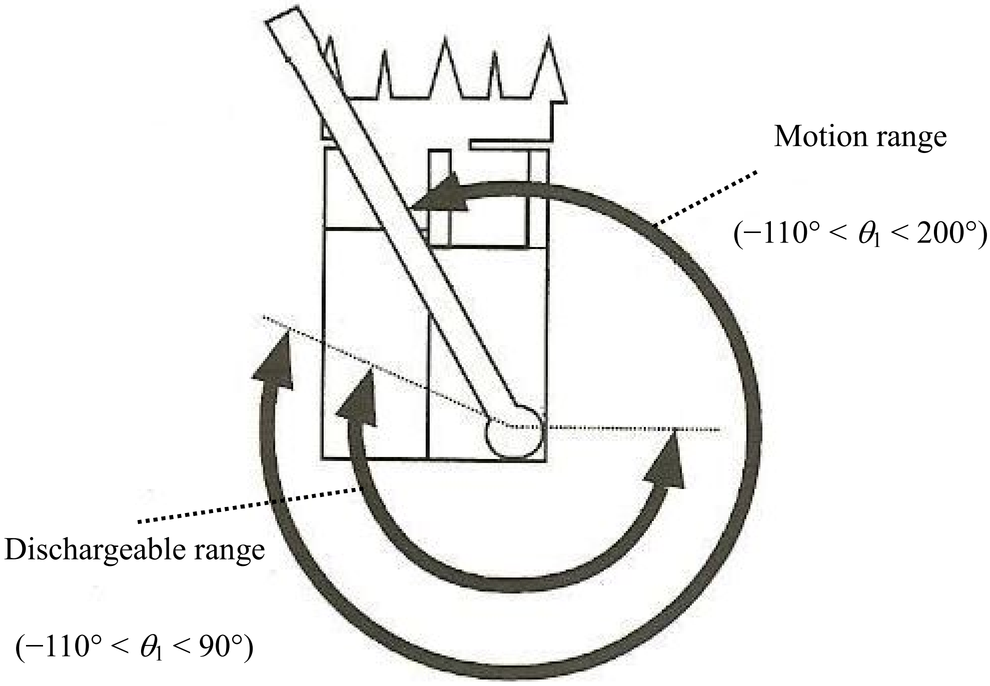

Fig. 3.8. Motion range and dischargeable range of θ_1.

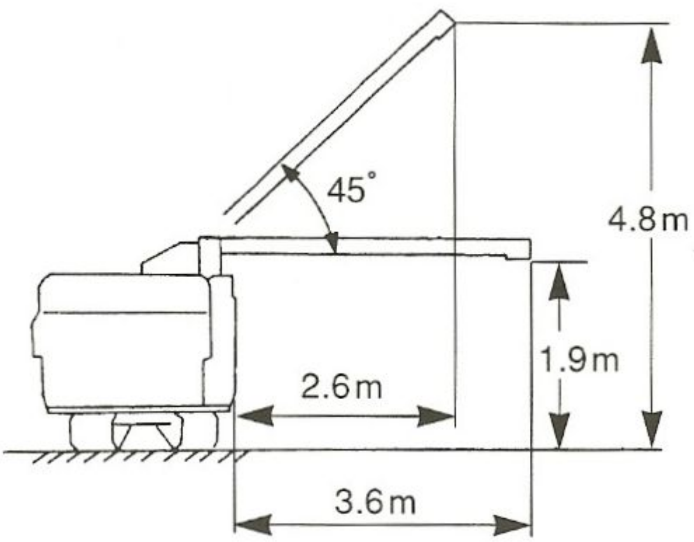

Fig. 3.9. Motion range of θ_2.

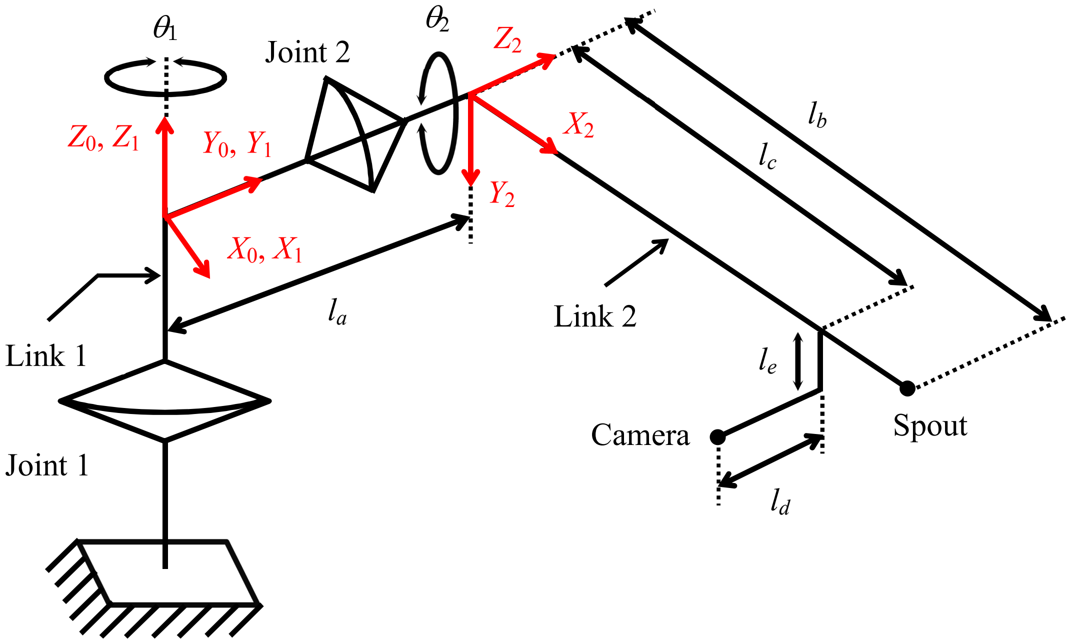

Fig. 3.10. Link structure of unloading auger.

In general, a n-DOF manipulator can be modeled as a connection of n links and n joints. Here, the link is the arm of the manipulator which connects the two adjacent joints. The geometric relations between the adjacent coordinates systems can be expressed by a *Denavit-Hartenberg* notation [27]. In what follows, the coordinate system is described by this method. The target joint angles θ_1 and θ_2 to achieve an arbitrary state of the unloading auger are calculated as an inverse kinematics problem of the robot manipulator [28]-[31].

Figure 3.10 shows the link structure and three coordinate systems Σ_0, Σ_1 and Σ_2, which are also right-handed systems. l_a is the offset distance between the origins of Σ_1 and that of Σ_2 along the Y_1 axis. l_b and l_c represent the lengths from the origin of Σ_2 to the auger spout and to the camera, respectively. l_d and l_e are the distances from the X_2 axis to the camera in the $-Z_2$ direction and Y_2 direction, respectively. The link parameters of the unloading auger are shown in Table 3.2.

Table 3.2. Link parameters of unloading auger.

Link	Link length [mm]	Twist angle [°]	Distance between the links [mm]	Joint angle [°]
1	0	0	0	θ_1
2	0	-90	l_a	-θ_2

Σ_0 is the initial coordinate system (X_0, Y_0, Z_0) before rotating the auger; Σ_1 is the coordinate system (X_1, Y_1, Z_1) rotated by the angle θ_1 around the Z_0 axis in the system Σ_0 using the homogeneous transformation matrix ${}^0\boldsymbol{T}_1$, expressed by Eq. (3.12).

$$ {}^0\boldsymbol{T}_1 = \begin{bmatrix} \cos\theta_1 & -\sin\theta_1 & 0 & 0 \\ \sin\theta_1 & \cos\theta_1 & 0 & 0 \\ 0 & 0 & 1 & 0 \\ 0 & 0 & 0 & 1 \end{bmatrix}. \tag{3.12} $$

Σ_2 is the coordinate system (X_2, Y_2, Z_2) rotated by the angle −90° around the X_1 axis, $-\theta_2$ around the Z_2 axis, and then translated by l_a in the Y_1 direction using ${}^1\boldsymbol{T}_2$, which is expressed by Eq. (3.13).

$$ {}^1\boldsymbol{T}_2 = \begin{bmatrix} \cos\theta_2 & -\sin\theta_2 & 0 & 0 \\ 0 & 0 & 1 & l_a \\ -\sin\theta_2 & -\cos\theta_2 & 0 & 0 \\ 0 & 0 & 0 & 1 \end{bmatrix}. \tag{3.13} $$

Σ_{Camera} (X_C, Y_C, Z_C) is the camera-based coordinate system. As well as ${}^0\boldsymbol{T}_1$ and ${}^1\boldsymbol{T}_2$, the relation between Σ_2 and Σ_{Camera} is expressed by the transformation matrix ${}^2\boldsymbol{T}_{Camera}$. In the transformation from Σ_2 to Σ_{Camera}, Σ_2 is translated by l_c in the X_2 axis, l_e in the Y_2 axis, and $-l_d$ in the Z_2 axis. It then rotates by 90° about the Y_2 axis, −90° about the latest X_2 axis, and α about the latest X_2 axis. Thus, the homogeneous transformation matrix ${}^2\boldsymbol{T}_{Camera}$ is expressed as shown in Eq. (3.14).

$$
{}^{2}\boldsymbol{T}_{Camera} = \begin{bmatrix} 0 & -\sin\alpha & \cos\alpha & l_c \\ 0 & \cos\alpha & \sin\alpha & l_e \\ -1 & 0 & 0 & -l_d \\ 0 & 0 & 0 & 1 \end{bmatrix}. \tag{3.14}
$$

The geometrical relationship between the coordinate systems assigned to the combine are as described above. Moreover, ${}^{Camera}\boldsymbol{T}_{Marker}$ is obtained from a function of ARToolKit. Therefore, ${}^{0}\boldsymbol{T}_{Marker}$ can be derived as,

$$
{}^{0}\boldsymbol{T}_{Marker} = {}^{0}\boldsymbol{T}_{1}\,{}^{1}\boldsymbol{T}_{2}\,{}^{2}\boldsymbol{T}_{Camera}\,{}^{Camera}\boldsymbol{T}_{Marker}. \tag{3.15}
$$

If the vector of the target point on Σ_{Marker} is abbreviated as ${}^{Marker}\boldsymbol{r}_{Target}$, then ${}^{0}\boldsymbol{r}_{Target}$ is described with ${}^{0}\boldsymbol{T}_{Marker}$ as,

$$
\begin{aligned}
{}^{0}\boldsymbol{r}_{Target} &= {}^{0}\boldsymbol{T}_{Marker}\,{}^{Marker}\boldsymbol{r}_{Target} \\
&= {}^{0}\boldsymbol{T}_{1}\,{}^{1}\boldsymbol{T}_{2}\,{}^{2}\boldsymbol{T}_{Camera}\,{}^{Camera}\boldsymbol{T}_{Marker}\,{}^{Marker}\boldsymbol{r}_{Target},
\end{aligned} \tag{3.16}
$$

where ${}^{0}\boldsymbol{T}_{1}$ and ${}^{1}\boldsymbol{T}_{2}$ are given by θ_1 and θ_2, respectively, corresponding to the auger's present position. ${}^{2}\boldsymbol{T}_{Camera}$ is determined by the camera's elevation angle α.

${}^{0}\boldsymbol{r}_{Spout}$, the positional vector of the auger spout on Σ_0, is written with ${}^{2}\boldsymbol{r}_{Spout}$, on Σ_2, as follows:

$$
{}^{0}\boldsymbol{r}_{Spout} = {}^{0}\boldsymbol{T}_{1}\,{}^{1}\boldsymbol{T}_{2}\,{}^{2}\boldsymbol{r}_{Spout}. \tag{3.17}
$$

Figure 3.11 shows the geometric relationship between the auger spout, the target point, and the fiducial marker, as well as the two coordinate systems Σ_0 and Σ_{Marker}. The target point is a 3D point to which the auger spout should be positioned. The coordinate system Σ_{Marker} is a fiducial-marker-based coordinate system generated by (X_M, Y_M, Z_M), which is also a right-handed system.

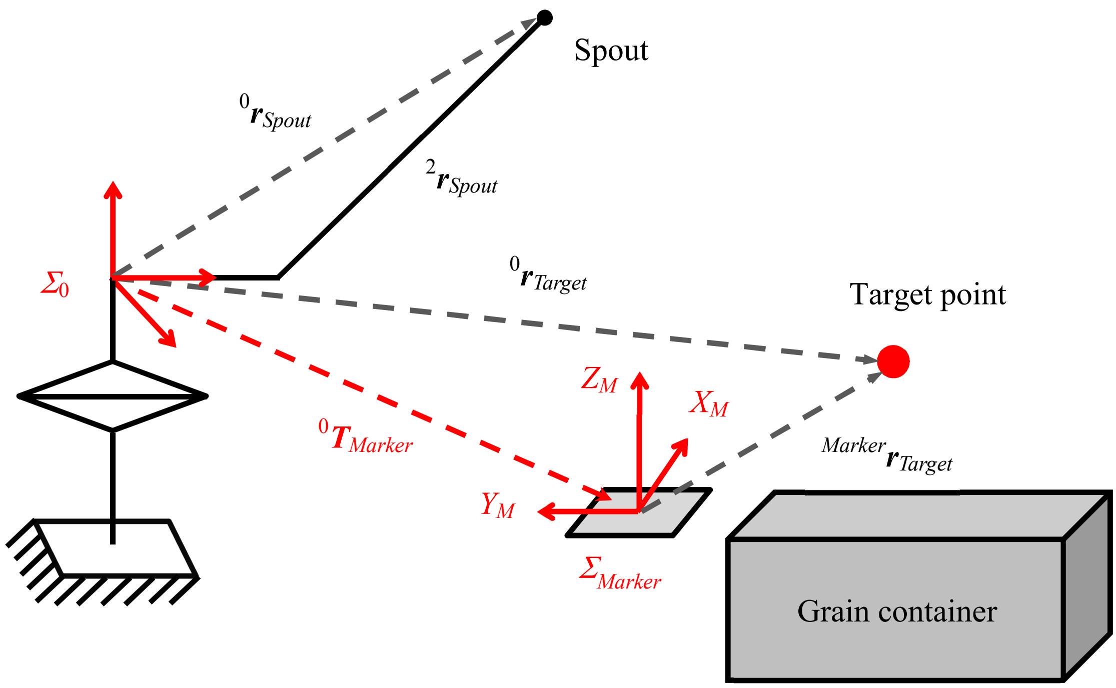

Fig. 3.11. Geometric relation among auger spout, target point, and fiducial marker.

Considering the fact that $^{2}\boldsymbol{r}_{Spout}$ is expressed in Eq. (3.18),

$$^{2}\boldsymbol{r}_{Spout} = [l_b \quad 0 \quad 0 \quad 1]^T, \tag{3.18}$$

Eq. (3.17) gives

$$^{0}\boldsymbol{r}_{Spout} = \begin{bmatrix} l_b \cos\theta_1 \cos\theta_2 - l_a \sin\theta_1 \\ l_b \sin\theta_1 \cos\theta_2 + l_a \cos\theta_1 \\ l_b \sin\theta_2 \\ 1 \end{bmatrix}. \tag{3.19}$$

The target joint angles θ_1 and θ_2 are determined so as to satisfy Eq. (3.20).

$$^{0}\boldsymbol{r}_{Spout} = {}^{0}\boldsymbol{r}_{Target}. \tag{3.20}$$

If the vector $^{0}\boldsymbol{r}_{Target}$ is denoted by $[x_0, \quad y_0, \quad z_0, \quad 1]^T$, which is calculated according to Eq. (3.16), Eq. (3.20) gives:

$$\theta_1 = \tan^{-1}\frac{x_0}{y_0} - \sin^{-1}\left(\frac{l_a}{\sqrt{{x_0}^2 + {y_0}^2}}\right), \tag{3.21}$$

$$\theta_2 = \cos^{-1}\left(\frac{\sqrt{{x_0}^2 + {y_0}^2 - {l_a}^2}}{l_b}\right) \tag{3.22}$$

, which are the desired joint angles.

Again, a target point is initially set on Σ_{Marker}. The vector of the target point on the combine-based coordinate system Σ_0, ${}^0\boldsymbol{r}_{Target}$ is calculated on the basis of ${}^0\boldsymbol{T}_1$, ${}^1\boldsymbol{T}_2$, and ${}^2\boldsymbol{T}_{Camera}$, which are determined by the link structure and its parameters (Fig. 3.6, Fig. 3.7 and Fig. 3.10), and ${}^{Camera}\boldsymbol{T}_{Marker}$, which is obtained from the camera images using ARToolKit. The positional vector of the auger spout on Σ_0, ${}^0\boldsymbol{r}_{Spout}$ is calculated in Eq. (3.17). Finally, by solving Eq. (3.20) (about x and y coordinates), the joint angles are determined such that the spout moves to the target point.

3.4. Required Accuracy

Figure 3.12 shows the pickup truck (SUZUKI Motor Corporation, Carry) with grain storage container (TAISHO Corporation, SBX-11N). Table 3.3 and Table 3.4 show the specifications of the grain storage container and the truck, respectively.

Fig. 3.12. Pickup truck with grain container.

Table 3.3. Specifications of grain container.

Model		SBX-11N
Dimensions [mm]	Length	1,830
	Width	1,300
	Height	1,170
Volume [L]		1,700
Weight [kg]		185
Discharging efficiency [kg/min]		200 - 250
Power input [DC V]		12

Table 3.4. Specifications of pickup truck.

Dimensions [mm]	Length	3,395
	Width	1,475
	Height	1,790
Dimensions of rear deck [mm]	Length	1,940
	Width	1,410
Tread [mm]	Front	1,305
	Rear	1,290
Height of rear deck [mm]		640
Weight [kg]		720

This type of pickup truck is universally used by Japanese farmers and nearly-standardized, and thereby most of all the commercialized grain containers are designed to be mountable on the truck (see Fig. 3.12). Thus, our autonomous unloading operation also assumes the use of this kind of wagon.

In the unloading operation, it is important to eliminate any unloading loss, for instance, spilling grain outside the grain storage container. To discharge grains without any loss, the grain stream is positioned over the top edges of the grain storage container, and there needs to be sufficient room between the grain stream and both side edges of the storage container. Figure 3.13 shows the dimensions of the grain storage container and the maximum width of the grain stream in the actual unloading operation.

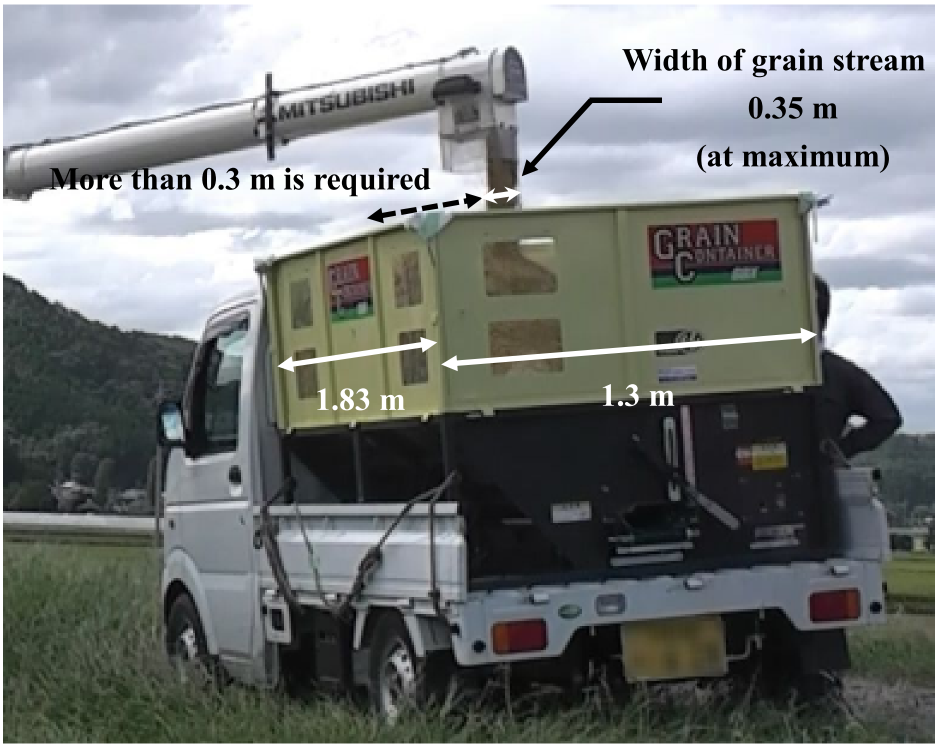

Fig. 3.13. Dimensions of grain storage container and maximum width of grain stream.

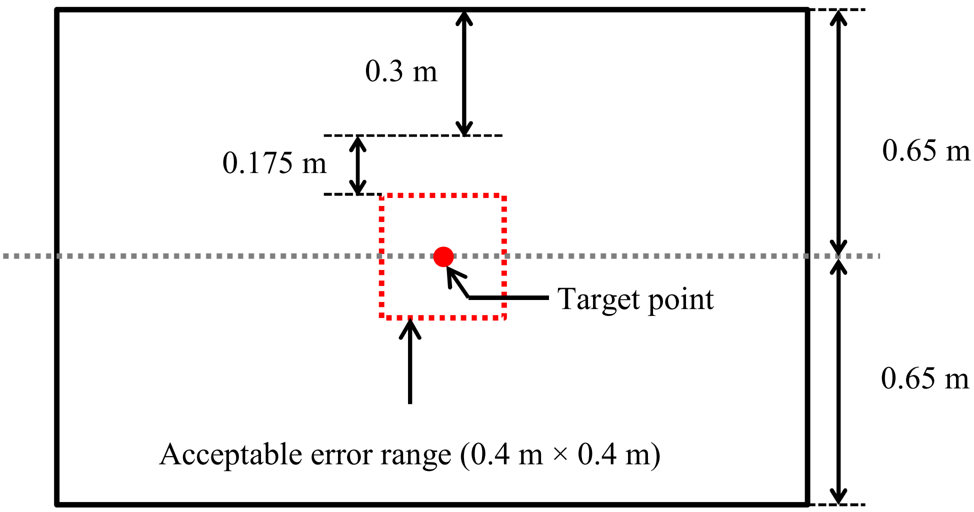

Fig. 3.14. Acceptable error range between grain storage container and auger spout (top view).

In the actual unloading process, the maximum width of the grain stream from the spout is 0.35 m. Allowing for sufficient space between the auger spout and the sides of the grain storage container, the grain stream should no less than 0.3 m from the sides of the grain storage container, in order to meet our requirement of no unloading loss. Thus, the auger spout should be positioned within a square of 0.4 m × 0.4 m, as shown in Fig. 3.11.

A fiducial marker, that indicates the position of the grain storage container, is put on the roof of the pick-up truck. Figure 3.15 illustrates a view from above of the relative position between the fiducial marker and the grain storage container. The distance between the center of the fiducial marker and the center of the grain container is 1.5 m.

As mentioned above, the required specifications for autonomous unloading operation are defined as follows: 1) A target point is set at $(x, y) = (1.5, 0)$ on the coordinate system of the fiducial marker shown in the figure. 2) An acceptable error range for the auger spout position is within a 0.4 m × 0.4 m square.

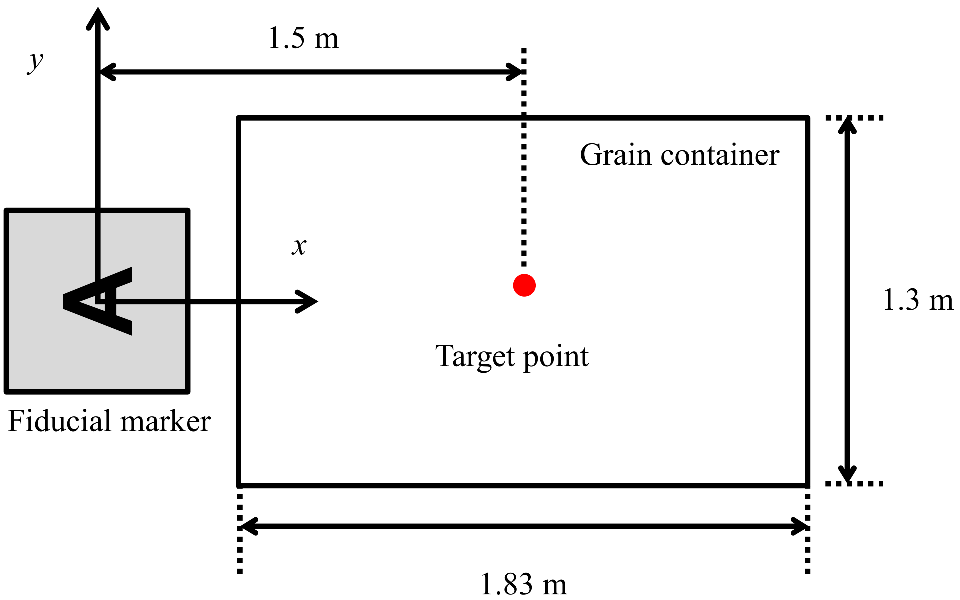

Fig. 3.15. Fiducial marker and grain storage container (top view).

3.5. Experiments of Auger Positioning

A universal serial bus (USB) camera (ELECOM, Co., Ltd., UCAM-DLA200HSV) is mounted on the unloading auger, as shown in Fig. 3.16. Table 3.5 gives its specifications.

Fig. 3.16. USB camera.

Table 3.5. Specifications of camera.

Model		ELECOM UCAM-DLA200HSV
Power		USB 2.0 port, 5V, 500mA
Pixel count		2 million
Image sensor		1/4 inch CMOS
Focus		Manual
Resolution		640 × 480
Frame rate		25fps
Color depth		24bit
Angle of View		60° (diagonal)
Dimension [mm]	Length	42
	Width	65
	Height	72
Weight [g]		100

In the experiment certain assumptions are made. First, the combine is parked alongside the truck that is located on a farm road adjacent to the paddy field. Second, the fiducial marker lies within the camera's field of view, and the auger spout can physically reach the grain storage container and the assigned target point.

The PC is used for processing images captured by the auger camera and controlling the unloading auger of the combine. The experiment was performed according to the following steps: first, an operator starts the software program when the auger is at a state in which the camera can capture the entire fiducial marker and the software determines the target joint angles for positioning. Second, the control program controls the unloading auger to position its spout to the target point. Third, the position of the spout and the fiducial marker are measured with a total station (SOKKIA Co., Ltd., SET 4100s), which is a surveying instrument that integrates a laser range finder and theodolite (see Fig. 3.17). After that, he manually returns the unloading auger to a state where the camera can observe the marker.

Fig. 3.17. Total station.

The positioning accuracy of the unloading auger was determined for four relative positions between the combine and the grain storage container, as shown in Fig. 3.18. These positions were investigated in order to confirm the degree with which relative positions influence either positively or negatively the positioning accuracy of the auger spout. Thus, for each relative position, as shown in Fig. 3.18, the experiments were performed five times.

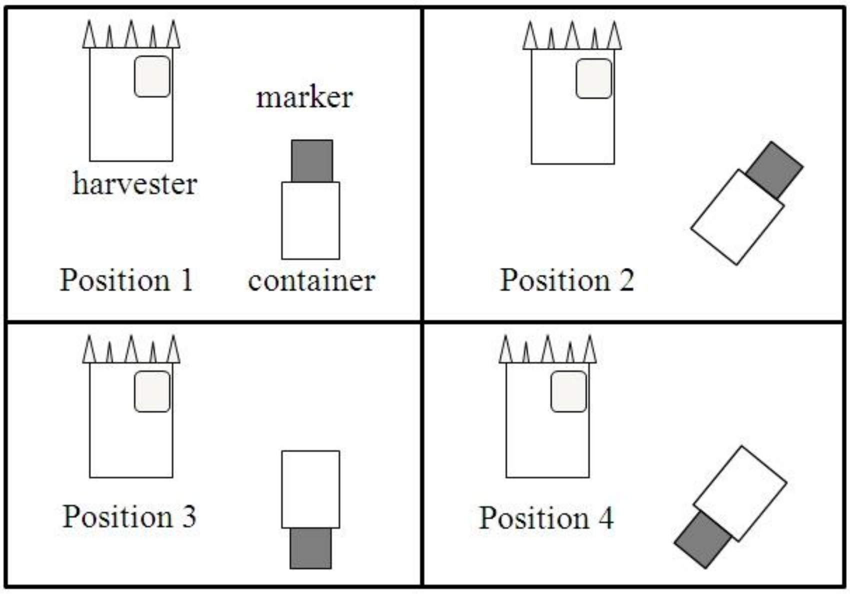

Fig. 3.18. Relative positions between combine harvester and pickup truck.

Table 3.6 shows the actual parameters with respect to the unloading auger and the camera installation in this experiment.

Table 3.6. Parameters of unloading auger and camera installation.

l_a [mm]	200
l_b [mm]	4,280
l_c [mm]	3,195
l_d [mm]	135
l_e [mm]	90
α [°]	90

3.6. Results and Discussion

Figure 3.19 shows the positioning accuracy of the auger spout by the combine robot. It shows the difference between the target position of the auger spout and the actual position determined by the joint angles after positioning. *x* and *y* axes correspond to the ones shown in Fig. 3.15. The results show that the combine robot can position the auger spout within an accuracy of ± 0.1 m.

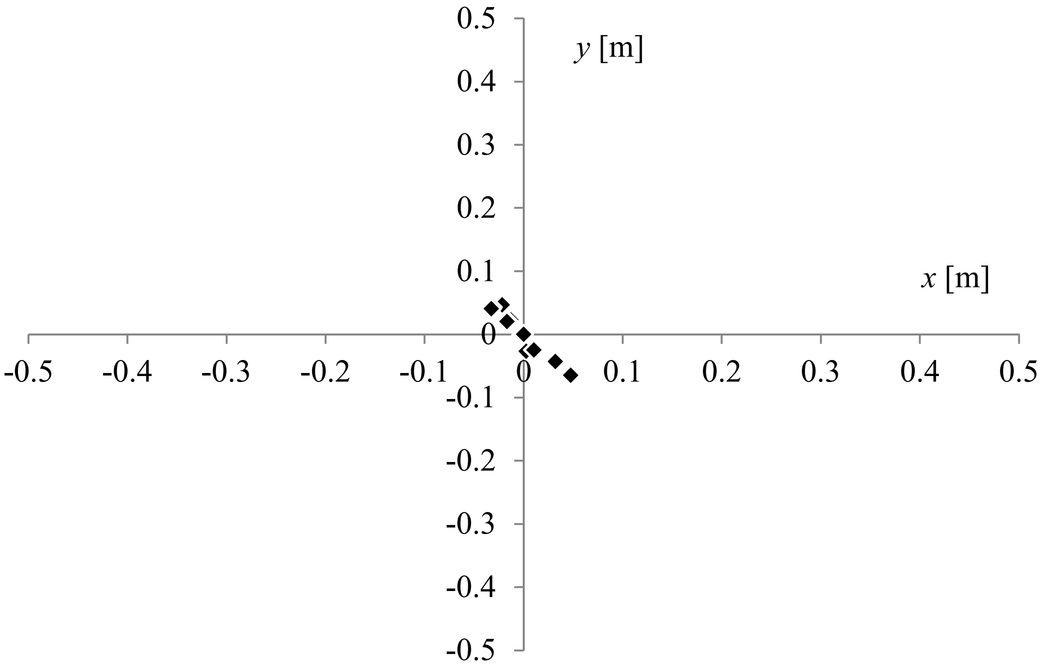

Fig. 3.19. Positioning accuracy of unloading auger.

The markers show the difference between the auger spout position calculated by the input angles (obtained by the software) and that calculated by the actual angles after positioning (obtained by the combine control program).

Figure 3.20 to Fig. 3.23 show the experimental results for all tests. Positions 1 to 4 correspond to the relative positions depicted in Fig. 3.18. Each plot indicates the final horizontal position of the spout after positioning, which is measured with the total station, and is represented on the coordinate system shown in Fig. 3.15

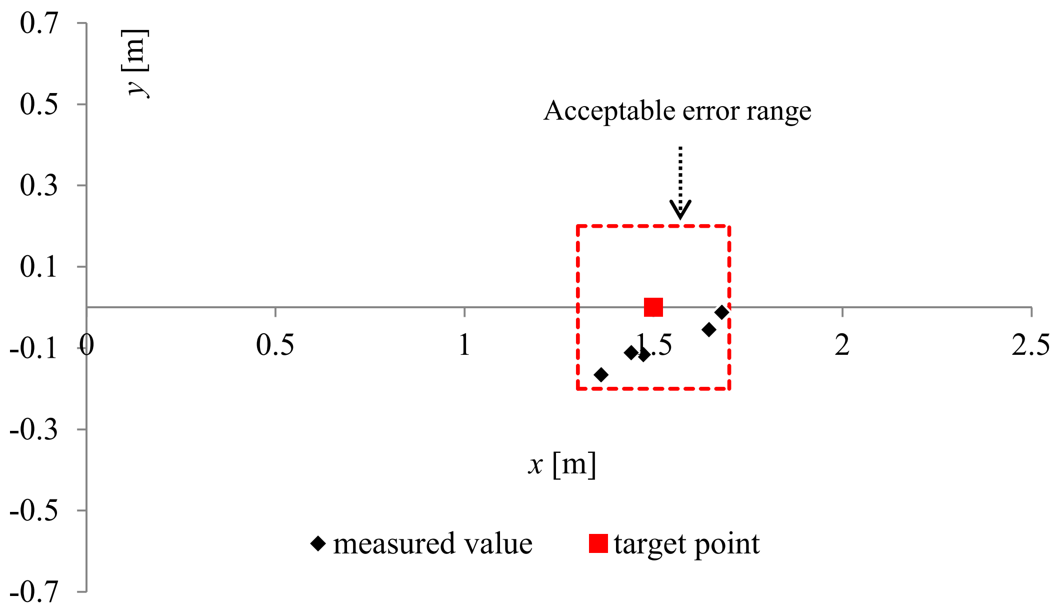

Fig. 3.20. Positioning accuracy of the spout for configuration 1.

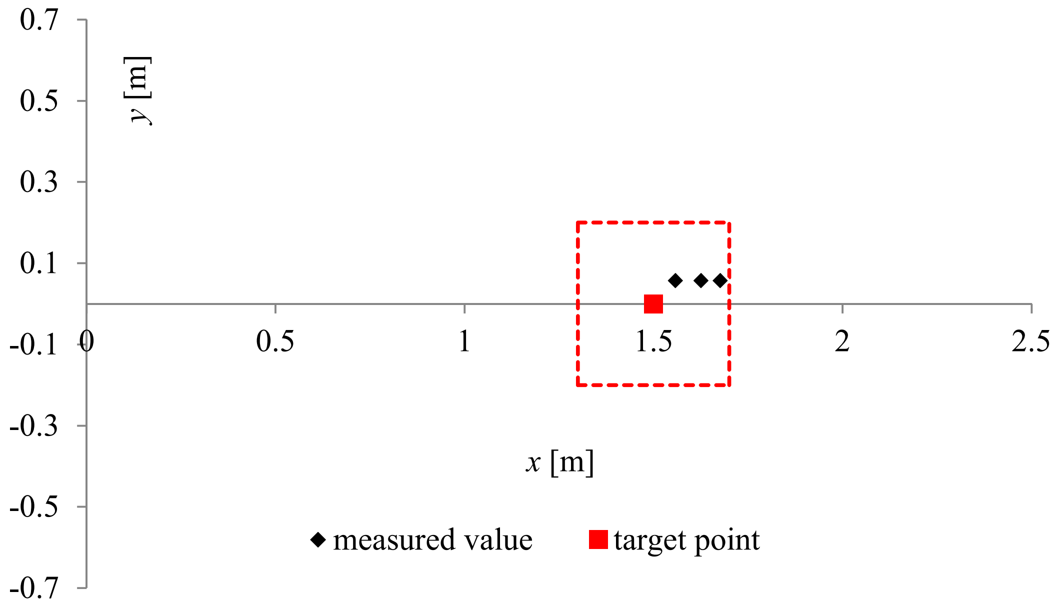

Fig. 3.21. Positioning accuracy of the spout for configuration 2.

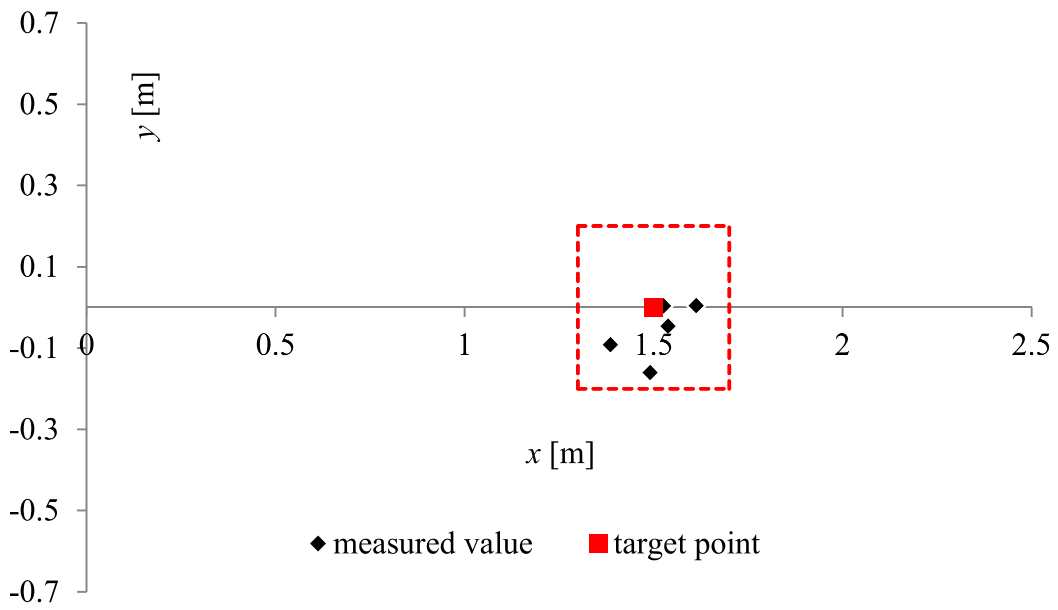

Fig. 3.22. Positioning accuracy of the spout for configuration 3.

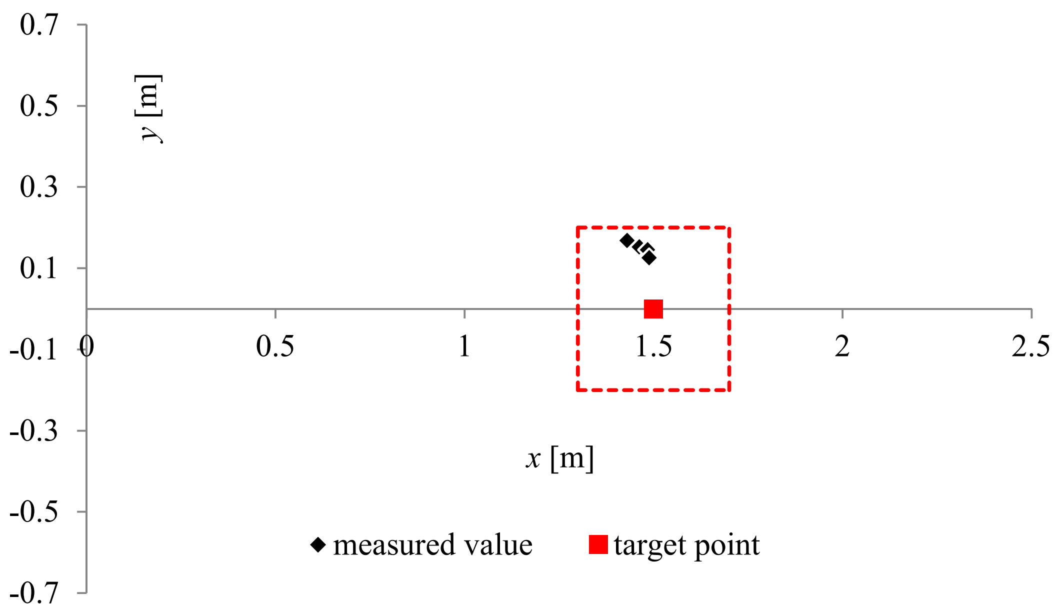

Fig. 3.23. Positioning accuracy of the spout for configuration 4.

In Fig. 3.20 to Fig. 3.23, the solid red square denotes the target point (1.5, 0) (c.f. Fig. 3.15) that is preliminarily assigned in the software program. The dashed-line-square represents the acceptable error range, (i.e., 1.5 ± 0.2, 0 ± 0.2). Figure 3.20 to Fig. 3.23 show that the spout was positioned within this range for all tests. Some tests resulted in the same measured value. Thus, a few markers overlap in these figures.

Table 3.7 shows the maximum error, the mean error, and the RMSE from the true value (1.5, 0), i.e., initially assigned target point. RMSE is about 0.1 m in both x and y direction. The maximum error (0.180, 0.168) is also less than 0.2 m, which falls within the acceptable error range in both directions.

Table 3.7. Positioning errors of auger spout.

	x [m]	y [m]
Max	0.180	0.168
Mean	0.082	0.081
RMSE	0.101	0.098

Some possible sources for these positioning errors may be the resolution of the camera, positioning accuracy of the unloading auger, flexure of the fiducial marker, and errors with camera installation parameters and the link parameters. In particular, the resolution of the camera and the positioning accuracy of the unloading auger are critical. Although the flexure of the fiducial marker and measurement precision may be sources of errors, they are not as critical for resolution and positioning accuracy. This was established by testing two types of fiducial marker, namely a plywood board (relatively flexible) and an aluminum board (relatively flat). However, neither of the boards made any significant difference. The camera elevation angle and the lengths l_a, l_b, l_c, l_d, l_e were measured five times, however, their values were almost the same. In addition, the measurement precision values were only a few centimeters and few degrees, which geometrically resulted in an error of only a few centimeters in the spout position. With respect to positioning accuracy, this can result in a maximum error of about 5 - 6 cm. The combine harvester cannot perfectly position its unloading auger to the input angles (c.f. Fig. 3.19), which is mainly due to the inertia of the auger's rotating movement. Among the relative positions in Fig. 3.20 to Fig. 3.23, the measured plots are scattered in the x directions for position 1 and 3. The inertia is assumed to be the cause of the scattering (c.f. Fig. 3.19). It is inevitable that the proposed system will include this type of error.

In this study, ARToolKit was used to determine the relative position between the unloading auger and the fiducial marker. The required joint angles of the unloading auger were calculated at rate of about 20 frames per second, and the latest average of the joint angles for every 30 frames was used for positioning the unloading auger to the target joint angles. The relative position between the unloading auger and the fiducial marker, as determined by ARToolKit, varied for the same position, depending on the sunlight and shadow. Thus, we confirmed the variation of the target joint angles of the unloading auger at the same position. In this test, the unloading auger is kept static at arbitrary positions where the fiducial marker is caught by the camera. The standard deviations of the angles calculated with 350 frames were 0.01° and 0.01° for θ_1 and θ_2, respectively. Thus, the variations of the target joint angles determined by ARToolKit were sufficiently small, and ARToolKit has sufficient reliability to determine the relative position between the unloading auger and the fiducial marker.

3.7. Conclusions

In this chapter, a machine vision system was developed for autonomous unloading operations. Based on the machine vision system, the joint angles to position the auger spout to a target point to discharge grain were calculated. The main findings and results are summarized as follows.

1. The developed machine vision determined the relative position between the auger spout of the unloading auger and the grain storage container using ARToolkit. The machine vision system detects a fiducial marker from input images captured with a USB camera attached to the unloading auger.

2. A position control system for the unloading auger was developed. The unloading auger was modeled as a 2-DOF manipulator. The target joint angles of the unloading auger were determined from the visual information obtained by the machine vision system for positioning the spout at the preliminarily assigned target point.

3. An acceptable error range for auger positioning was defined from consideration of the relationship between the auger spout and the grain storage container.

4. The experiments confirmed the positioning accuracy of the spout. The actual positions of the auger spout were measured with a total station. The results show that the auger spout can be positioned to a target point with sufficient accuracy. RMSE is about 0.1 m and the maximum error is within 0.2 m in both x and y directions.

The experimental results suggest that the present system is capable to bring the auger in a correct position for automatically unloading grain from the combine to the grain storage container without any loss.

REFERENCES

[1] Ishida, M., Imou, K., Okado, A., Takenaga, H., Honda, Y., Itokawa, N. and Shibuya, Y: Autonomous tractor for forage production. Journal of JSAM. 60(2): 59-66, 1998.

[2] Takai, R., Barawid, O. Jr., Ishii, K. and Noguchi, N: Development of Crawler-Type Robot Tractor based on GPS and IMU, Preprint of the IFAC International Conference on AGRICONTROL 2010, A3-5, Kyoto, Japan, 2010.

[3] Sato, J., Shigeta, K. and Nagasaka, Y: Automatic Operation of a Combined Harvester in a Rice Field. *Proceedings* of the 1996 IEEE/SICE/RSJ International Conference on Multisensor Fusion and Integration for Intelligent Systems, 86-92, Washington, DC, USA, 1996.

[4] Nagasaka, Y., Umeda, N., Kanetani, Y., Taniwaki, K. and Sasaki, Y: Automated rice transplanter using global positioning and gyroscopes. Computers and Electronics in Agriculture, 43(3), 223-234, 2004.

[5] Iida, M. and Yamada, Y: Rice harvesting operation using an autonomous combine with a GPS and a FOG. *Proceedings* of the Conference of Automation Technology for Offroad Equipment 2006, ASAE, 125-131, 2006.

[6] Iida, M., Uchida, R., Zhu, H., Kurita, H., Suguri, M. and Masuda, R: Development of robotic head-feeding combine. *Proceedings* of the CIGR Internationla Symposium on “Sustainable Bioproduction –Water, Energy, and Food”, Tokyo, Japan, 20HOS3006, 2011.

[7] Iida, M., Uchida, R., Zhu, H., Ohdoi, K., Suguri, M., Kurita, H., Masuda, R. and Inamura, T: Development of head-feeding combine robot. *Proceedings* of the 6th International Symposium on Machinery and Mechatronics for Agriculture and Biosystems Engineering (ISMAB) 2012, Jeonju, Korea, 2012.

[8] Uchida, R., Iida, M., Zhu, H., Kurita, H., Suguri, M. and Masuda, R: Path following control for head-feeding combine robot. Transactions of the Society of Instrument and Control Engineers. vol. 49, no. 1, 119-124, 2013.

[9] Iida, M., Uchida, R., Zhu, H., Suguri, M., Kurita, H. and Masuda, R: Path-following control for a head-feeding combine robot. Engineering in Agriculture, Environment and Food, Accepted October 12, 2012.

[10] Madsen, T. E., Kirk, K. and Blas, M. R: 3D camera for forager automation. *Proceedings* of the 67th Conference: LAND. TECHNIK - Agricultural Engineering 2009, 147-152, Hannover, Germany, 2009.

[11] Möller, J: Computer vision – A versatile technology in automation of agriculture machinery. Keynote report of 21th Annual Meeting of the Club of Bologna, EIMA 2010, Bologna, Italy, 2010.

[12] Happich, G., Harms, H.H. and Lang, T: Loading of agricultural trailers using a model-based method. The CIGR EJournal, Manuscript 1187, Vol. XI, 2010.

[13] Lepetit, V. and Fua, P: Monocular-based 3D tracking of rigid objects. Now Publishers Inc., MA, USA, 1-3, 2005.

[14] Claus, D. and Fitzgibbon, A. W: Reliable fiducial detection in natural scenes, Lecture notes in Computer Science, Vol. 3024, 469-480, 2004.

[15] Koller, D., Klinker, G., Rose, E., Breen, D., Whitaker, R. and Tuceryan, M: Real-time vision-based camera tracking for augmented reality applications. *Proceedings* of the Symposium on Virtual Reality Software and Technology (VRST-97), 87-94, Lausanne, Switzerland, 1997.

[16] Kato, H. and Billinghurst, M: Marker tracking and HMD calibration for a video-based augmented reality conferencing system. *Proceedings* of the 2nd IEEE and ACM International Workshop on Augmented Reality, 85-94, San Francisco, USA, 1999.

[17] Billinghurst, M., Kato, H. and Poupyrev, Ivan: The magicbook: a transitional AR interface. Computer & Graphics, vol. 25, 745-753, 2001.

[18] Billinghurst, M. and Kato, H: Collaborative augmented reality. Communications of the ACM, vol. 45, No. 7, 64-70, 2002.

[19] Billinghurst, M., Kato, H., Kiyokawa, K., Belcher, D. and Poupyrev, I: Experiments with face-to face collaborative AR interfaces. Virtual Reality, vol. 6, issue 3, 107-121, 2002.

[20] Hedley, N. R., Billinghurst, M., Postner, L., May, R. and Kato, H: Explorations in the use of Augmented Reality for geographic visualization. Teleoperators and Virtual Environments – Mixed reality. vol. 11, issue 2, 119-133, 2002.

[21] Farbiz, F., Cheok, A. D., Wei, Liu., ZhiYing, Z., Ke, X., Prince, S., Billinghurst, M. and Kato, H: Live three-dimensional content for Augmented Reality. IEEE Transactions on Multimedia, vol. 7, no. 3, 514-523, 2005.

[22] Gonzalez, R. C. and Wintz, P: Digital Image Processing 2^{nd} Edition. Addison-Wesley Publishing Company, MA, USA, 36-52, 1987.

[23] Xu, G. and Zhang, Z: Epipolar Geometry in Stereo, Motion and Object Recognition: A Unified Approach. Kluwer Academic Publishers Norwell, MA, USA, 7-16, 1996.

[24] Sturm, P. F. and Maybank, S. J: On plane-based camera calibration: A general algorithm, singularities, applications. IEEE Computer Society Conference on Computer Vision and Pattern Recognition, vol. 1, 1999.

[25] Zhang, Z: A flexible new technique for camera calibration. IEEE Transactions on Pattern Analysis and Machine Intelligence. vol. 22, issue 11, 1330-1334, 2000.

[26] Rekimono, J: Matrix: A realtime object identification and registration method for augmented reality. *Proceedings* of the 3rd Asia-Pacific Computer and Human Interaction, 63-68, Kanagawa, Japan, 1998.

[27] Denavit, J. and Hartenberg, R. S: A Kinematic Notation for Lower-Pair Mechanisms Based on Matrices. ASME Journal of Applied Mechanics, vol. 77, 215-221, 1955.

[28] Asada, H. and Slotine, J. –J. E: Robot Analysis and Control. Wiley-Interscience Publication, NY, USA, 15-50, 1986.

[29] Paul, R. P: Robot Manipulators. MIT Press, Cambridge, England, 41-81, 1981

[30] Yoshikawa, T: Foundations of Robot Control. Corona Publishing Co., Ltd., Tokyo, Japan, 11-68, 1988.

CHAPTER 4

SEARCHING FOR FIDUCIAL MARKER BY AUGER CAMERA

4.1. Introduction

In the previous chapter [1], a method that utilizes image processing technique for positioning the unloading auger to an appropriate location to unload grain was introduced. The experimental results demonstrate this method can position the auger spout to a specified target point with sufficient horizontal accuracy, when viewed from above the grain storage container. In the experiment, however, positioning was conducted assuming the fiducial marker had already been located by the camera attached to the unloading auger. A combine robot is required to search for and detect the fiducial marker automatically and with certainty. In addition, two software program modules were used in that experiment, one for the communication between the combine and a laptop PC and then the control of the combine, and the other for image processing and calculation of the target joint angles. Obviously, these two functions should be integrated into a more practical method for autonomous unloading. Thus, the autonomous fiducial marker searching function needs to be pursued.

In searching for the marker the issue of work efficiency is involved. One of the most important concerns for automation of agricultural machinery [2] is that time costs associated with agricultural operations using an autonomous machine should not be much longer than that required to do the same operation manually. It goes without saying that the autonomous operation time should preferably be shorter. Thus, the autonomous unloading system should be designed so that the fiducial marker can be located smoothly and integrated into the autonomous unloading operation in time efficient manner.

A strategy for efficiently locating the fiducial marker is closely linked to the camera's field of view (FOV). The coverage of the camera's FOV is quite an important factor for visual servoing, and thereby has been widely studied by researchers concerned with mobile robots [3], [4], especially by those who have developed a robot that searches for a particular object [5].

Similar problems have also been studied in other fields. For instance, the efficient placement of basement stations for wireless networks has been studied in the field of wireless sensor networks or mobile sensor networks [6], [7]. Researchers in urban engineering have a keen interest in effectively arranging security cameras to obtain the most secure coverage with the least number of cameras [8]-[10]. Although these problems are for different applications or regions of interest, essentially they are the same in terms of optimization of coverage. Thus, the methodology presented in these fields can be suggestive in the efficient locating of a fiducial marker.

The objectives of this chapter are as follows:

1. To compute the FOV of the auger camera based on the pinhole camera model.

2. To determine the optimal placement of the camera based on the simulation results.

3. To propose a fiducial marker searching method for efficiently searching and accurately detecting the marker.

4. To examine the actual performance of the presented method on the combine robot.

4.2. Unloading Operation by Combine Robot

In the previous chapter, it was assumed that the fiducial marker had already been detected. In fact, however, the combine robot requires a procedure to search for and detect the fiducial marker. Before entering into detailed discussion, it will be helpful to summarize the overall concept and the assumptions of the system. When the grain tank of the combine robot is full, the robot is supposed to stop harvesting and autonomously return to the assigned point by GPS navigation, where it will unload grain into the grain storage container. This point will be previously given as GPS data. Even if the combine robot can travel to the point autonomously, the pickup truck may be parked at the position with some position errors. Figure 4.1 illustrates an overview of the presumed situation after returning to this assigned point. The combine is located in a paddy field alongside the pickup truck that is on a farm road. As described in Chapter 2, the combine robot harvests rice crops in a counter-clockwise fashion (see Fig. 2.9). Thus, in this study, the truck is supposed to be always located on the right side of the combine robot.

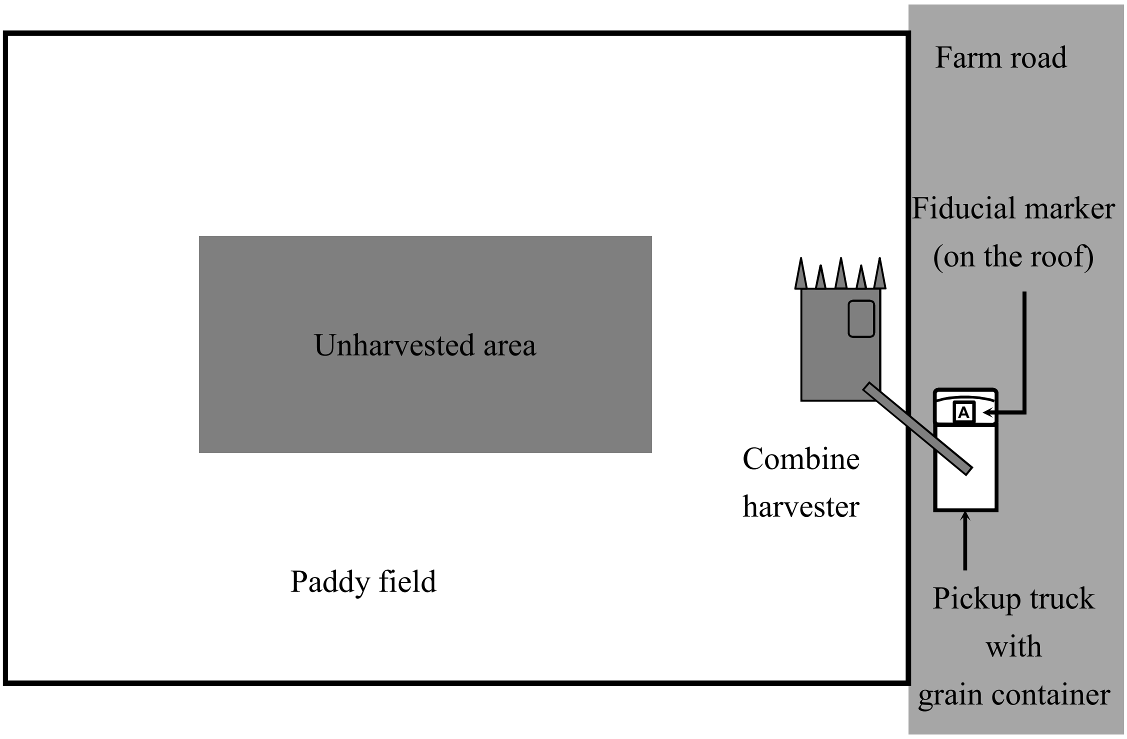

Fig. 4.1. Assumed situation for autonomous unloading operation.

Figure 4.2 shows the actual arrangement of the combine with an auger camera (a USB camera), the pickup truck with a grain storage container and a fiducial marker located on its roof. In Fig. 4.3, the combine is actually unloading the grain.

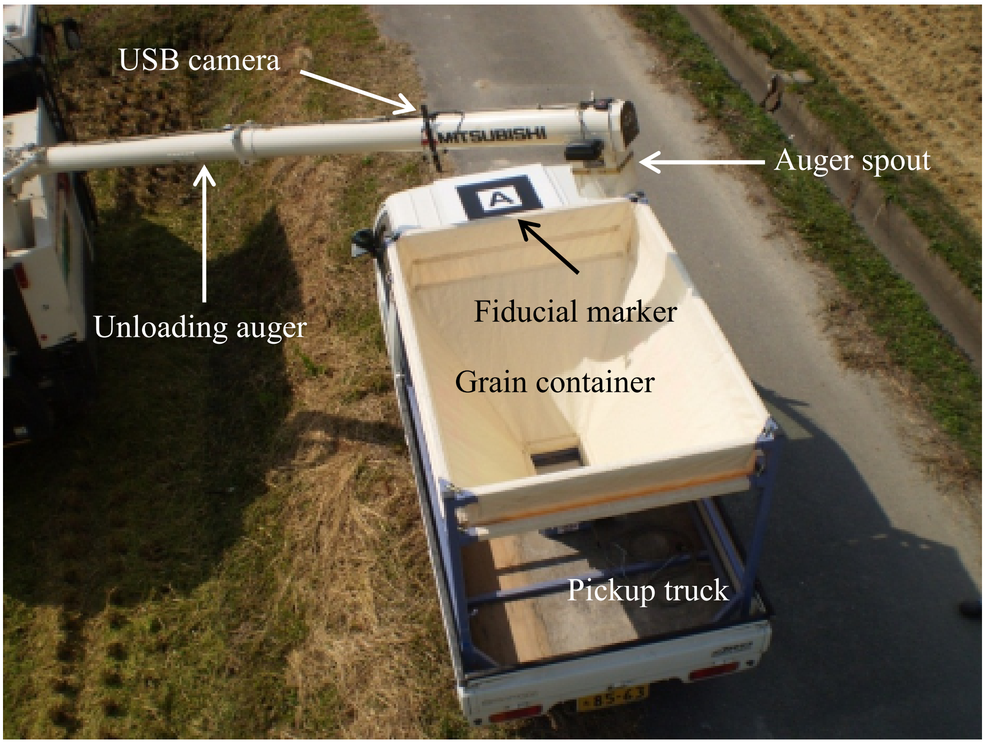

Fig. 4.2. Unloading auger, pickup truck with grain container and fiducial marker on which 'A' is printed.

Fig. 4.3. Combine harvester unloading grains into grain container.

To search for the fiducial marker as efficiently as possible, the FOV of the auger camera needs to be considered. The system should search for the fiducial marker in such a way that it does not need to retrace the same area repeatedly. In other words, the auger camera is required to sweep over the whole operational area, without any overlap as far as possible, in order to consistently and accurately locate the fiducial marker. It is necessary to exhaustively examine the FOV in order to optimize the search procedure. Thus, in the following section, the FOV of the auger camera is computationally simulated for various decisive parameters, and the effective searching procedure is presented based on the simulation results.

4.3. Analysis of the Installation of the Auger Camera

4.3.1. Simulation Model for FOV of Auger Camera

The FOV of a camera represents the extent of its visible field. Since the fiducial marker is placed on the roof of the truck (c.f. Fig. 4.2 and Fig. 4.3), the FOV at roof height needs to be focused on. Usually, a rice paddy is enclosed by embankments and by at least one farm road, the height of which is usually higher than the paddy ground. Although the height of the adjacent farm road from a paddy field (denoted h_{fr} hereafter) varies between fields, it is sufficient to consider only two cases, which will be described below.

In this study, a 2-DOF manipulator was adopted as the kinematic model of the unloading auger, as in Chapter 3, and the coordinate systems were assigned [1], [11] (see Fig. 3.5 to Fig. 3.7). An arbitrary position on these coordinate systems was calculated as the kinematics problem of the manipulator [12]-[14]. Some approximations are made for the model, and these will be explained later. Let the height of the origin of Σ_0 be h_c and the height of the pickup truck be h_{kt}. More precisely, h_c is the height, above the ground, of the origin of Σ_0, the orthogonal coordinate system set on the combine. h_{kt} is the height of the roof of the pickup truck above the ground of the farm road.

In general, the FOV can be represented by its angle of view (AOV), and depth of field D. AOV is represented in terms of the vertical AOV and the horizontal AOV. The depth of field represents the area of the visual scene that is acceptably sharp. Provided a target object is of an acceptable level of sharpness, D of a camera spans from D_{min} to D_{max} [15]. Outside of this range, images are blurred. In fact, D depends on the focal length of the camera. The focal length of the camera used in this study was kept constant, such that D falls within an acceptable range of sharpness. D was empirically determined and at the same time, it is also experimentally confirmed that the target plane (i.e., roof of the truck, or fiducial marker) forms an image with sufficient sharpness, as far as h_{fr} varies within an expected range. The range was assumed to be 0 m < h_{fr} < 1.5 m in this study, based on actual and usual rice paddy field conditions.

Further approximations were applied to the system model. In the following analysis, the unloading auger was dealt with as a line, not a solid object. And the camera's dimensions were neglected. Hence, l_a, l_d and l_e in the model could be equal to zero. Table 4.1 summarizes the lengths of l_a, l_b, l_c, l_d and l_e in the following simulation. In addition, a pinhole camera model [16], [17] was used.

Table 4.1. Link parameters in simulation.

l_a [mm]	l_b [mm]	l_c [mm]	l_d [mm]	l_e [mm]
0	4,280	3,195	0	0

Although it may be considered that l_c is also a decisive variable for the FOV, in fact, l_c cannot be varied from the position shown in the table. Obviously, the camera needs to be attached at the top of the unloading auger for obtaining as large a FOV as possible. When attached to the spout, however, the camera cannot obtain a clear image because of the dust that flows out of the spout during the unloading operation. Thus, the camera was attached at a position as close to the auger spout as possible, but not being obstructed by dust from the unloading operation. This position was empirically determined and regarded as constant in the whole study.

a) Case 1

In the case that h_c is longer than h_{kt} + h_{fr}, the camera's FOV and the associated parameters are depicted in Fig. 4.4-(a) and Fig. 4.4-(b). Both figures represent the cross-sectional view at Y_0-Z_0 plane. For the sake of ease in consideration, θ_1 is kept at 90° in these figures.

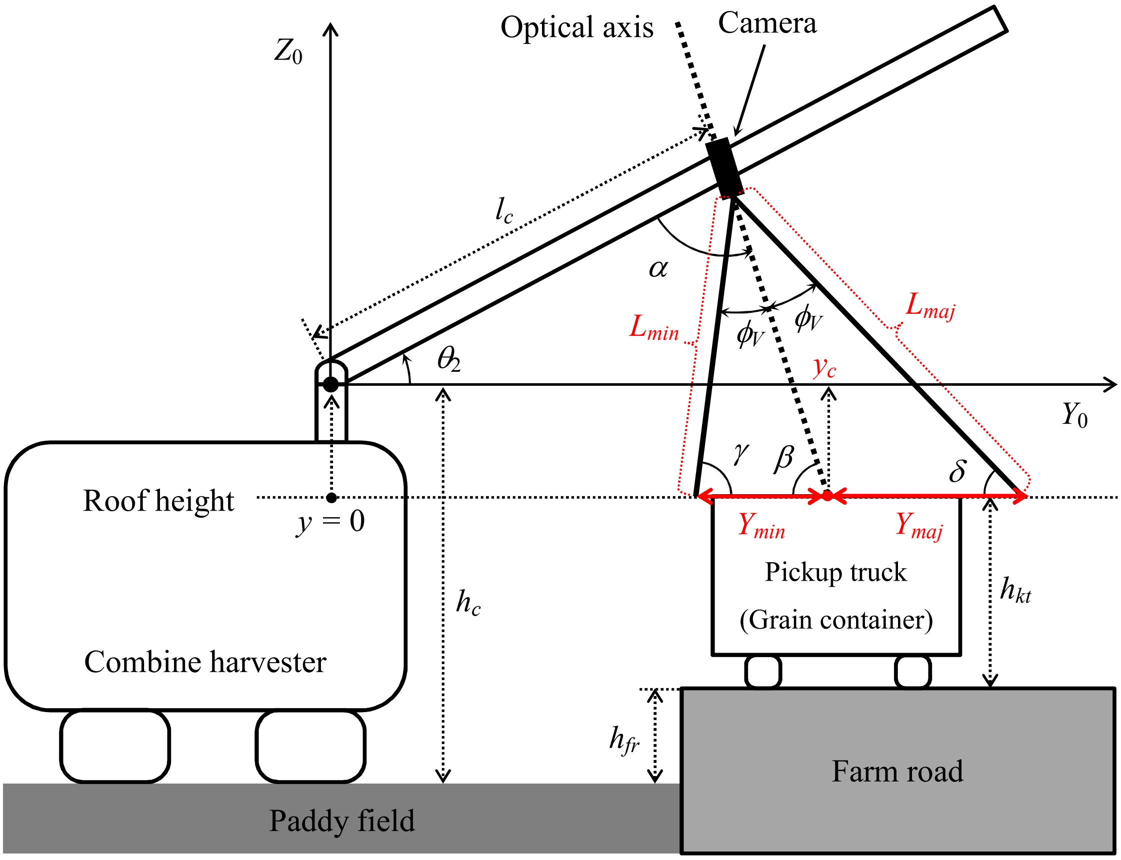

Fig. 4.4-(a). Cross-sectional view at Y_0-Z_0 plane when $h_c > h_{kt} + h_{fr}$.

In Fig. 4.4, α is the camera's elevation angle and ϕ_V is half the vertical AOV. The FOV at the height of the fiducial marker on the roof is divided by the optical axis (a point y_c in Fig. 4.4) into two parts, whose length along Y_0 axis are Y_{min}, which is closer to the combine and Y_{maj}, which is far from it. L_{min} and L_{maj} are the distance between the upper or the lower edge of the FOV at the roof height and the optical center, respectively. Regarding other parameters in the figure, l_c is the distance between the camera and the origin of Σ_0. And β, γ and δ are defined as follows.

$$\beta = \pi - (\theta_2 + \alpha). \tag{4.1}$$

$$\gamma = \pi - (\beta + \phi_V). \tag{4.2}$$

$$\delta = \pi - (\theta_2 + \alpha + \phi_V). \tag{4.3}$$

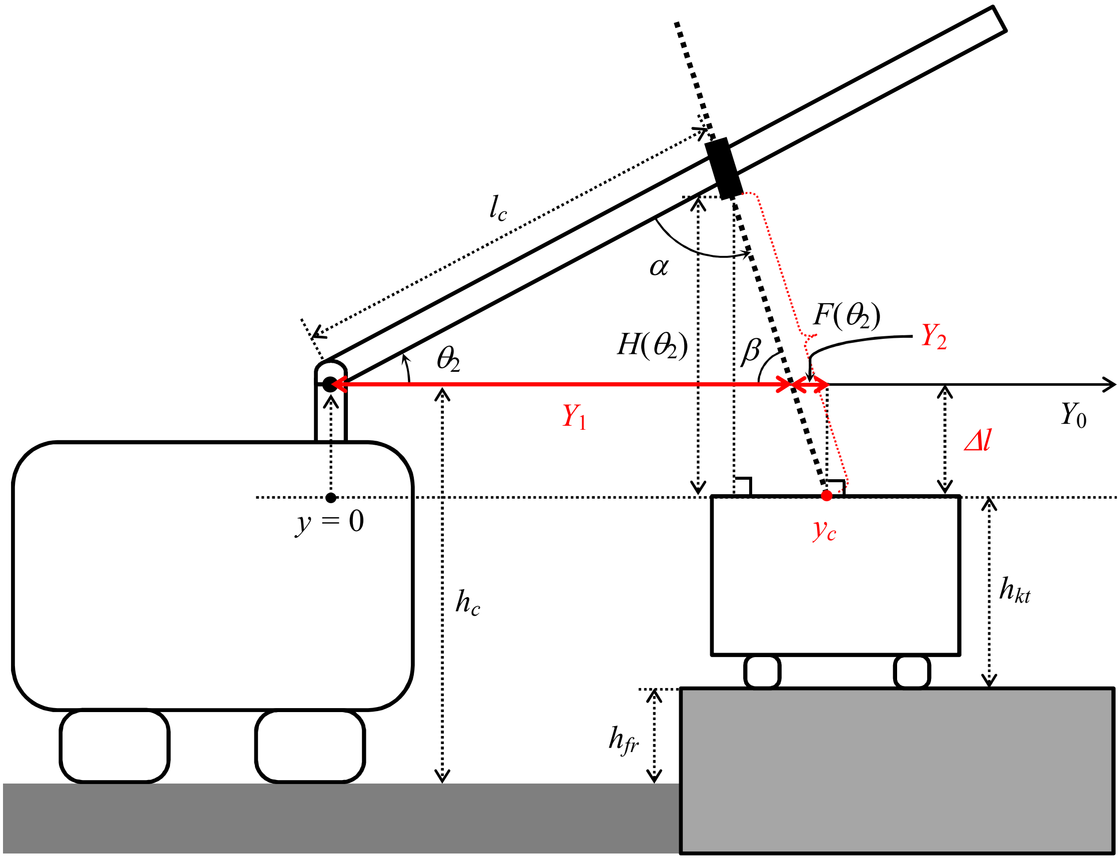

Fig. 4.4-(b). Cross-sectional view at Y_0-Z_0 plane when $h_c > h_{kt} + h_{fr}$.

In Fig. 4.4-(b), $H(\theta_2)$ is the height of the optical center above the roof. $F(\theta_2)$ is defined as the distance between the optical center and the roof height along the optical axis. On the Y_0 axis, Y_1 denotes the coordinate of the intercept by the optical axis and Y_2 is defined as $y_c - Y_1$. Lastly, when $h_c > h_{kt} + h_{fr}$, Δl is calculated by $h_c - (h_{kt} + h_{fr})$.

Under these definitions, the camera's FOV is calculated based on the elementary geometry: If $h_c > h_{kt} + h_{fr}$, $H(\theta_2)$ is described in Eq. (4.4).

$$
\begin{aligned}
H(\theta_2) &= l_c \sin\theta_2 + \Delta l \\
&= l_c \sin\theta_2 + \left(h_c - h_{fr} - h_{kt}\right).
\end{aligned}
\tag{4.4}
$$

Thus, L_{min}, L_{maj} and $F(\theta_2)$ are represented using $H(\theta_2)$ as follows.

$$L_{min} = \frac{H(\theta_2)}{\sin\gamma} = \frac{H(\theta_2)}{\sin(\beta + \phi_V)} = \frac{H(\theta_2)}{\sin(\theta_2 + \alpha - \phi_V)}. \tag{4.5}$$

$$L_{maj} = \frac{H(\theta_2)}{\sin\delta} = \frac{H(\theta_2)}{\sin(\theta_2 + \alpha + \phi_V)}. \tag{4.6}$$

$$F(\theta_2) = \frac{H(\theta_2)}{\sin\beta} = \frac{H(\theta_2)}{\sin(\theta_2 + \alpha)}. \tag{4.7}$$

And then, Y_{min} and Y_{maj} are calculated as the following equations.

$$Y_{min} = \sqrt{\{F(\theta_2)\}^2 + {L_{min}}^2 - 2F(\theta_2)L_{min}\cos\phi_V}. \tag{4.8}$$

$$Y_{maj} = \sqrt{\{F(\theta_2)\}^2 + {L_{maj}}^2 - 2F(\theta_2)L_{maj}\cos\phi_V}. \tag{4.9}$$

The value of y_c is also obtained in Eq. (4.10).

$$y_c = Y_1 + Y_2 = \sqrt{\{F(\theta_2)\}^2 + {l_c}^2 - 2F(\theta_2)l_c\cos\alpha} + \frac{\Delta l}{\tan\beta} = \sqrt{\{F(\theta_2)\}^2 + {l_c}^2 - 2F(\theta_2)l_c\cos\alpha} + \frac{h_c - h_{fr} - h_{kt}}{\tan(\theta_2 + \alpha)}. \tag{4.10}$$

Figure 4.5 shows the camera's FOV and the parameters that are also illustrated in Fig. 4.4. To make the figure clearer, the plane that includes the line of L_{min} and the lower edge is clipped and translated in the left side.

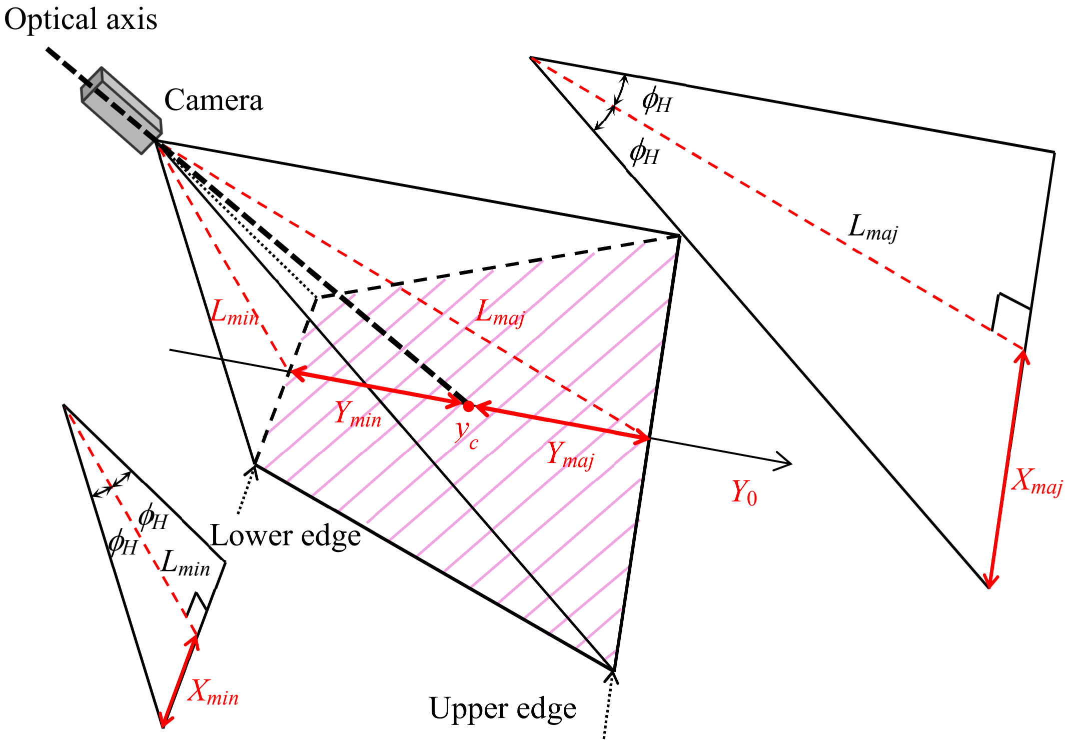

Fig. 4.5. Conceptual image of FOV.

Here, ϕ_H is half the horizontal AOV. X_{min} is half the bottom length of the rectangular triangle that consists of an angle of ϕ_H and a line segment whose length is L_{min}. Similarly, the plane that includes the line of L_{maj} and the upper edge is depicted separately in the right side and X_{maj} is defined as well as X_{min}. Once L_{min} and L_{maj} are known, X_{min} and X_{maj} can be obtained as follows.

$$X_{min} = L_{min} \tan \phi_H. \tag{4.11}$$

$$X_{maj} = L_{maj} \tan \phi_H. \tag{4.12}$$

Finally, the FOV at the roof height can be simulated using the parameters of y_c, X_{min}, X_{maj}, Y_{min} and Y_{maj}.

b) Case 2

It is necessary to consider separately the case when h_c is lower than h_{kt} + h_{fr}. The camera's FOV and the associated parameters are illustrated in Fig. 4.6-(a). γ' is the supplementary angle of γ. As well as Fig. 4.4-(b), Fig. 4.6-(b) can be helpful.

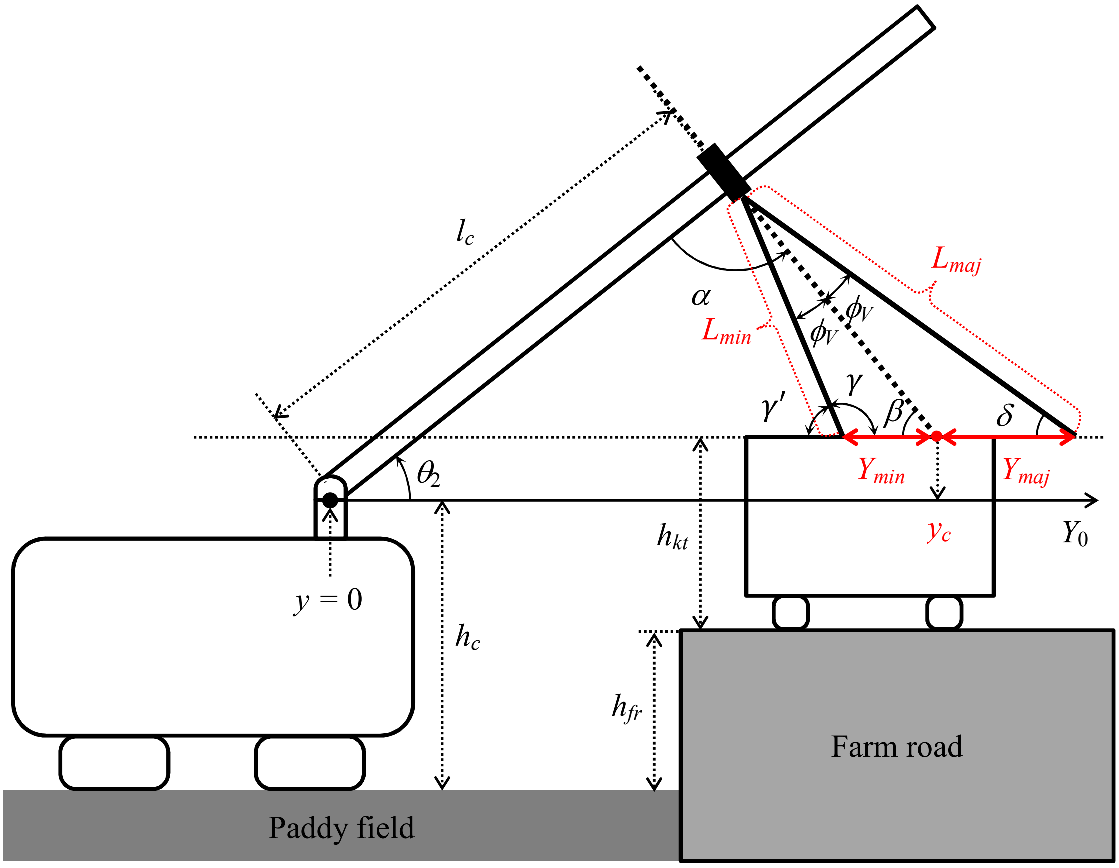

Fig. 4.6-(a). Cross-sectional view at Y_0-Z_0 plane when $h_c < h_{kt} + h_{fr}$.

In this case, the roof height is located above the origin of Σ_0. The intersection of the unloading auger and the roof height is marked as a red square in the figure, and the length between this point and the origin of Σ_0 along the unloading auger is represented by l_Δ. Now, Δl is defined as h_{kt} + h_{fr} − h_c, and thus $H(\theta_2)$ is described in slightly different form.

$$\begin{aligned} H(\theta_2) &= l_c \sin\theta_2 + \Delta l \\ &= l_c \sin\theta_2 - (h_c - h_{fr} - h_{kt}). \end{aligned} \tag{4.13}$$

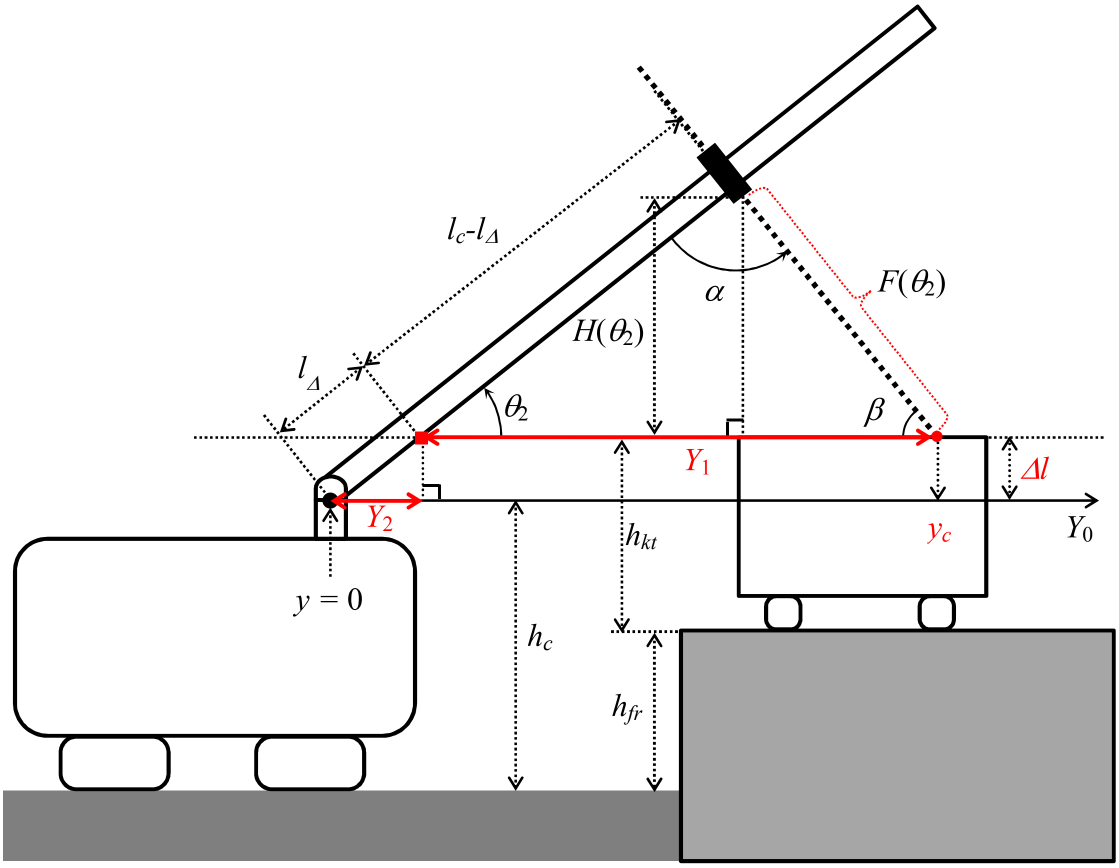

Fig. 4.6-(b). Cross-sectional view at Y_0-Z_0 plane when $h_c < h_{kt} + h_{fr}$.

Moreover, a modification must be made to Eq. (4.5), although the form itself is finally equal.

$$
\begin{aligned}
L_{min} &= \frac{H(\theta_2)}{\sin\gamma'} \\
&= \frac{H(\theta_2)}{\sin(\beta+\phi_V)} \\
&= \frac{H(\theta_2)}{\sin(\theta_2+\alpha-\phi_V)}.
\end{aligned}
\tag{4.14}
$$

Except for these changes, L_{maj}, $F(\theta_2)$, Y_{min} and Y_{maj} are calculated in the same manner as represented in Eq. (4.6) to Eq. (4.9), respectively, although the value of y_c requires different consideration as shown in Fig. 4.6-(b).

$$y_c = Y_1 + Y_2$$

$$= \sqrt{\{F(\theta_2)\}^2 + (l_c - l_\Delta)^2 - 2F(\theta_2)(l_c - l_\Delta)\cos\alpha} + \frac{\Delta l}{\tan\theta_2}, \tag{4.15}$$

where

$$l_\Delta = \frac{\Delta l}{\sin\theta_2}.$$

Concerning X_{min} and X_{maj}, they are obtained in the identical form as the case of $h_c > h_{kt} + h_{fr}$.

In the following description, the simulation result of the camera's FOV is explained with respect to a few decisive variables for FOV. Next, an appropriate assignment of the variables is determined, and finally an effective fiducial marker searching procedure is presented.

4.3.2. FOVs for Joint Angle of Unloading Auger

The simulation was performed under the parameter values shown in Table. 4.2.

Table 4.2. Parameters setting.

	Parameter	Default	Variation	Step
Height	h_c [m]	2.35	const.	-
	h_{kt} [m]	1.79	const.	-
	h_{fr} [m]	0	0 - 1.5	0.5
Camera	α [°]	60 or 90	const.	-
	ϕ_V [°]	24.79	const.	-
	ϕ_H [°]	19.11	const.	-
Unloading auger	θ_1 [°]	0	0 - 180	0.1
	θ_2 [°]	20	20 - 45	10 or 5

Figure 4.7 shows the range of the FOV based on the combine-based coordinate system (i.e., Σ_0 in Fig. 3.5 and Fig. 3.6), when θ_1 of the unloading auger rotates from 0° to 180°. Note that the point (X_0, Y_0) = (0, 0), which is marked as Origin in the following figures, indicates the origin of Σ_0. Figure 4.7 shows the results for the joint angle θ_2 of the auger: 20°, 30°, 40° and 45°. For the case of θ_1 = 0°, 90° and 180°, the corresponding FOVs are drawn in the figure. In all cases, other variables are kept at α = 60° and h_{fr} = 0.5 m. The figure indicates the whole area where the camera can physically observe for each value of θ_2, although the range of θ_1 is limited from 0° to 180°. Similarly, the other exemplary FOVs are shown in Fig. 4.8, which is the case of α = 90° and h_{fr} = 0.5 m.

Obviously, it is clear that the case of α = 90° offers much larger FOVs than the case of α = 60°. In general, FOV shifts centrifugally as α increases. An appropriate angle of α, however, should not be determined based on only the largeness of FOV, because a larger FOV is not always efficient for fiducial marker searching. This is discussed in next section.

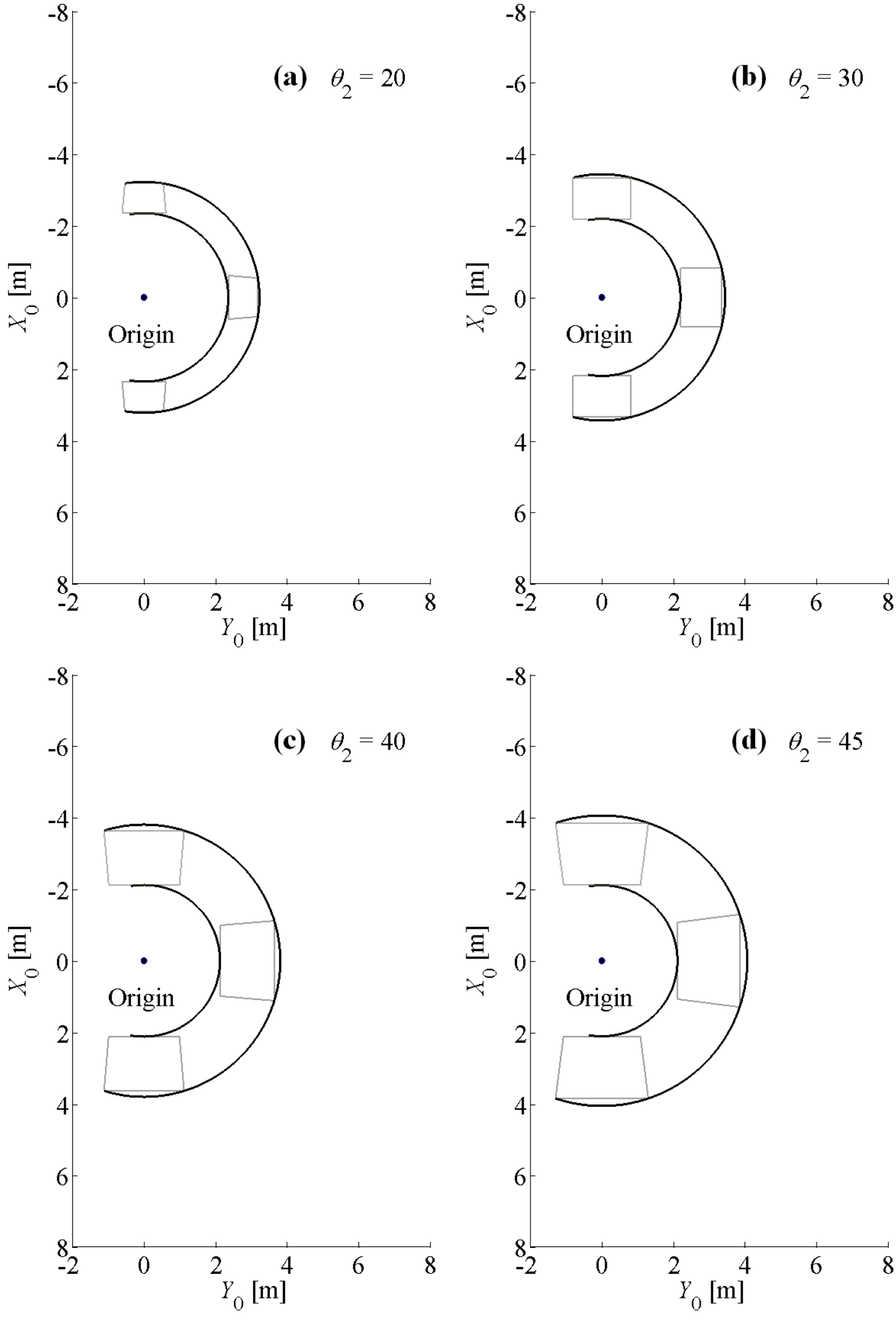

Fig. 4.7. Calculated FOV when $\alpha = 60°$ and $h_{fr} = 0.5$ m.
(a). $\theta_2 = 20°$; (b). $\theta_2 = 30°$; (c). $\theta_2 = 40°$; $\theta_2 = 45°$.

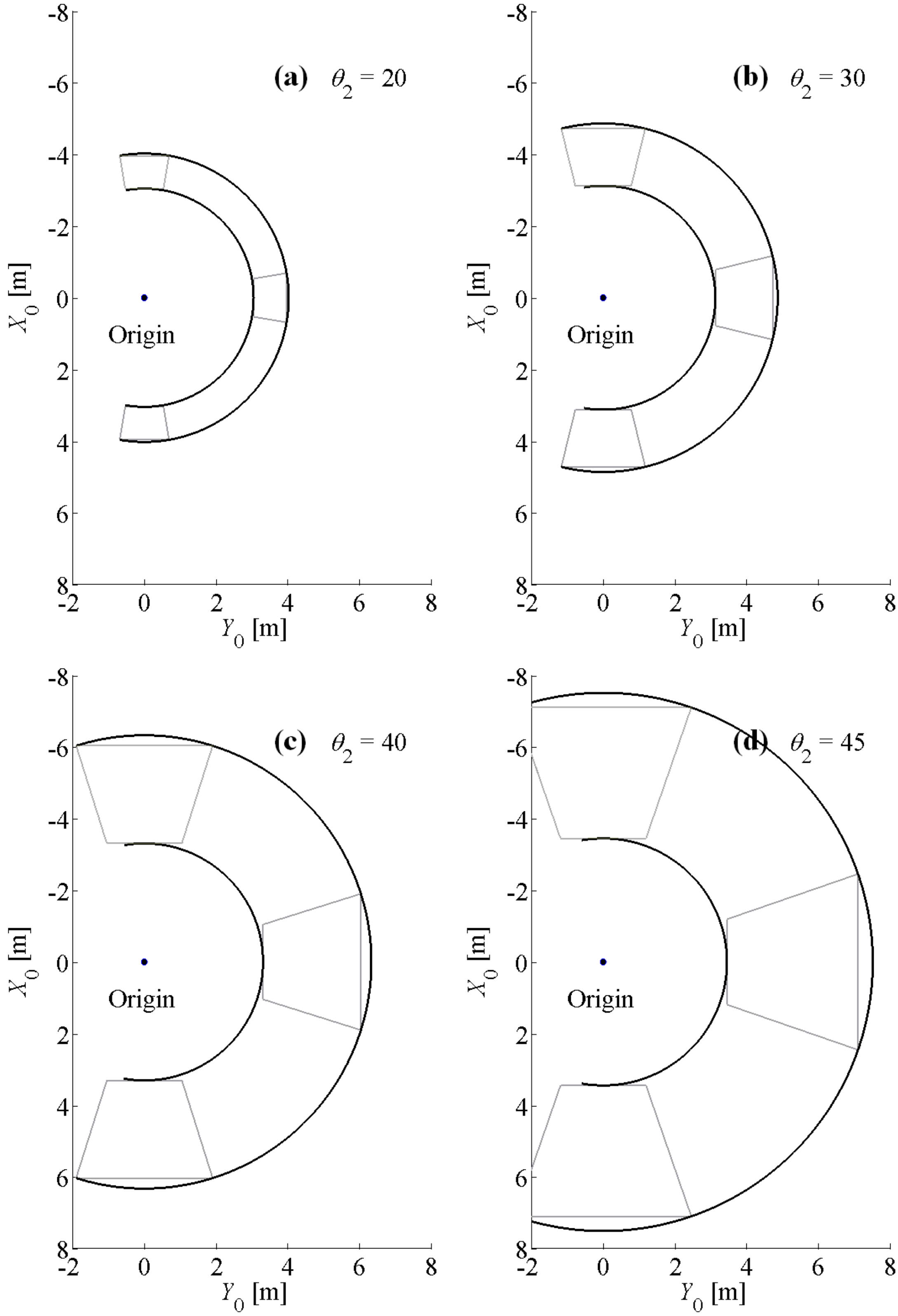

Fig. 4.8. Calculated FOV when $\alpha = 90°$ and $h_{fr} = 0.5$ m.
(a). $\theta_2 = 20°$; (b). $\theta_2 = 30°$; (c). $\theta_2 = 40°$; $\theta_2 = 45°$.

4.3.3. Optimal Camera Installation

In the following, the positional relation between the combine and the pickup truck is as given in Fig. 4.9.

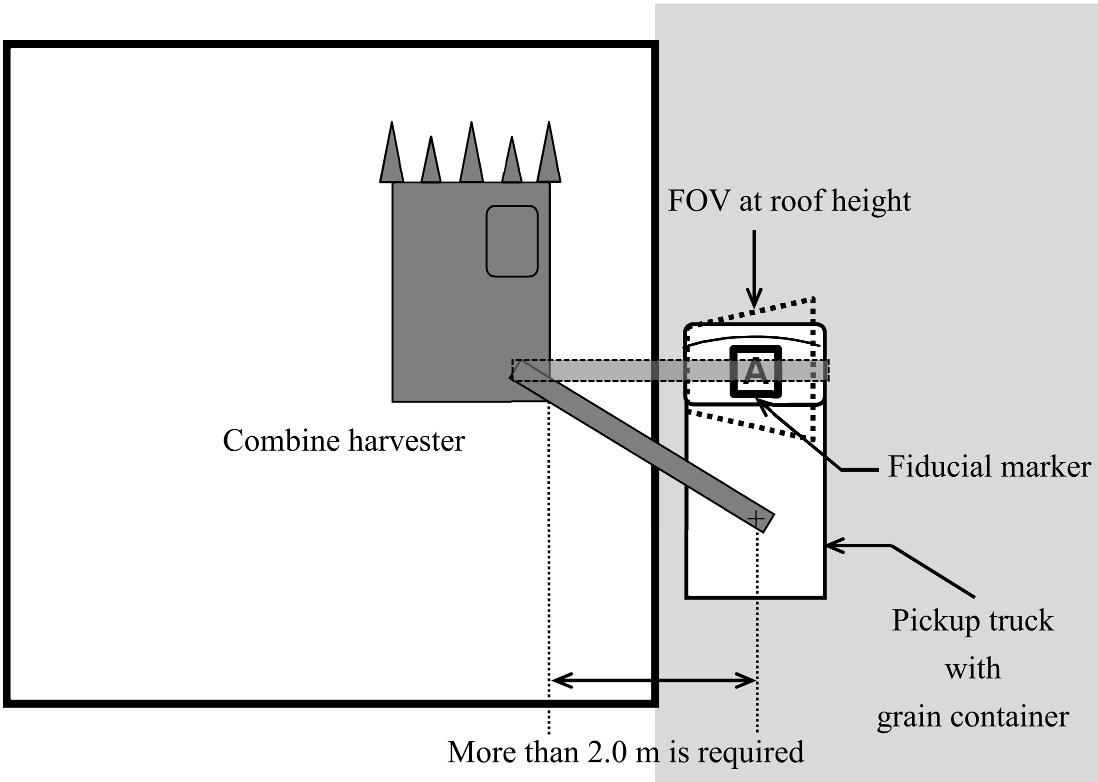

Fig. 4.9. Positional relation between combine harvester and pickup truck.

In general, there is at least 2.0 m between the combine and the target point. This is caused by physical obstacles such as an irrigation canal, the difference in ground level between the paddy field and the farm road, and so on. Thus, in the actual unloading operation, the joint angles are restricted. To ensure more than 2.0 m as a margin, the range of θ_1 is required to satisfy $20° < \theta_1 < 90°$. In addition, θ_2 can be also confined by the value of h_{fr}. In the method presented in Chapter 3, a target point is preliminarily assigned and the joint angles are determined such that the auger spout should be positioned at that point. h_t, the height of the target point from the roof (i.e., from the fiducial marker) is set to 0.5 m. In this case, θ_2 must satisfy the following relation.

$$l_b \sin\theta_2 + h_c = h_{fr} + h_{kt} + h_t \tag{4.16}$$

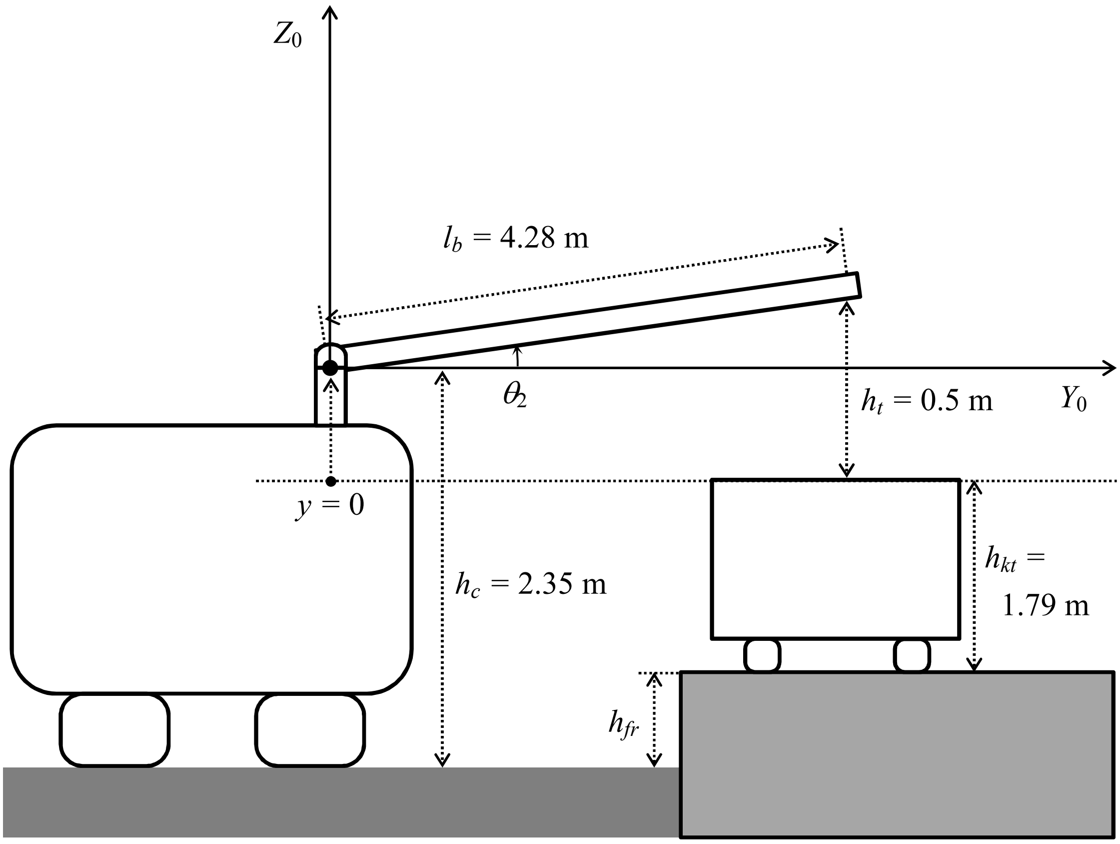

Fig. 4. 10. Cross-sectional view at Y_0-Z_0 plane
when positioning has been ideally performed.

And considering the actual height of h_c, h_{kt} and h_t, the joint angle θ_2 can be approximately calculated as follows.

$$\theta_2 \approx \sin^{-1}\left(\frac{h_{fr}}{l_b}\right). \tag{4.17}$$

Thus, the ideal θ_2 can be estimated for h_{fr}. Concerning the representative values, h_{fr} = 0.0, 0.5, 1.0 and 1.5, the estimated θ_2 is presented in Table 4.3.

Table 4.3. Ideal angle of θ_2 estimated for representative h_{fr}.

h_{fr} [m]	θ_2 [°]
0.0	0.0
0.5	6.7
1.0	13.5
1.5	20.5

Once an ideal θ_2 is provided, the area in which the fiducial marker should be detected can be estimated in accordance with the θ_2 value. And, the value of α should be selected such that the FOV could include the estimated area as much as possible. Conversely, if α is determined in this manner, the fiducial marker is most likely to be covered by the camera's FOV, and then the tip of the spout (referred to as "the auger spout" or just "the spout", hereafter) can be ideally positioned to the target point based on the calculated θ_2 value corresponding to the detected fiducial marker.

In the following figures, the outer and inner border of FOV is shown by the grey finer lines. Let this FOV be the maximal FOV. It is generated from FOVs at every θ_2 value, such as Fig. 4.7 or Fig. 4.8. In short, it shows the whole area the camera can view when θ_2 varies from 20° to 45°. The ideal spout position is denoted by a cross mark for each 5° in the range of $20° < \theta_1 < 90°$. The two thicker lines indicate the outer and inner border of the shaded area in which the fiducial marker is considered to exist corresponding to the ideal spout position.

Again, when the fiducial marker is detected in this area, the target point that is assigned with respect to the detected fiducial marker will be located at the ideal spout position, denoted as a cross. Thus, the maximal FOV should include this shaded area as largely as possible. And the more preferable α can give the larger overlapped region between the maximal FOV and the shaded area.

Figure 4.11 to Fig. 4.14 show the fiducial marker coverage with the maximal FOV when α = 60°, 70°, 80° and 90°, respectively. The overlapped region is shown with red line, while the area that is not covered by the maximal FOV is shown with the black line. These figures show the result for the representative h_{fr} values, 0.0 m, 0.5 m, 1.0 m and 1.5 m, respectively. They are summarized in Table 4.4.

Table 4.4. Parameters setting.

	Parameter	Default	Variation	Step
Height	h_c [m]	2.35	const.	-
	h_{kt} [m]	1.79	const.	-
	h_{fr} [m]	0	0 - 1.5	0.5
Camera	α [°]	60	60 - 90	10
	ϕ_V [°]	24.79	const.	-
	ϕ_H [°]	19.11	const.	-
Unloading auger	θ_1 [°]	0	0 - 180	0.1
	θ_2 [°]	20	20 – 45	10 or 5

*The variation of θ_2 does not appear in the following figures.

From a qualitative point of view, these figures suggest some apparent features. First, the overlapped area decreases as the h_{fr} increases. This is natural because the maximal FOV narrows according to increasing h_{fr}. Second, the maximal FOV itself becomes wider with the increase of α. And as α increases, the maximal FOV, as a whole, shifts centrifugally relative to the shaded area. More specifically, in Fig. 4.11, the black shaded area, which is not included in the maximal FOV, appears outside of the exterior border of the FOV. On the other hand, in Fig. 4.13-(a), (b), (c), or in Fig. 4.14, the black shaded area appears outside of the interior border of the FOV. Figure 4.12-(a) and (b) do not have the black shaded area, which means the shaded area is entirely covered with the FOV. Figure 4.12-(c) and (d) show the similar feature to Fig. 4.14, although Figure 4.12-(d) also shows the same feature of Fig. 4.11.

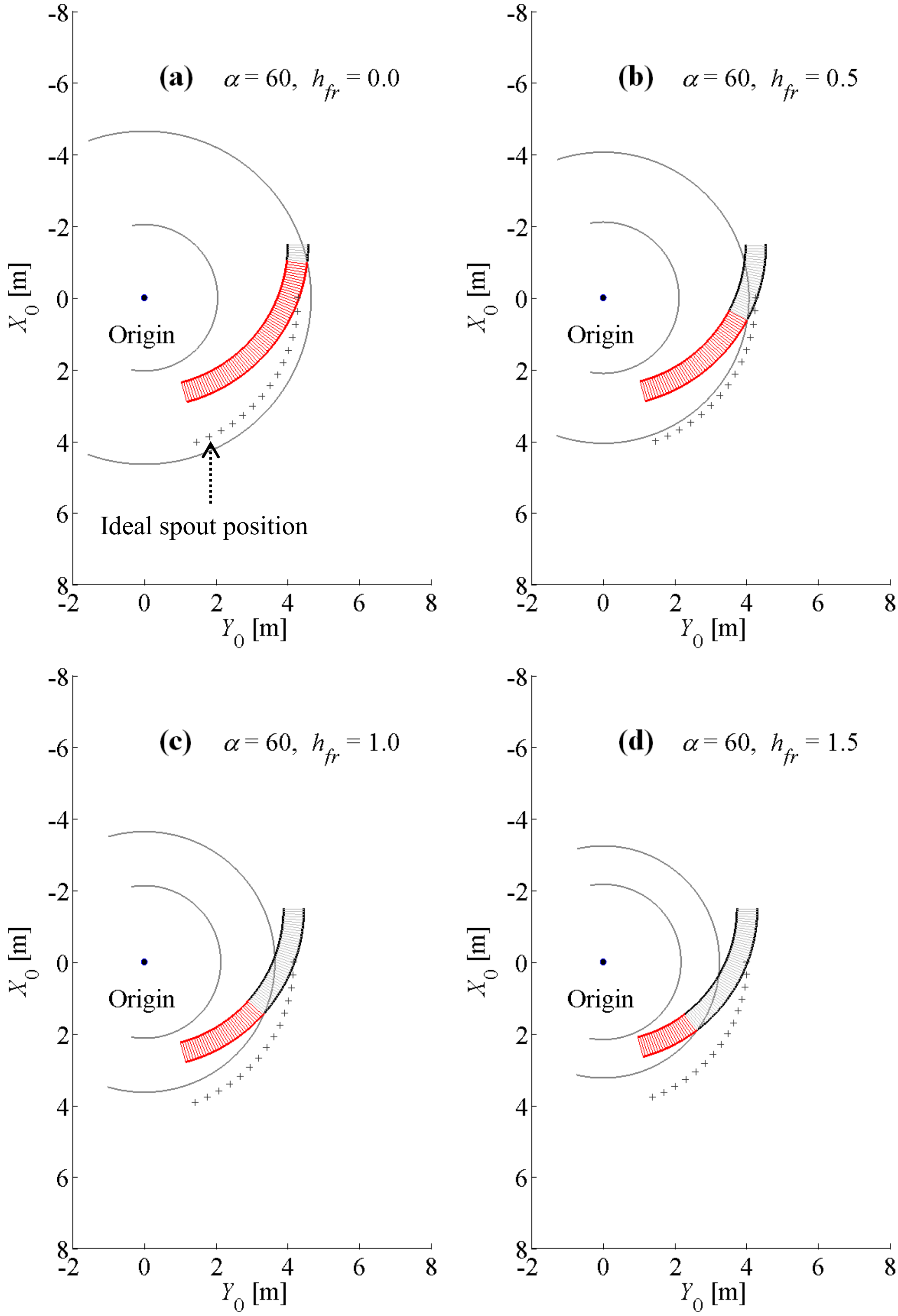

Fig. 4. 11. Fiducial marker coverage with maximal FOV when $\alpha = 60°$.
(a). h_{fr} = 0.0 m; (b). h_{fr} = 0.5 m; (c). h_{fr} = 1.0 m; h_{fr} = 1.5 m.

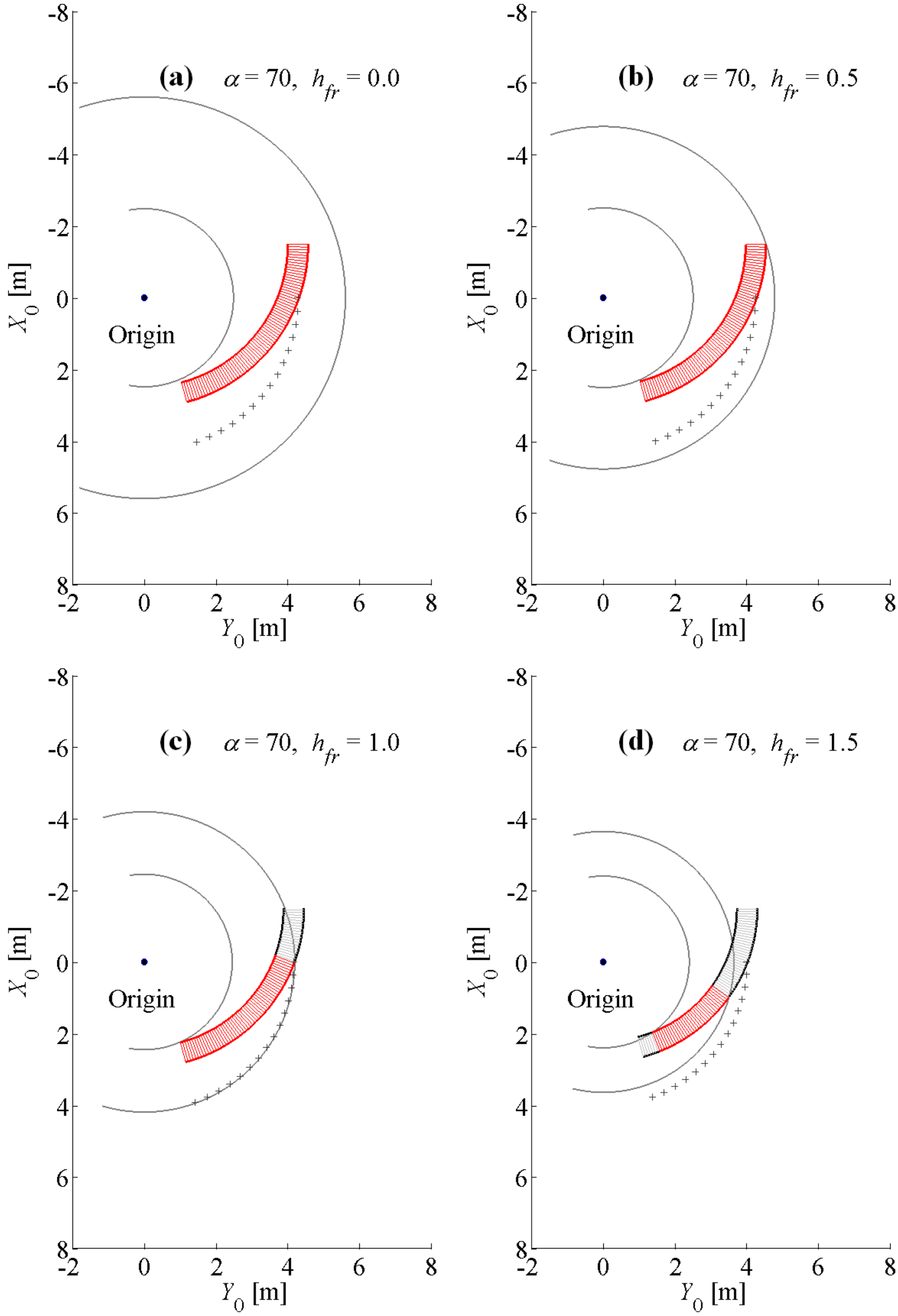

Fig. 4. 12. Fiducial marker coverage with maximal FOV when $\alpha = 70°$.
(a). $h_{fr} = 0.0$ m; (b). $h_{fr} = 0.5$ m; (c). $h_{fr} = 1.0$ m; $h_{fr} = 1.5$ m.

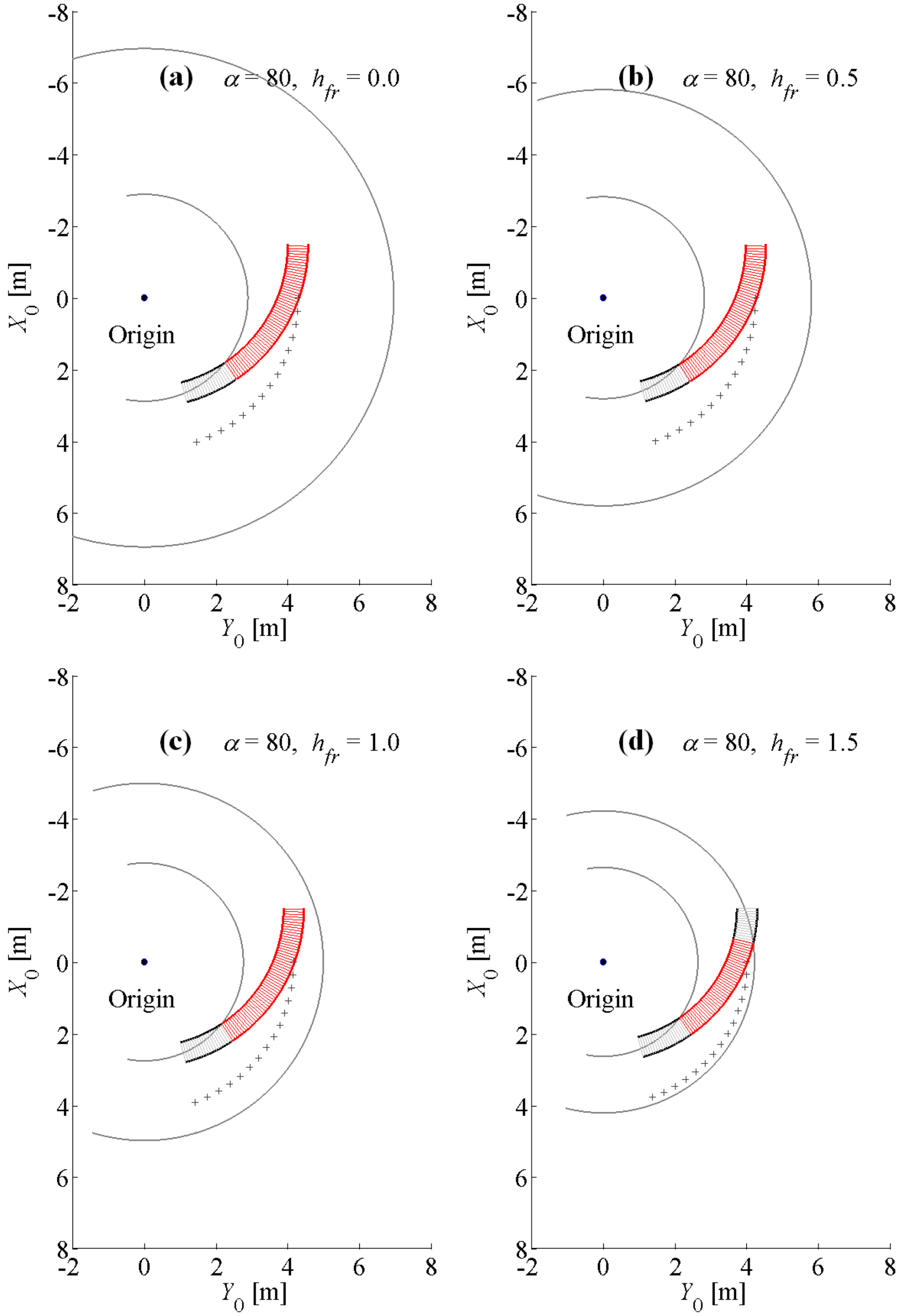

Fig. 4. 13. Fiducial marker coverage with maximal FOV when $\alpha = 80°$.
(a). h_{fr} = 0.0 m; (b). h_{fr} = 0.5 m; (c). h_{fr} = 1.0 m; h_{fr} = 1.5 m.

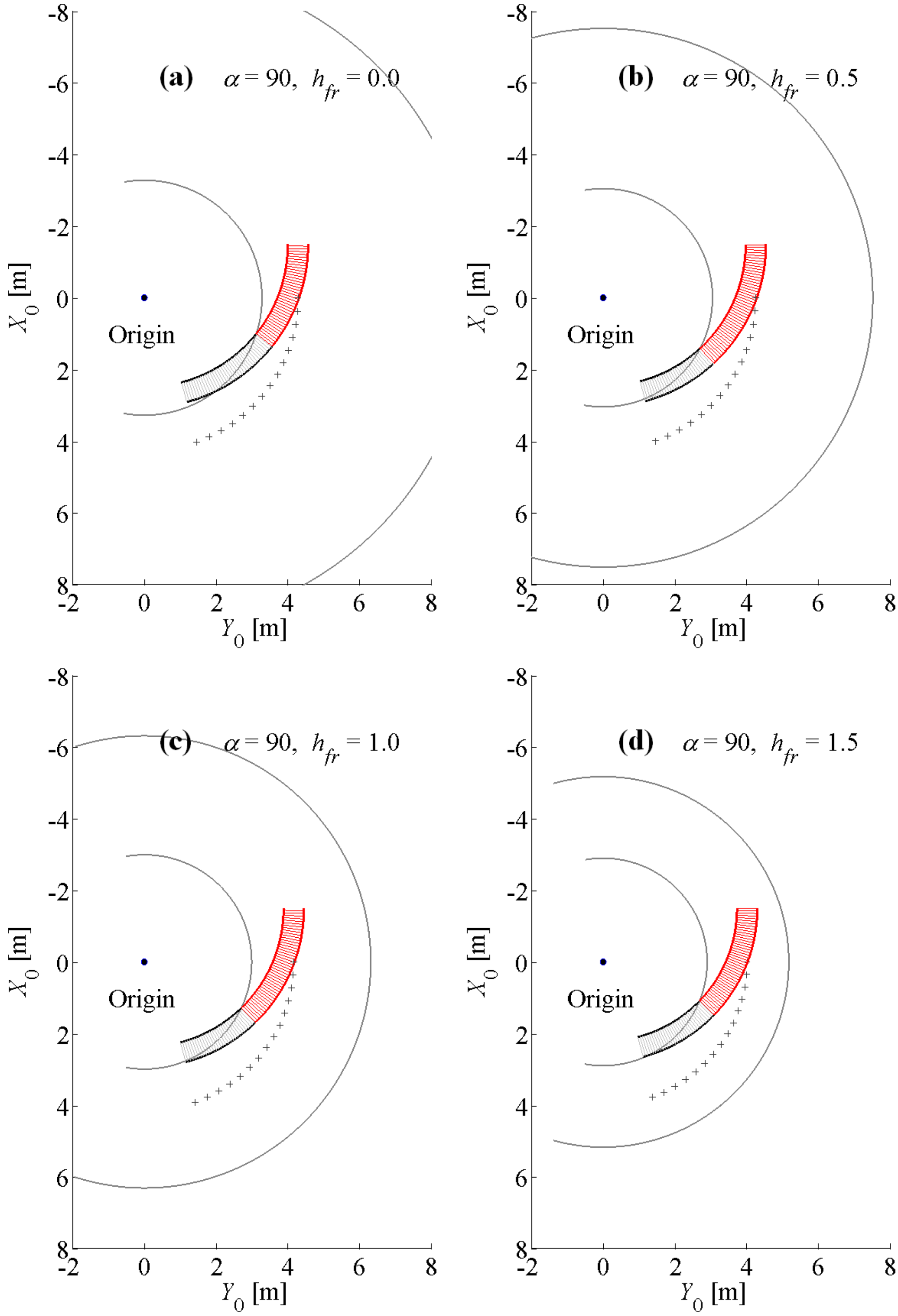

Fig. 4. 14. Fiducial marker coverage with maximal FOV when $\alpha = 90°$.
(a). h_{fr} = 0.0 m; (b). h_{fr} = 0.5 m; (c). h_{fr} = 1.0 m; h_{fr} = 1.5 m.

Figures shown in Table 4.5 also indicate these features.

Table 4.5. Ratio of each shaded area for representative α and h_{fr}.

α [°]	h_{fr} [m]	Outer black shaded area [%]	Inner black shaded area [%]	Red shaded area [%]	Average of red shaded area [%]
60	0.0	8.4	0.0	91.6	
	0.5	37.0	0.0	63.0	
	1.0	55.0	0.0	45.0	
	1.5	69.6	0.0	30.4	57.5
70	0.0	0.0	0.0	100.0	
	0.5	0.1	0.0	99.9	
	1.0	26.1	0.0	73.9	
	1.5	47.0	8.8	44.2	79.5
80	0.0	0.0	25.7	74.3	
	0.5	0.0	23.0	77.0	
	1.0	0.0	24.9	75.1	
	1.5	17.6	26.4	56.1	70.6
90	0.0	0.0	48.3	51.7	
	0.5	0.0	37.0	63.0	
	1.0	0.0	38.9	61.1	
	1.5	0.0	41.4	58.6	58.6

In Table 4.5, the outer black shaded area is the one that appears outside of the interior border of the maximal FOV, which is typically seen in Fig. 4.11, while the inner black shaded area appears outside of the exterior border of the maximal FOV as shown in Fig. 4.14. The shaded area that is included in the maximal FOV is denoted as the red shaded area. And the figures in this table represent the percentage of each shaded area in the total shaded area that represents, as described above, the area in which the fiducial marker is considered to exist corresponding to the ideal spout position. For each α value, the average value of four red shaded areas is shown in the rightmost column. The results for each α correspond to the each figure such as Fig. 4.11 to Fig. 4.14. For example, the uppermost column, the case of $\alpha = 60°$ and $h_{fr} = 0.0$ m, shows the data of Fig. 4.11-(a), which indicates that 91.6% of the shaded area is included in the maximal FOV and the rest of the area is outside of the exterior border of the FOV. And in the case of $\alpha = 60°$, the shaded area can be covered, on average, 57.5% with the maximal FOV.

As described above, Table 4.5 supports the qualitative consideration. First, the red shaded, overlapped area generally decreases as the h_{fr} increases, although in $\alpha = 80°$ and 90°, the case of $h_{fr} = 0.0$ m covers smaller area than that of $h_{fr} = 0.5$ m. Second, in the case of $\alpha =$ 60° and 70°, the inner black shaded area is almost 0.0%, while there is a certain amount of the outer black shaded area. In contrast, the inner black shaded area appears to some extent in the case of $\alpha = 80°$ and 90°, while the outer black shaded area is almost 0.0%. This indicates that the maximal FOV, as a whole, moves centrifugally relative to the shaded area according to increasing α.

From the results shown in Fig. 4.11 to Fig. 4.14 and in Table 4.5, the value of $\alpha = 60°$ is too small, that is the optical axis of the camera looks too inward (c.f. Fig. 4.4 or Fig. 4.6). Similarly the value of $\alpha = 90°$ is too large, that is the camera looks too outward. It is certain that the larger α gives the larger FOV and thereby that the case of $\alpha = 90°$ gives the largest FOV in the representative values of α, however, the camera results in searching wider area in vain when $\alpha = 90°$. As a result, the average value of fiducial marker coverage remains 58.6%, which is almost equivalent to the 57.5% when $\alpha = 60°$. The case of $\alpha = 70°$ or $\alpha = 80°$ gives some different results. In both cases, the average value of red shaded area is over 70% and the overlapped area is neither located too close to the interior nor the exterior border of the maximal FOV. Thus, concerning the values between $\alpha = 71°$ and 79° (every 1°), the ratio of each shaded area is computed and, in the same manner of Table 4.5, shown in Table 4.6.

Table 4.6. Ratio of each shaded area for representative h_{fr} and for α from 71° to 79°.

α [°]	h_{fr} [m]	Outer black shaded area [%]	Inner black shaded area [%]	Red shaded area [%]	Average of red shaded area [%]
71	0.0	0.0	0.0	100.0	
	0.5	0.0	0.0	100.0	
	1.0	22.6	2.3	75.1	
	1.5	44.5	10.9	44.6	79.9
72	0.0	0.0	0.0	100.0	
	0.5	0.0	3.6	96.4	
	1.0	19.2	5.7	75.1	
	1.5	41.9	12.8	45.3	79.2
73	0.0	0.0	3.3	96.7	
	0.5	0.0	6.3	93.7	
	1.0	15.6	8.8	75.6	
	1.5	39.3	14.6	46.1	78.0
74	0.0	0.0	7.5	92.5	
	0.5	0.0	9.1	90.9	
	1.0	11.9	11.6	76.6	
	1.5	36.5	16.4	47.1	76.8
75	0.0	0.0	11.1	88.9	
	0.5	0.0	11.7	88.3	
	1.0	7.9	14.2	77.9	
	1.5	33.7	18.1	48.2	75.8

α [°]	h_{fr} [m]	Outer black shaded area [%]	Inner black shaded area [%]	Red shaded area [%]	Average of red shaded area [%]
76	0.0	0.0	14.4	85.6	
	0.5	0.0	14.2	85.8	
	1.0	3.6	16.8	79.6	
	1.5	30.8	19.8	49.4	75.1
77	0.0	0.0	17.4	82.6	
	0.5	0.0	16.5	83.5	
	1.0	0.0	18.9	81.1	
	1.5	27.7	21.6	50.7	74.5
78	0.0	0.0	20.4	79.6	
	0.5	0.0	18.8	81.2	
	1.0	0.0	21.0	79.0	
	1.5	24.5	23.2	52.3	73.0
79	0.0	0.0	23.0	77.0	
	0.5	0.0	20.9	79.1	
	1.0	0.0	22.9	77.1	
	1.5	21.0	24.8	54.2	71.8

Table 4.6 indicates that the FOV at α = 71° gives the largest overlapped area on average. Therefore, the angle α is optimal to be 71°.

4.4. Auger Control for Searching Procedure

4.4.1. Strategy of Auger Control

Figure 4.15 shows the maximal FOV when α is 71°. In the figure, especially for the case of θ_1 = 0°, 90° and 180°, FOVs at θ_2 = 20°, 30°, 40° and 45° are also illustrated in trapezoidal shape, in a widening order from the smallest to the largest. In Fig. 4.15-(a) and (b), the maximal FOV consists of the FOV at θ_2 = 20° for the smallest and that at θ_2 = 45° for the largest. In Fig. 4.15-(c) and (d), the maximal FOV is generated only by the FOV at θ_2 = 45° for both the smallest and the largest, since the FOV at θ_2 = 45° includes all the FOVs at other θ_2 values. Then, if searching is performed at θ_2 = 20° and θ_2 = 45°, the camera searches the whole area that it can physically catch.

If the unloading auger rotates with θ_2 = 20°, however, physical interference possibly arises between the auger and the grain storage container (c.f. Fig. 4.2 or Fig. 4.3). Table 4.3 also suggests that it will occur especially in h_{fr} = 1.5 m, because the ideal θ_2 for unloading is estimated to be 20.5° when h_{fr} is 1.5 m. In the end, it seems to be preferable that the searching procedure is performed at θ_2 = 30° and θ_2 = 45°. Taking into account the fact that the maximal FOV can be almost entirely covered only with the FOV at θ_2 = 45°, the searching procedure should be performed primarily at θ_2 = 45° and after that, it should be performed at θ_2 = 30°. Hereinafter, let the former be *the primary searching step* and let the latter be *the secondary searching step*.

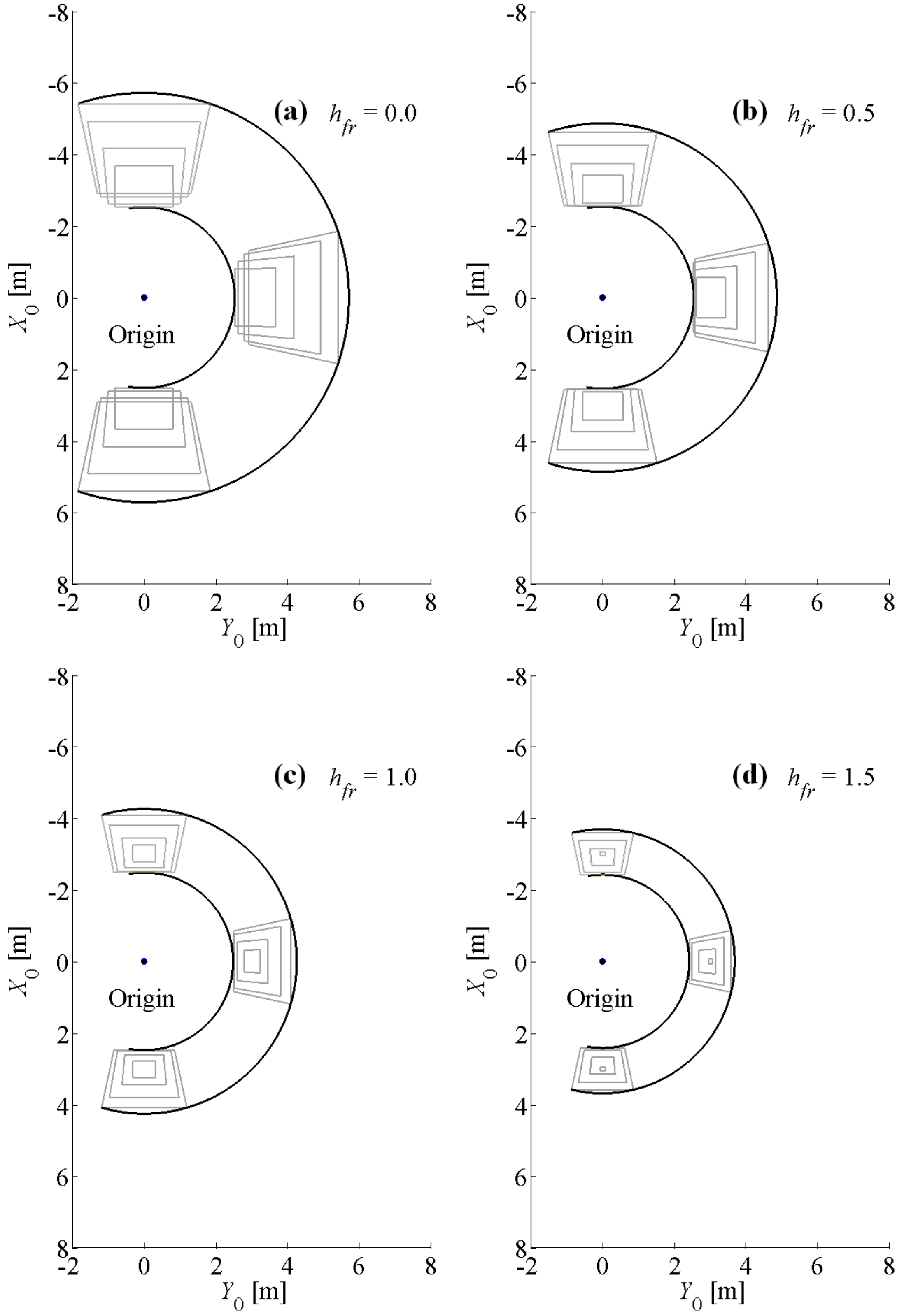

Fig. 4.15. Maximal FOV when α is 71°.

(a). h_{fr} = 0.0 m; (b). h_{fr} = 0.5 m; (c). h_{fr} = 1.0 m; h_{fr} = 1.5 m.

In this study, a software program is developed for controlling the unloading auger based on the target position obtained through image processing. The combine harvester is controlled by several ECUs. The program runs on a laptop PC and communicates with the combine via a RS-232C cable. It simultaneously performs the image processing in which images are taken from the USB camera and the desired joint angles are calculated if the fiducial marker is detected. The angles are sent to the ECU together with other commands (see Fig. 2.6).

Figure 4.16 shows the algorithm of the software program. The right column is the main flow of the algorithm, in which a series of data is received and sent in period of 100 ms. And in the searching mode, searching procedure is performed until the fiducial marker is detected. When the image processing program recognizes that the fiducial marker is detected, the searching procedure is terminated and the auger stops moving for a few seconds to obtain clearer images, and thereby to enable more precise computation of the joint angles. The joint angles are obtained based on the method presented in Chapter 3. After a predefined period of stopping, the calculated joint angles are defined as the target angles in the positioning mode. The left column shows the flow of image processing. It is multi-threaded and is repeated independently of the main flow.

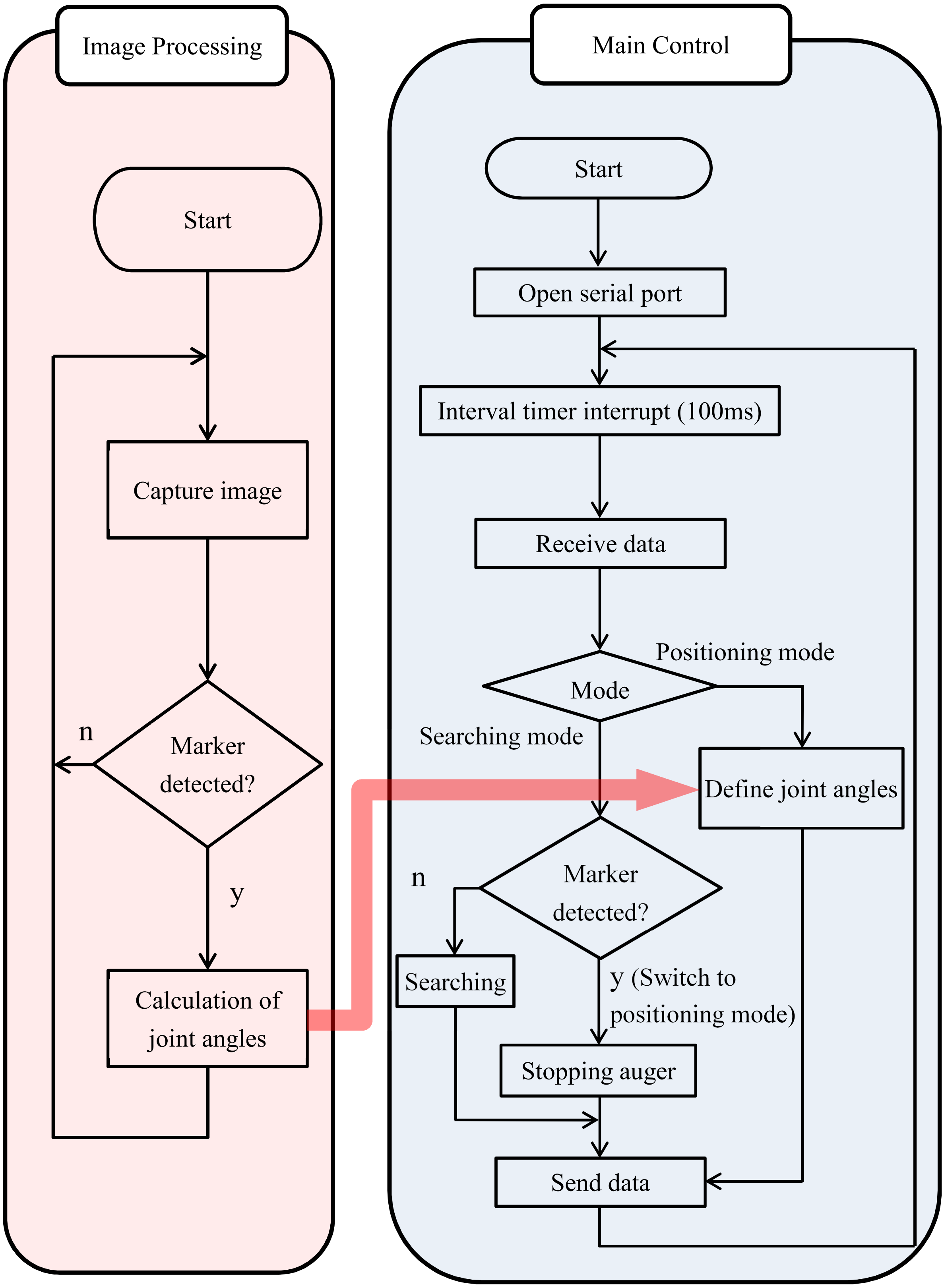

Fig. 4.16. Algorithm.

4.4.2. Assumptions and Experimental Procedure

To confirm the efficiency and the validity of the presented method, a searching experiment was conducted. In the experiment, a simple situation is assumed, but it seems sufficiently reasonable because it is highly possible in the actual unloading operation. Assumptions are as follows:

1. The combine harvester is parked in a paddy field almost alongside a pickup truck that is located on the farm road alongside the paddy, as shown in Fig. 4.1.

2. The fiducial marker is attached to the roof of the truck.

3. The auger spout can be physically positioned to the given target point, which is preliminarily assigned in the software program.

About the assignment of the target point, the details have already been explained in Section 3.4 and will not be addressed here. The experiment was conducted in the following manner: Two joints of the unloading auger were initialized at θ_1 = 192° and θ_2 = 3°, respectively. Let this state be *the default position*. The auger starts to move from the default position. After the fiducial marker has been detected, the spout positioning was performed (c.f. Fig. 4.16).

Among tests, the positional relation between the combine and the fiducial marker were slightly changed. Through the fiducial marker searching and spout positioning task, two joint angles, θ_1 and θ_2, were recorded every 0.1 s. The required time for the searching and positioning operation was measured to confirm the efficiency. Whether the combine robot can detect the fiducial marker with the method and whether the presented searching steps are sufficient were confirmed to validate the proposed method.

4.5. Results and Discussion

Following figures illustrate the trajectory of the auger spout and the transition of auger joint angles (θ_1 and θ_2). Note that for these figures, each trajectory is three-dimensionally rotated to facilitate perceiving the whole trajectory. Thus, although the graphs sometimes vary in appearance, this is just caused by different viewpoints.

a) Case 1

Figure 4.17 shows an experimental result when the fiducial marker is detected during the primary searching step. The grey dot line shows the locus of the auger spout during the searching process, while the red circle indicates the positioning process. The red rectangle represents the estimated position of the fiducial marker. As illustrated in Fig. 4.17-(a), the primary step starts its path from the default position (i.e., θ_1 = 192° and θ_2 = 3°, and marked as N_1 in the figure). The unloading auger raises its joint angle θ_2 up to 45° (marked as N_2) and then rotates clockwise until reaching to the next node (N_3, but not shown). During this rotation, the fiducial marker is detected at a spout position S_1 (θ_1 = 37.5° and θ_2 = 45°). After the calculation of the target joint angles, the unloading auger is positioned to that position. In the positioning, the auger rotates counter clockwise from S_1, via S_2 (θ_1 = 44.6° and θ_2 = 45°), to S_3 (θ_1 = 44.6° and θ_2 = 29.8°). In Fig. 4.17-(b), the transition of the joint angles is plotted against time elapsed, the grey continuous line for θ_1 and the black dashed line for θ_2. In this instance, it takes 7.6 seconds until detecting the fiducial marker. After a 2.2 second lapse, positioning commenced and took 2.0 seconds. As a whole, 12 seconds were needed for searching and positioning. An additional two tests were conducted and the entire searching and positioning procedure required 18 seconds and 17 seconds, respectively.

a) Case 2

Next, an experimental result is presented on the case when the camera finds the fiducial marker not on the first searching step but on the second searching step. Figure 4.18-(a) shows a trajectory typical for this case. From the end of the primary searching step (N_3: θ_1 = 0° and θ_2 = 45°), the unloading auger lowers its joint angle θ_2 down to 30° (marked as N_4) and then it rotates counter clockwise to the point of θ_1 = 90°. The fiducial marker is detected at a spout position S_4 (θ_1 = 54° and θ_2 = 30°). After a few seconds, the auger is positioned to the position θ_1 = 27° and θ_2 = 0° (marked as S_5). These characteristic nodes are also noted in Fig. 4.18-(b). It takes 9.6 seconds for the primary searching step and 4.6 seconds from the end of the primary step to the detection of the fiducial marker. The positioning step took 3.6 seconds in this case. As a whole, it took about 23 seconds until positioning has finished. In the other two tests, it took 22 seconds and 16 seconds, respectively, for the searching and positioning procedure.

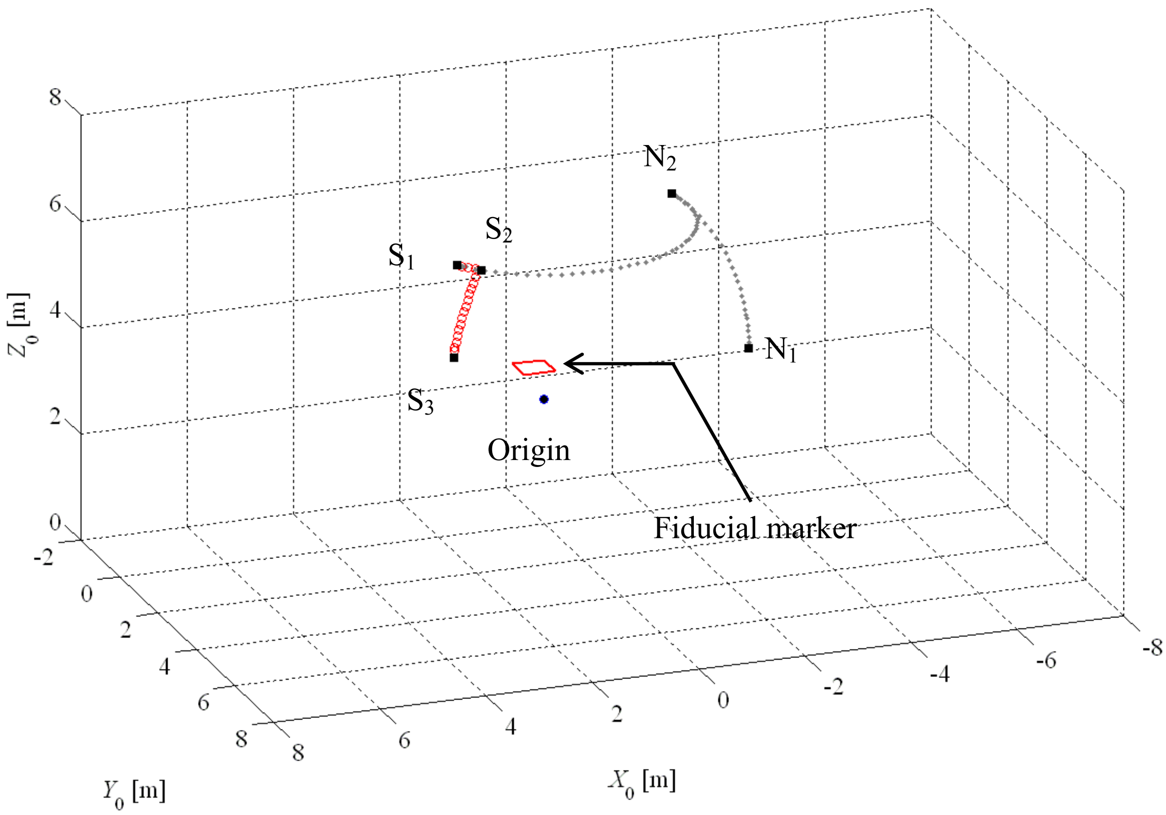

Fig. 4.17-(a). Trajectory of auger spout.

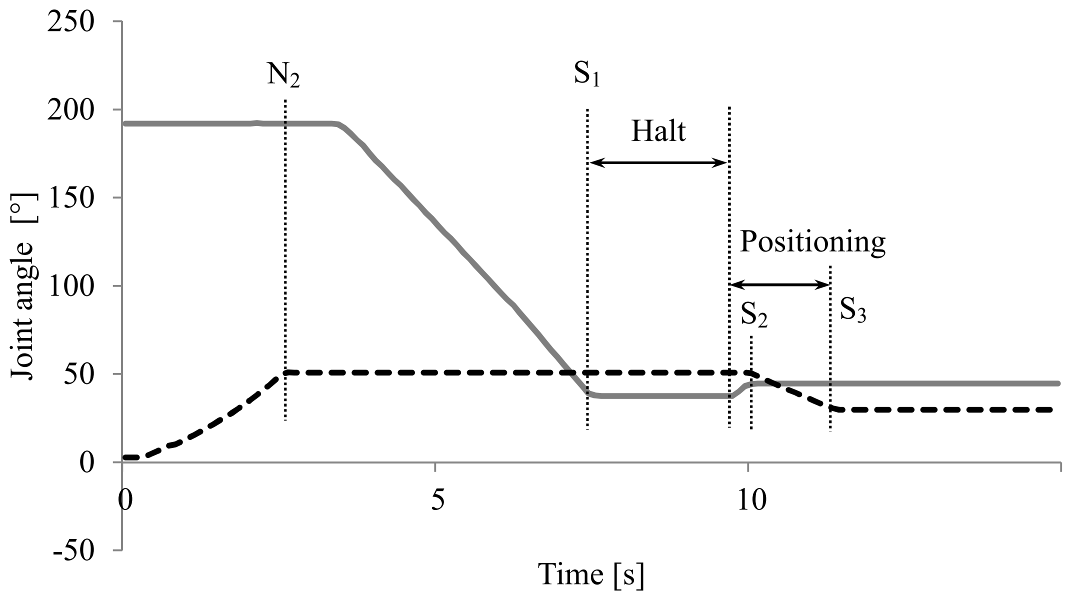

Fig. 4.17-(b). Transition of joint angles.

—— : θ_1; - - - - : θ_2

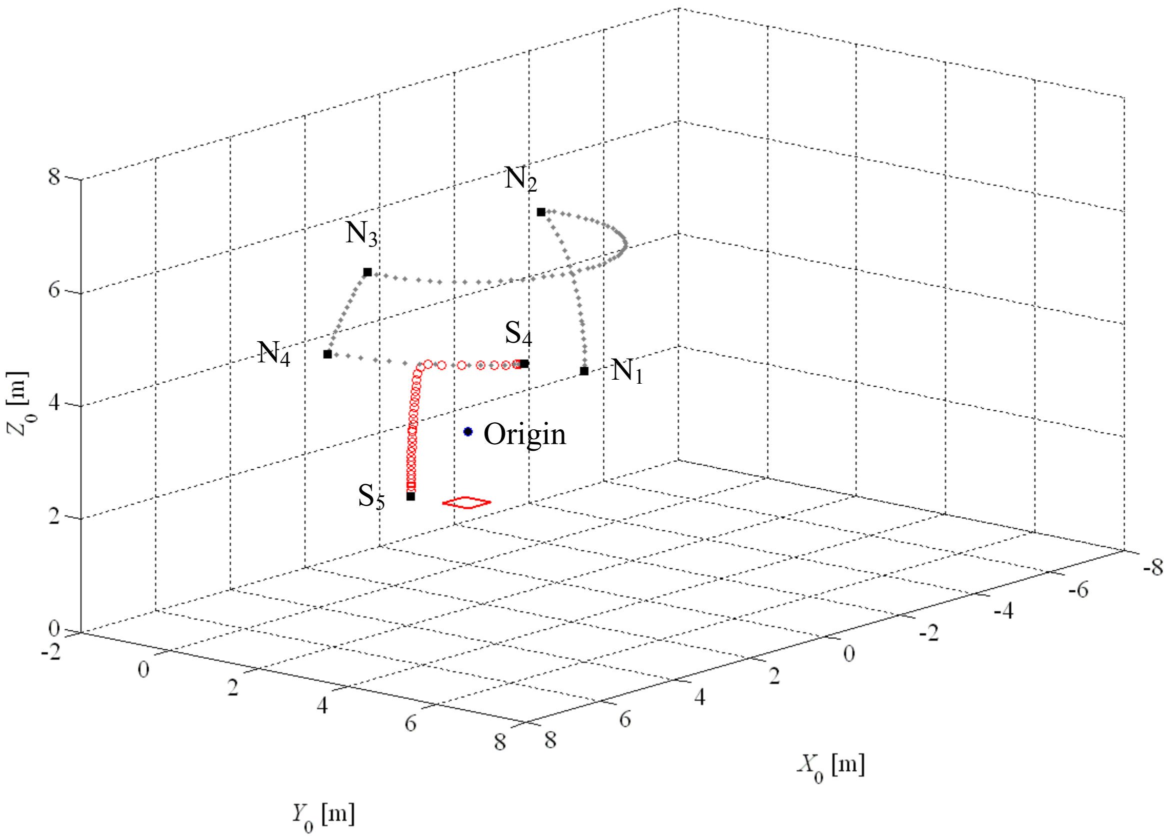

Fig. 4.18-(a). Trajectory of auger spout.

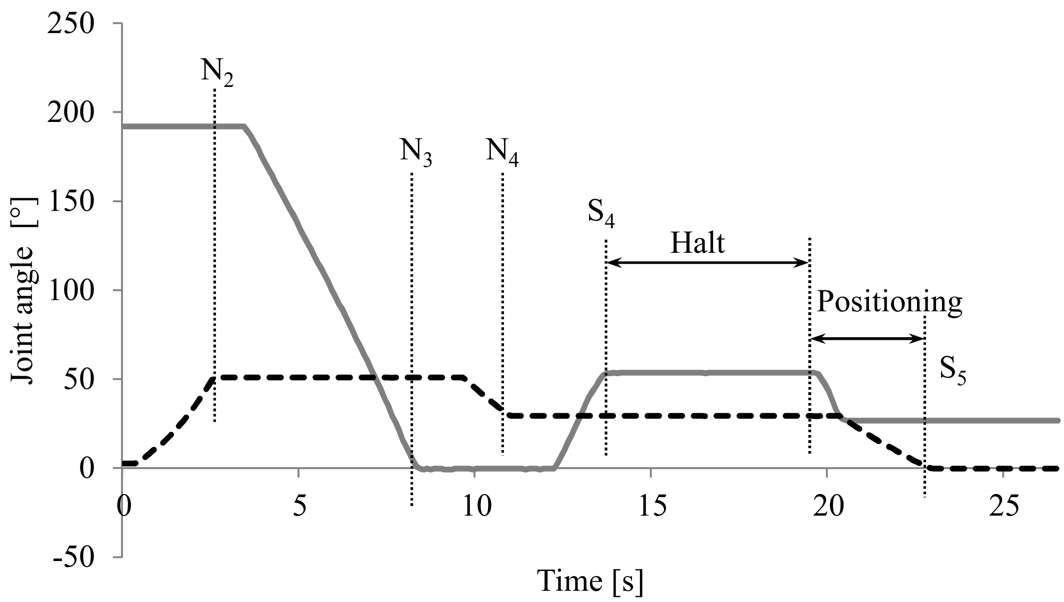

Fig. 4.18-(b). Transition of joint angles.

: θ_1; : θ_2

When an operator of the combine manually positions the unloading auger to the appropriate point above the grain storage container, it took about 37 seconds on average, which is the time taken for actual unloading operation performed by not only skilled but also by unskilled operators. Table 4.7 summarizes the required time for spout positioning for both unmanned and manned operation.

Although it is difficult to make a precise comparison of the measured time with manual positioning and the elapsed time that is required for the presented autonomous method, since the former was performed in a quite different manner from the latter, and the manner itself depends on each operator, however, it is clear that the autonomous searching and positioning method is not much more time-consuming than manual positioning.

Figure 4.18 shows the result when the fiducial marker is detected in the secondary searching step. In this case, the combine and the fiducial marker are located in such a way that the fiducial marker is not included in the FOV at θ_2 = 45° (i.e., the height of the primary searching step), and at the same time, included in the FOV at θ_2 = 30° (i.e., the height of the secondary searching step). This, however, happened in only a few tests. In fact, the fiducial marker was almost always detected in the primary step. Thus, the autonomous method will seldom require more than 20 seconds. The secondary searching step serves as an auxiliary searching procedure and it does not happen frequently. Nevertheless, the secondary searching step is useful. Usually, it takes just an additional few seconds, and thereby the auger camera can cover most of the maximal FOV.

Table 4.7. Required time for positioning operation.

	Test	Required time [s]
Case 1	1	12
	2	18
	3	17
Case 2	1	23
	2	22
	3	16
Manual operation		37 (on average)

4.6. Conclusions

For the installation of the auger camera, including fiducial marker searching, the FOV of the auger camera was computed based on the variables that affect the FOV, the camera's elevation angle α, the height of farm road h_{fr}, and the joint angle θ_2. The assumption is that the fiducial marker is searched by the camera attached to the unloading auger. The most suitable angle α was determined for the most effective fiducial marker search. An efficient searching procedure was proposed based on the simulation results.

For each representative value of α and h_{fr}, the maximal FOV was obtained which indicates the whole area the auger camera can mechanically incorporate when θ_2 varies from 20° to 45°. When the auger spout of the unloading auger is successfully positioned to the assigned target point, then the ideal joint angle θ_2 is bound by the height of the farm road h_{fr}. With respect to the ideal θ_2, the area in which the fiducial marker should exist can be simultaneously estimated. Then, α was determined such that the maximal FOV can cover this area, as much as possible. The angle of α = 71° provided, on average, the largest fiducial marker coverage 79.9%.

After the assignment of this α value, maximal FOVs at representative θ_2 values were computed as shown in Fig. 4.15. This suggests that the maximal FOV can be covered by searching at θ_2 = 45° (the primary searching step) and the rest of the maximal FOV is almost covered by that at θ_2 = 30° (the secondary searching step). The experimental results also show that the fiducial marker was detected mainly in the primary searching step. The secondary searching step is still useful for achieving maximal FOV. The fiducial marker was certainly detected, if it is located inside the maximal FOV, either during the primary searching step or the secondary searching step, and additional searching steps are needless.

When the fiducial marker was detected in the primary searching step, it took 16 seconds for searching and positioning. It took 20 seconds for the whole process when the fiducial marker was acquired in the secondary step. This figure is comparable to the time needed in manual positioning.

Therefore, the presented method, the combine robot performs the searching, detecting and positioning task with high efficiency and sufficient reliability.

REFERENCES

[1] Kurita, H., Iida, M., Suguri, M. and Masuda, R: Application of Image Processing Technology for Unloading Automation of Robotic Head-Feeding Combine Harvester. Engineering in Agriculture, Environment and Food, vol. 5, no. 4, 146-151, 2012.

[2] Buckmaster, D. R. and Hilton, J. W: Computerized cycle analysis of harvest, transport, and unload systems. Computer and Electronics in Agriculture, vol. 47, 137-147, 2005.

[3] Salaris, P., Pallottino, L., Hutchinson, S. and Bicchi, A: From Optimal Planning to Visual Servoing with Limited FOV. *Proceedings* of the 2011 IEEE/RSJ International Conference on Intelligent Robots and Systems, 2817-2824, CA, USA, 2011.

[4] Zhang, H. and Ostrowski, J. P: Visual Motion Planning for Mobile Robots. IEEE Transactions on Robotics and Automation, vol. 18, no. 2, 199-208, 2002.

[5] Tsotsos, J. K. and Shubina, K: Attention and Visual Search: Active Robotic Vision Systems that Search. Keynote Lecture of the 5th International Conference on Computer Vision Systems, Bielefeld, Germany, 2007.

[6] Osais, Y. E., St-Hilaire, M. and Yu, F. R: Directional Sensor Placement with Optimal Sensing Range, Field of View and Orientation. Mobile Networks and Applications, vol. 15, issue 2, 216-225, 2010.

[7] Li, J. Wang, R. Huang, H. and Sun, L: Voronoi-Based Coverage Optimization for Directional Sensor Networks. Wireless Sensor Network, vol. 1, no. 5, 417-424, 2009.

[8] Murray, A. T., Kim, K., Davis, J. W., Machiraju, R. and Parent, R: Coverage Optimization to Support Security Monitoring. Computers, Environment and Urban Systems, vol. 31, 133-147, 2007.

[9] Erdem, U. M. and Sclaroff, S: Automated Camera Layout to Satisfy Task-Specific and Floorplan-Specific Coverage Requirements. Computer Vision and Image Understanding, vol. 103, 156-169, 2006.

[10] Debaque, B., Jedidi, R. and Prevost, D: Optimal Video Camera Network Deployment to Support Security Monitoring. *Proceedings* of the 12th International Conference on Information Fusion, WA, USA, 1730-1736, 2009.

[11] Denavit, J. and Hartenberg, R. S: A Kinematic Notation for Lower-Pair Mechanisms Based on Matrices. ASME Journal of Applied Mechanics, vol. 77, 215-221, 1955.

[12] Asada, H. and Slotine, J. –J. E: Robot Analysis and Control. Wiley-Interscience Publication, NY, USA, 15-50, 1986.

[13] Paul, R. P: Robot Manipulators. MIT Press, Cambridge, England, 41-81, 1981.

[14] Yoshikawa, T: Foundations of Robot Control. Corona Publishing Co., Ltd., Tokyo, Japan, 11-68, 1988.

[15] Munishwar, V. P., Tilak, S. and Abu-Ghazaleh, N. B: Coverage Management for Mobile Targets in Visual Sensor Networks. *Proceedings* of the 15th ACM International Conference on modeling, Analysis and Simulation of Wireless and Mobile Systems, 107-116, NY, USA, 2012.

[16] Gonzalez, R. C., Wintz, P. Digital Image Processing 2nd Edition. Addison-Wesley Publishing Company, MA, USA, 1987.

[17] Xu, G., Zhang, Z. Epipolar Geometry in Stereo, Motion and Object Recognition: A Unified Approach. Kluwer Academic Publishers Norwell, MA, USA, 1996.

CHAPTER 5

AUTONOMOUS UNLOADING SYSTEM FOR ACTUAL UNLOADING OPERATION

5.1. Introduction

For decades, vehicular robots have been eagerly studied and developed in various fields. Recently, RTK-GPS has been widely used for autonomous navigation. Also in the field of agricultural engineering, researchers have tried to develop autonomously guided machinery using GPS navigation [1]-[3]. The RTK-GPS has an accuracy of within 20 mm. It is utilized as a navigation sensor for the combine harvester robot, which has demonstrated to sufficiently control path following performance and has successfully harvested crops in actual harvesting experiments [4], [5]. This high accuracy could be applied for auger spout positioning.

After harvesting, the combine is required to unload grain into some kind of vehicle for offsite transportation. Usually, a lightweight type of pickup truck is used as the transportation means, especially in the main island of Japan. A grain storage container is, generally, mounted on the truck. Under these assumptions, a machine vision based-method is presented to determine the joint angles for positioning the auger spout of the unloading auger to a target point to unload grain [6]. This method provides the basis for autonomous unloading. In the method, a planar fiducial marker is utilized to help locate a grain storage container, using input images captured by a USB camera, and to estimate the positional relation between the combine harvester and the grain storage container.

The fiducial marker needs to be detected by the camera. In order to search and detect it efficiently and certainly, the camera's FOV is computed. Based on the analysis on FOV, the camera was appropriately installed on the combine robot and an efficient and absolute fiducial marker searching procedure is presented [7], [8].

Although the presented methods result in positioning with sufficient accuracy and efficiency, the methods themselves assume simple conditions applied in actual unloading operations.

The objectives of this chapter are as follows:

1. To present the vision-based method by which the auger spout of the unloading auger can be positioned to an arbitrary target point with 3D accuracy.

2. To integrate the developed techniques, the combine control, the fiducial marker searching and the vision-based spout positioning, into the autonomous unloading system that is applicable in actual paddy field conditions.

3. To examine the performance of the presented autonomous unloading system in field tests.

5.2. Autonomous Unloading System

In this section, first, the basic method [6] is summarized and the problems involved are addressed. To solve these problems, the basic method is modified for more accurate spout positioning [9]. And then, a comprehensive method is presented for a more practical unloading operation, which includes the searching procedure, the modified method and returning of the combine`s auger to the unloading position.

5.2.1. 3D Positioning of Auger Spout

In the basic method, the unloading auger is modeled as a 2-DOF manipulator. Figure 5.1 shows the link structure of the unloading auger. Figure 5.2 is a schematic view of the coordinates in the basic method.

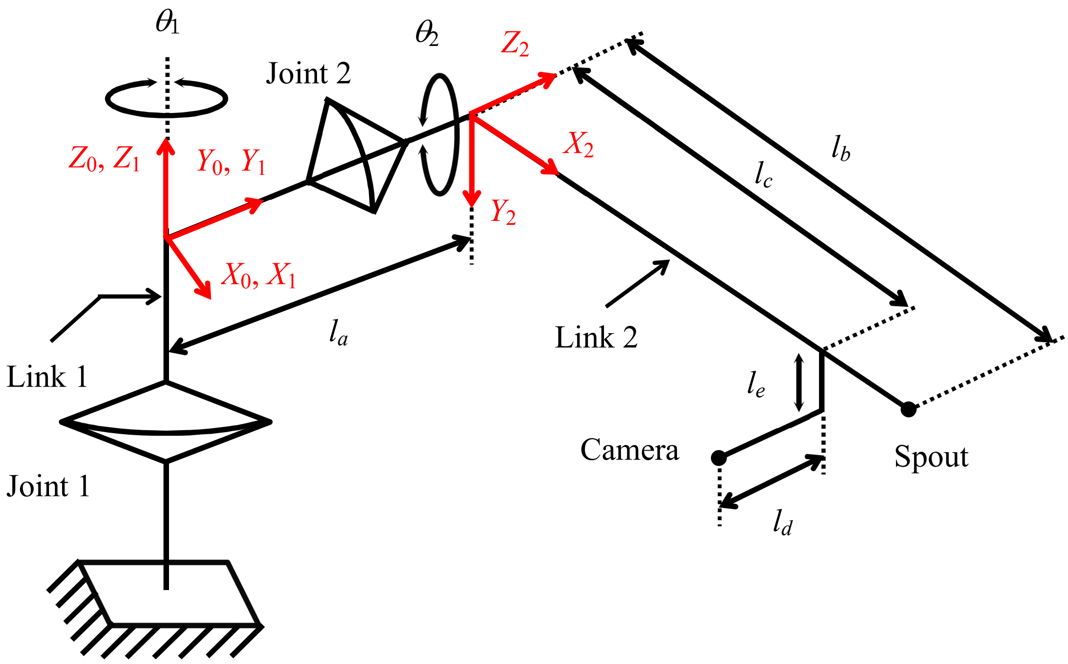

Fig. 5.1. Link structure of unloading auger.

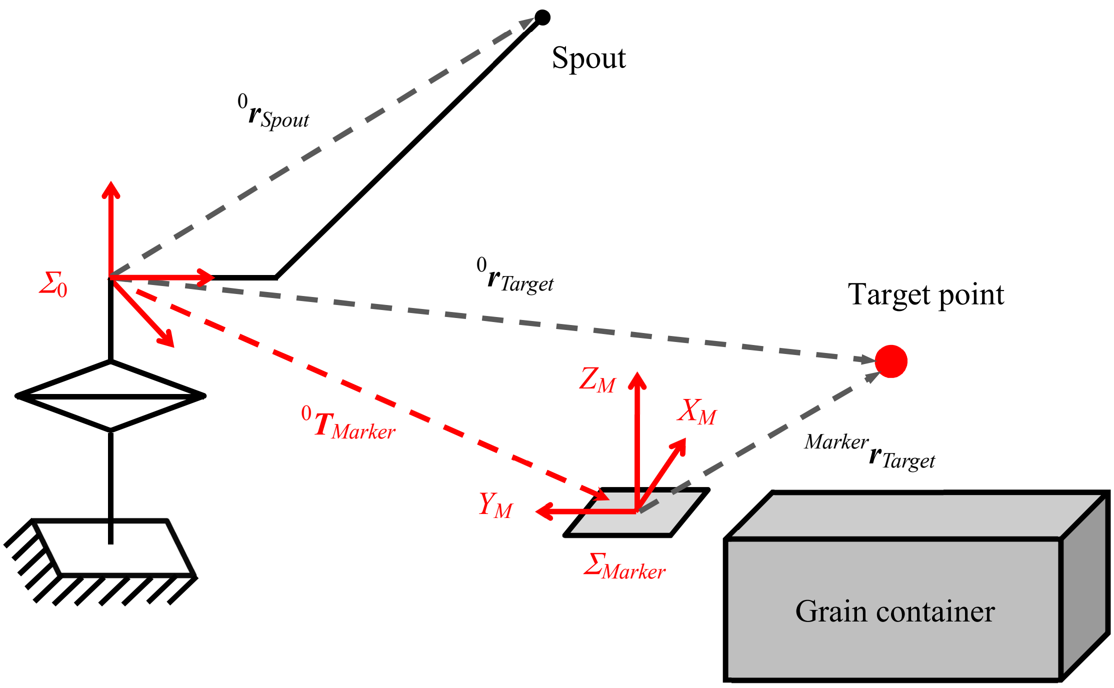

Fig. 5.2. Schematic view of basic method.

With the homogeneous transformation matrices ${}^{0}\boldsymbol{T}_1$ (from Σ_0 to Σ_1) and ${}^{1}\boldsymbol{T}_2$ (from Σ_1 to Σ_2), the position vector of the auger spout at Σ_0 is represented in Eq. (5.1).

$$\begin{aligned} {}^{0}\boldsymbol{r}_{Spout} &= {}^{0}\boldsymbol{T}_1\,{}^{1}\boldsymbol{T}_2\,{}^{2}\boldsymbol{r}_{Spout} \\ &= \begin{bmatrix} l_b\cos\theta_1\cos\theta_2 - l_a\sin\theta_1 \\ l_b\sin\theta_1\cos\theta_2 + l_a\cos\theta_1 \\ l_b\sin\theta_2 \\ 1 \end{bmatrix}. \end{aligned} \tag{5.1}$$

Now, assume that the fiducial marker has already been observed by the camera. Then ${}^{0}\boldsymbol{T}_1$ and ${}^{1}\boldsymbol{T}_2$ are determined by the joint angles θ_1 and θ_2 corresponding to the present auger's position. ${}^{2}\boldsymbol{T}_{Camera}$ is calculated based on the camera's elevation angle α and ${}^{Camera}\boldsymbol{T}_{Marker}$ is estimated according to the image processing technique [10], [11]. Thus, the position vector of the target point can be calculated as follows:

$$\begin{aligned} {}^{0}\boldsymbol{r}_{Target} &= {}^{0}\boldsymbol{T}_{Marker}\,{}^{Marker}\boldsymbol{r}_{Target} \\ &= {}^{0}\boldsymbol{T}_1\,{}^{1}\boldsymbol{T}_2\,{}^{2}\boldsymbol{T}_{Camera}\,{}^{Camera}\boldsymbol{T}_{Marker}\,{}^{Marker}\boldsymbol{r}_{Target} \\ &:= [x_0,\quad y_0,\quad z_0,\quad 1]^T, \end{aligned} \tag{5.2}$$

where, ${}^{Marker}\boldsymbol{r}_{Target}$ is properly assigned beforehand. If the spout overlaps the target point, ${}^{0}\boldsymbol{r}_{Spout}$ and ${}^{0}\boldsymbol{r}_{Target}$ satisfy the following relation.

$${}^{0}\boldsymbol{r}_{Spout} = {}^{0}\boldsymbol{r}_{Target}. \tag{5.3}$$

Finally, by solving Eq. (5.3) about x and y coordinates, the target joint angles are determined. With the angles expressed in Eq. (5.4) and Eq. (5.5), the spout can be positioned at the target point in horizontally [12]-[14].

$$\theta_1 = \tan^{-1}\frac{x_0}{y_0} - \sin^{-1}\left(\frac{l_a}{\sqrt{{x_0}^2 + {y_0}^2}}\right). \tag{5.4}$$

$$\theta_2 = \cos^{-1}\left(\frac{\sqrt{{x_0}^2 + {y_0}^2 - {l_a}^2}}{l_b}\right). \tag{5.5}$$

When the positioning to the position θ_1 and θ_2 is accurately completed, ${}^0\boldsymbol{r}_{Spout}$ should be equal to $[x_0,\ \ y_0,\ \ l_b \sin\theta_2\,,\ \ 1]^T$, however, $l_b \sin\theta_2 = z_0$ in general. Since the unloading auger used in this study has 2-DOF, it cannot satisfy Eq. (5.3) simultaneously in the x, y and z coordinates.

In the basic method, a simple condition is assumed that the harvester is located at the point where the unloading auger can be ideally positioned. In this ideal state, the positional relation between the combine and the grain storage container is as follows; when positioning is performed based on the calculated joint angles, the position vector of the auger spout is x_0 and y_0, almost exact in the x and y direction, respectively. In the z direction the spout position could be either higher or lower than z_0. In other words, if the positional relation is not ideal, the auger spout could be positioned at too high or too low a point from the target point.

The position of the combine harvester relative to the grain container (or pickup truck) is not always ideal. And in actual paddy fields, positioning accuracy is sometimes reduced by various factors such as soil condition, stack of chopped straws, wind condition and so on. Thus, it is essential for practical applications to develop a method that takes into account accuracy in z direction.

Because of the constraint in the DOF, the positioning method must put less priority to one of the three axes. Considering the fact that grain stream is almost vertically downward, the acceptable error range in the horizontal direction is relatively restricted, while the error in the vertical direction is more tolerable than that in the horizontal direction. The positioning accuracy in the horizontal direction is ensured by the basic method. Thus, it is reasonable to estimate and correct the vertical error at first, and then position the spout according to the basic method. To correct the vertical error, the harvester can travel forward just a required distance. In short, this forward traveling complements the lack of DOF of the unloading auger.

Suppose that the fiducial marker has already been detected and the joint angles θ_1 and θ_2 are calculated as described in Eq. (5.4) and Eq. (5.5). When the harvester now travels just ΔL forward, then the spout can be ideally positioned also in the vertical direction. In addition, it is presumed that the harvester's orientation remains static during the forward traveling. Then, the harvester-based coordinate system, Σ_0 is translated just $-\Delta L$ along X_0 axis into Σ_0'. The position vector of the target point on Σ_0' is thereby represented in Eq. (5.6).

$$^{0\prime}\boldsymbol{r}_{Target} = [x_0 + \Delta L, \quad y_0, \quad z_0, \quad 1]^T. \tag{5.6}$$

Before traveling, the target joint angles θ_1 and θ_2 are calculated. After forward traveling, they will be adjusted to the angles with which the spout again reaches the target point. Let them be $\tilde{\theta}_1$ and $\tilde{\theta}_2$. Figure 5.3 and Fig. 5.4 illustrate the schematic views of the positional relation before and after forward traveling.

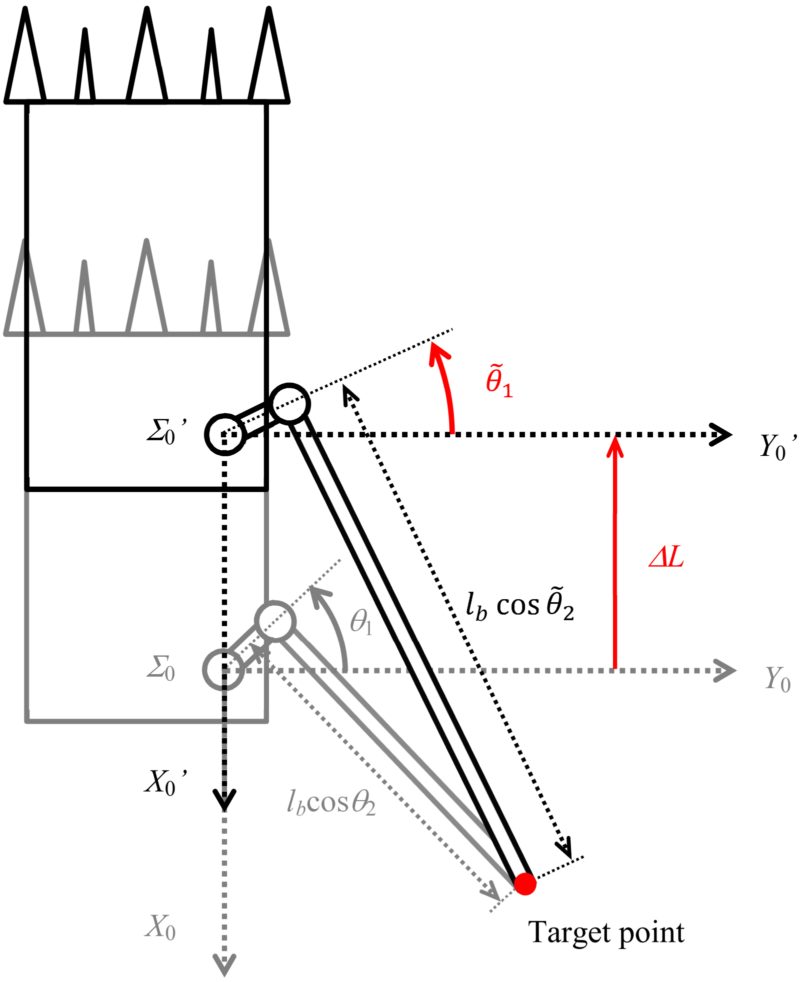

Fig. 5.3. Combine robot before and after forward traveling (top view).
(grey line) : before; (black line) : after

Figure 5.3 shows the view from above the combine before and after traveling. The combine before traveling and its annotation are shown in grey, while those after traveling are presented in black, although important parts are red colored. In both cases, the auger spout is positioned at the target point horizontally.

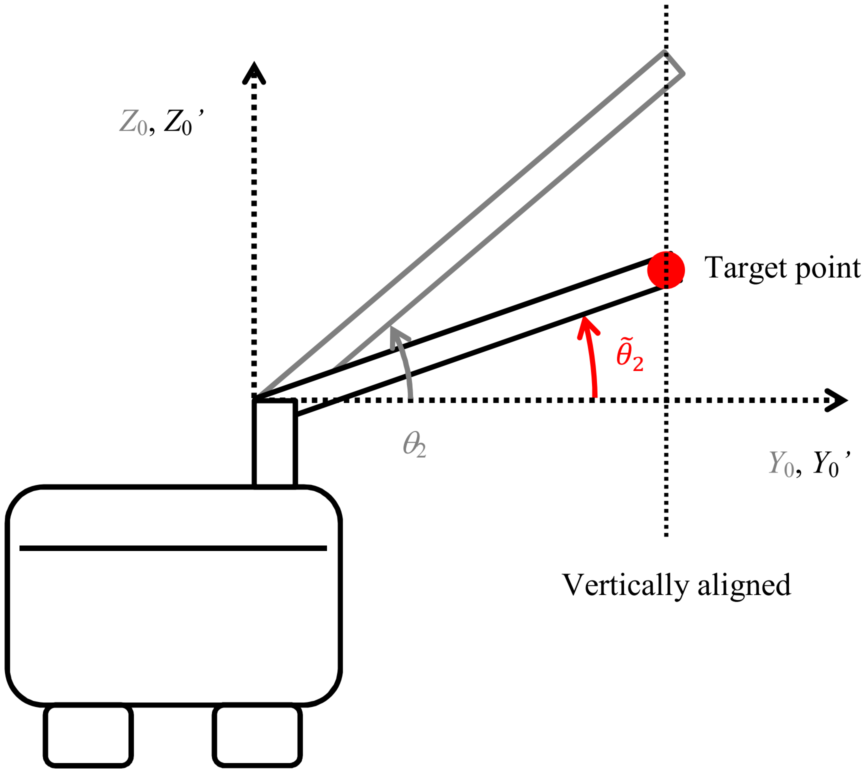

Fig. 5.4. Combine robot before and after forward traveling (rear view).
: before; : after

Figure 5.4 represents the cross-sectional view in the Y_0-Z_0 plane. The drawing and caption are similarly colored as in Fig. 5.3. In the state before and after traveling, the spout is aligned with the target point along the vertical direction.

${}^{0'}\boldsymbol{r}_{Spout}$, the position vector of the spout on Σ_0', is similarly obtained as Eq. (5.1). $\tilde{\theta}_1$ and $\tilde{\theta}_2$ will be determined by the basic method such that they satisfy Eq. (5.3) about the x and y coordinates. In addition, it is assumed that they satisfy the z coordinate due to the forward traveling by ΔL. Finally, ${}^{0'}\boldsymbol{r}_{Spout} = {}^{0'}\boldsymbol{r}_{Target}$ gives the following equations.

$$x_0 + \Delta L = -l_a \sin\tilde{\theta}_1 + l_b \cos\tilde{\theta}_2 \cos\tilde{\theta}_1. \tag{5.7}$$

$$y_0 = l_a \cos\tilde{\theta}_1 + l_b \cos\tilde{\theta}_2 \sin\tilde{\theta}_1. \tag{5.8}$$

$$z_0 = l_b \sin\tilde{\theta}_2. \tag{5.9}$$

Eq. (5.7) to Eq. (5.9) give $\tilde{\theta}_1$, $\tilde{\theta}_2$ and ΔL as follows.

$$\tilde{\theta}_1 = \sin^{-1}\frac{y_0}{\sqrt{\left(l_b\cos\tilde{\theta}_2\right)^2 + {l_a}^2}} - \tan^{-1}\frac{l_a}{l_b\cos\tilde{\theta}_2}. \tag{5.10}$$

$$\tilde{\theta}_2 = \sin^{-1}\frac{z_0}{l_b}. \tag{5.11}$$

$$\Delta L = -x_0 + \sqrt{{l_a}^2 + \left(l_b\cos\tilde{\theta}_2\right)^2 - {y_0}^2}. \tag{5.12}$$

Thus, the required travel distance, ΔL, is calculated. Conversely, when the combine robot travels just ΔL forward, it should be located at a point where the auger spout can be positioned three dimensionally to a target point.

At the beginning, the fiducial marker is searched for. On detection of it, the joint angles θ_1 and θ_2 are calculated according to the basic method. If the unloading auger was positioned at these joint angles, there would be some vertical error between the actual spout position and the target point. This positioning error in vertical direction, Z_{Error}, can also be estimated by Eq. (5.13), after the fiducial marker is first detected.

$$Z_{Error} = \| l_b \sin\theta_2 - z_0 \|. \tag{5.13}$$

If the vertical error is too large, forward travel will be required, while positioning should be performed when the error is sufficiently small. To be more specific, an acceptable error ε is assigned. If Z_{Error} satisfies the inequality (5.14), then the harvester travels ΔL forward, as calculated in Eq. (5.12). Otherwise, positioning is immediately performed according to the values calculated in Eq. (5.4) and Eq. (5.5).

$$Z_{Error} > \varepsilon. \tag{5.14}$$

The modified method is implemented. Figure 5.5 shows the main part of the algorithm.

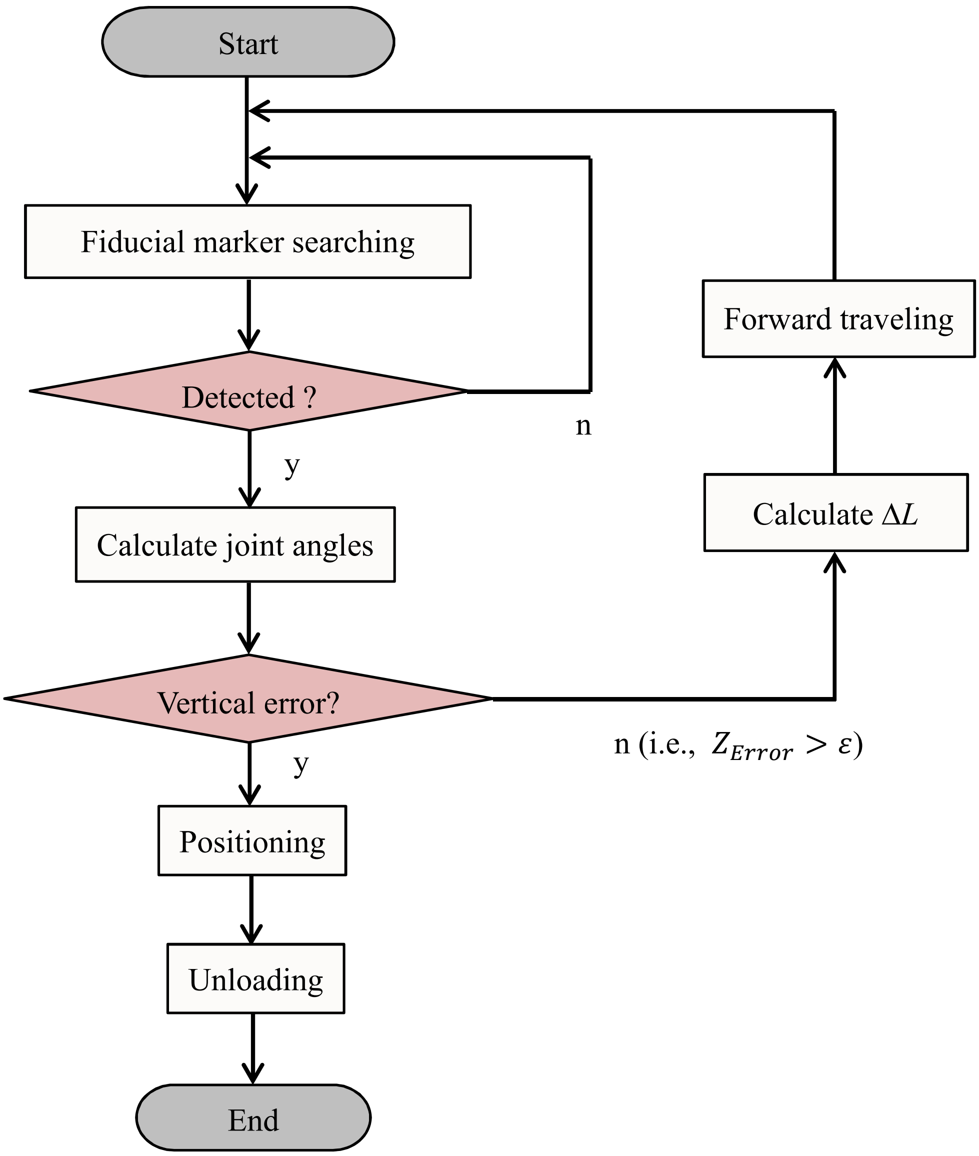

Fig. 5.5. Main flow of autonomous unloading.

The actual travel distance of the combine is estimated as a linear distance between the coordinate of the initial state and that of the present state. They are obtained by RTK-GPS within an accuracy of a few centimeters [8], [9]. When the travel distance reaches around ΔL, the combine stops and the fiducial marker is searched for again.

In practical application, it is difficult both to determine the travel distance with exactness and to stop the combine precisely at the point where it is considered to have traveled just ΔL from the initial state. Thus, $\tilde{\theta}_1$ and $\tilde{\theta}_2$ are utilised only for the calculation of ΔL in Eq. (5.12). The joint angles used for actual positioning should be determined based on the final detection of the fiducial marker. Hence, the fiducial marker searching procedure [7] is newly performed after traveling, which will enable more precise positioning [8]. If there still remains a vertical error despite the forward movement, the algorithm repeats this procedure again, although the iteration is restricted to a maximum of three times.

5.2.2. Results of 3D Positioning

To verify the validity of the 3D positioning method, positioning experiments were performed with the following assumptions. The combine robot is located in a paddy field roughly parallel to a pickup truck that is parked on the farm road adjacent to the paddy. The height of the farm road is around 1.0 m. In the initial state, the fiducial marker, which is placed on the roof of the truck, is located inside the FOV of the auger camera. More precisely, the fiducial marker is at least within the view of the camera attached to the unloading auger, when the algorithm performs the searching procedure.

In the experiment, positioning was performed several times on an asphalt pavement or on a gravel road. In the tests, the relative position between the combine and the fiducial marker was varied. Figure 5.6 shows three resultant trajectories of the combine, which were obtained from the tests carried out on an asphalt pavement. Figure 5.7 similarly represents three exemplar trajectories during the tests performed on a gravel road. These graphs are constructed based on RTK-GPS data, which are recorded at 10 Hz. Each recorded coordinate is appropriately translated and rotated in order that the origin of each graph may correspond to the initial state of the combine before traveling and that the positive direction along the x axis indicates the traveling direction. Thus, in following trajectories, the x axis shows the travel distance and y axis represents the lateral error.

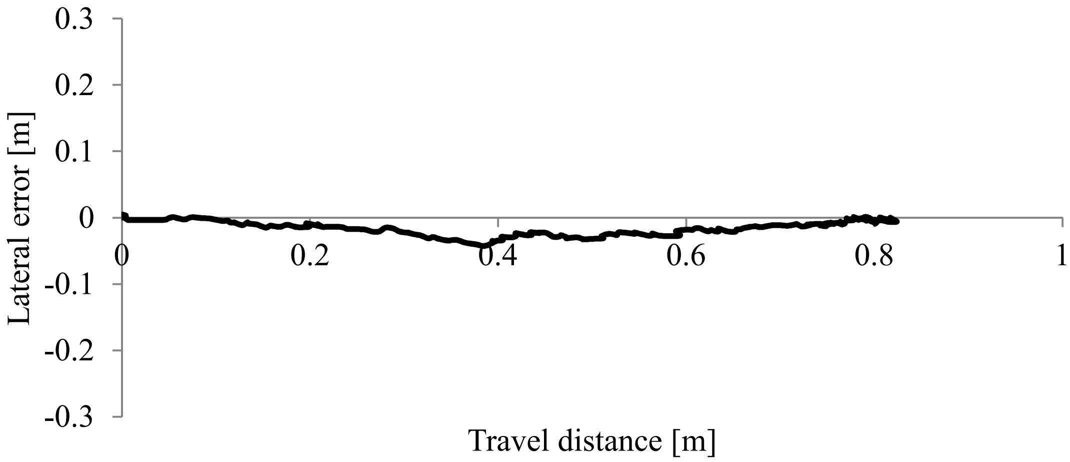

Fig. 5.6. Trajectory of combine robot on asphalt pavement.

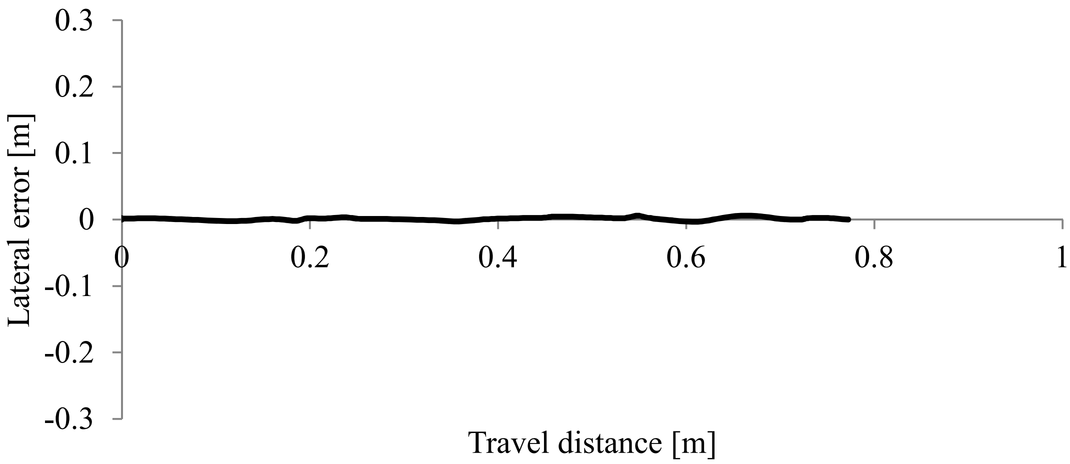

Fig. 5.7. Trajectory of combine robot on gravel road.

Table 5.1. Estimated positioning error in vertical direction, calculated ΔL and actual travel distance.

Test	Before or after traveling	Z_{Error} [m]	ΔL [m]	Travel distance [m]
AP-(a)	before	0.77	0.93	0.00
	after	0.03	-	0.73
AP-(b)	before	1.33	1.53	0.00
	after	0.34	-	1.13
AP-(c)	before	1.17	1.70	0.00
	after	0.12	-	1.31
GR-(a)	before	1.55	1.03	0.00
	after	-0.07	-	0.73
GR-(b)	before	2.02	2.79	0.00
	after	0.05	-	2.41
GR-(c)	before	1.08	1.60	0.00
	after	-0.10	-	1.22

Table 5.1 presents three important values; the vertical error Z_{Error} before and after traveling that was estimated by Eq. (5.13), the required traveling distance ΔL that was calculated according to Eq. (5.12) after the fiducial marker was detected and the actual travel distance of the combine. The tests on an asphalt pavement are named as AP-(a), AP-(b) and AP-(c). Figure 5.6 shows the resultant trajectory of the combine in the case of AP-(a). Similarly, GR-(a), GR-(b) and GR-(c) represent the results obtained on a gravel road. The trajectory of GR-(a) appears in Fig. 5.7.

In the test AP-(a), the Z_{Error} was 0.77 m when the fiducial marker was detected for the first time, which does not satisfy the restriction (5.14). Note that ε was set to 0.5 m in the experiment. Then, the calculated ΔL was 0.93 m. After traveling 0.73 m, the search procedure was performed again. When the fiducial marker was newly detected, the Z_{Error} was reduced to 0.03 m, which is sufficiently less than the acceptable error, ε. Positioning was successfully performed at this location. Also in other tests AP-(b) and AP-(c), the Z_{Error} was reduced from

1.33 m to 0.34 m and from 1.17 m to 0.12 m, respectively. These values satisfy the inequality (5.14).

In the tests GR-(a), GR-(b) and GR-(c), the Z_{Error} was quite close to zero after traveling. This may be because the lateral error of the combine. Table 5.2 presents the maximum lateral error and RMSE from the target path (i.e., x axes in Fig. 5.6 and Fig. 5.7). The tests performed on a gravel road appeared to result in a relatively small lateral error as a whole. Compared to Fig. 5.6, Fig. 5.7 also shows the closer trajectories along the target paths. As described in Section 5.2.1, the modified method assumes that the orientation of the combine remains constant during forward traveling. Whatever the case may be on an asphalt pavement or gravel road, Table 5.2 suggests that the assumptions were reasonable. Especially in the test GR-(c), traveling 2.79 m was required to correct the Z_{Error}. After actually traveling 2.41 m, the indices for the lateral error during this test were still small. This fact also ensures the validity of the assumption in case of relatively longer forward traveling.

Table 5.2. Maximum error and RMSE against target path during traveling.

Test	MAX [m]	RMSE [m]
AP-(a)	0.04	0.02
AP-(b)	0.09	0.03
AP-(c)	0.02	0.01
GR-(a)	0.01	0.01
GR-(b)	0.02	0.01
GR-(c)	0.01	0.01

5.2.3. Homing

The experimental results show that the modified method enables the auger spout to be positioned to a target point not only horizontally but also vertically. There remains another issue to be addressed. As explained in Section 5.2.2, the modified method assumes that the fiducial marker can be observed by the camera when the searching procedure is executed, without the combine needing to travel.

When the grain tank of the combine robot is full, the combine is required to return to the position where it unloads the grain into a grain storage container. Hereinafter, this position is called the *home position* and the combine's return to this position is called *homing*. To be a practical application, the autonomous unloading system needs to include a homing function. A part of this function was also incorporated into the present system and tested in actual field conditions. Figure 5.8 illustrates the homing operation simulated and tested in the field experiments.

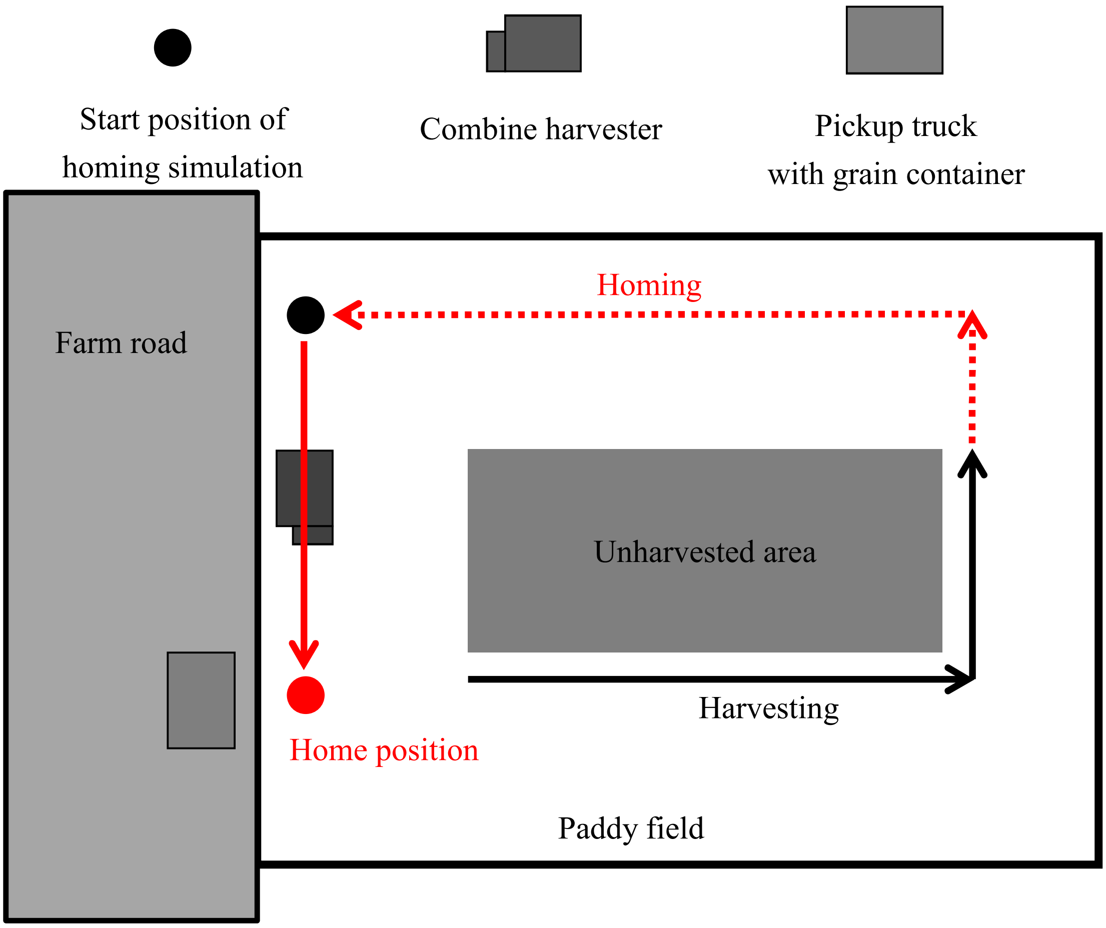

Fig. 5.8. Schematic view of homing operation.

Black arrows indicate the harvesting path. The home position is marked by a solid red circle. Assume that the grain tank of the combine has become full at the end of the black arrow and the combine is returning to the home position along the red line. In the following test, the red continuous line is simulated. The combine harvester starts from the position of homing simulation that is marked by the black circle. The combine robot travels along the target path (i.e., red line) to the home position. When it reaches the destination, the combine stops traveling and the autonomous unloading starts.

5.3. Field Test

The presented methods have been simulated virtually or verified under reasonable assumptions. Finally, these methods must be integrated into an autonomous unloading system, and it must be validated as a whole for the entire actual unloading operation. Consequently, field tests were performed in rice paddy fields. Two different districts were selected as test fields.

The first tests were conducted in a paddy field near Yagi town, Nantan city, Kyoto Prefecture, Japan. It is shown in Fig. 5.9. The test field is enclosed by a black rectangle. The red line indicates the adjacent farm road on which the pickup truck was parked.

Fig. 5.9. Experimental paddy field in Yagi town.

In this field, h_{fr} is 0.9 m. The combine and the truck were parked roughly parallel to each other. In this test, the homing operation was not used and the combine harvester was returned by an operator to the home position. In this state, the autonomous unloading was performed. The speed of the combine was set to 0.3 m/s.

The autonomous unloading system was also demonstrated in another field, an experimental field that is located in the National Agricultural Research Center (NARC), Tsukuba City, Ibaraki, Japan. Figure 5.10 shows the experimental field. h_{fr} is 0.2 m. Also in this test, the combine and the truck were parked roughly parallel to each other.

Fig. 5.10. Experimental paddy field in Tsukuba City.

In this test, homing was performed as described in Section 5.2.3. The speed of the combine was set to 0.4 m/s in the homing operation and to 0.3 m/s in the forward traveling process.

5.4. Results and Discussion

5.4.1. Test in Yagi Town

First, the results in Yagi town are shown. As in Section 5.2.2, the combine's trajectories are shown in Fig. 5.11. Table 5.3 presents the vertical error Z_{Error} before and after traveling, the required traveling distance ΔL, and the actual distance traveled. It also includes maximum error and RMSE against the target path during forward traveling. Rows Y-(a) and Y-(b) in Table 5.3 correspond to Fig. 5.11-(a) and (b), respectively.

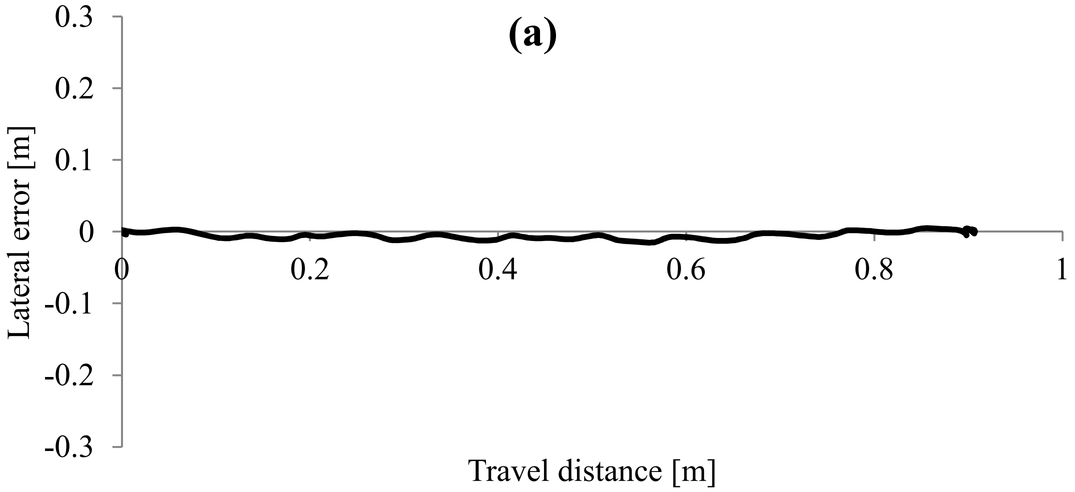

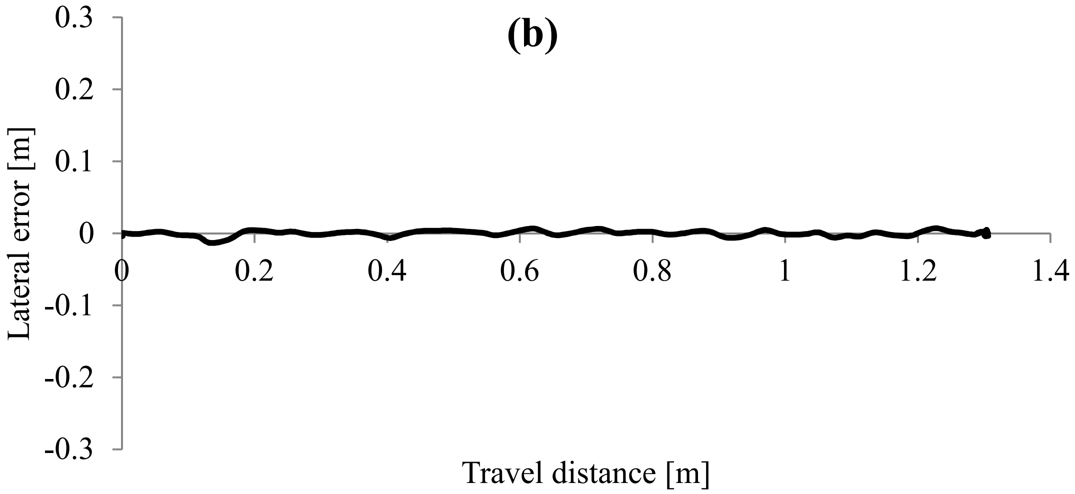

Fig. 5.11. Trajectory of combine robot for autonomous unloading (Test in Yagi town).

In both cases, the indices for lateral error were quite small, which were all less than 0.01 m. They had been expected to be much larger than those shown in Table 5.2, because of the muddy ground in the rice paddy could cause a large lateral error compared to an asphalt or gravel surface. This might be due to the shorter distance traveled, 0.77 m in Y-(a) and 1.16 m in Y-(b). After the combine had travelled forward and the fiducial marker had been detected again, the vertical error was reduced to -0.12 m and -0.28 m in each case, which satisfied the constraint (5.14). Then, the unloading auger was positioned to the target location based on the newly calculated joint angles. Finally, grain was unloaded successfully into the grain storage container without running over the container edges, as shown in Fig. 5.12.

Table 5.3. Estimated positioning error in vertical direction, calculated ΔL and actual travel distance (Test in Yagi town).

Test	Before or after traveling	Z_{Error} [m]	ΔL [m]	Travel distance [m]
Y-(a)	before	0.71	0.96	0.00
	after	-0.12	-	0.77
Y-(b)	before	1.21	1.36	0.00
	after	-0.28	-	1.16

Fig. 5.12. Combine robot unloading grain into grain storage container.

5.4.2. Test in Tsukuba City

Next, the resultant trajectories are similarly shown in Fig. 5.13 concerning the test conducted in Tsukuba City. In this test, homing was conducted as explained in Section 5.4. The black line indicates the trajectory during homing. More precisely, this is the path from the start position of the test to the position near home at which the combine stops traveling (c.f. Fig. 5.8). The red line indicates the trajectory during the forward travel to correct for vertical error.

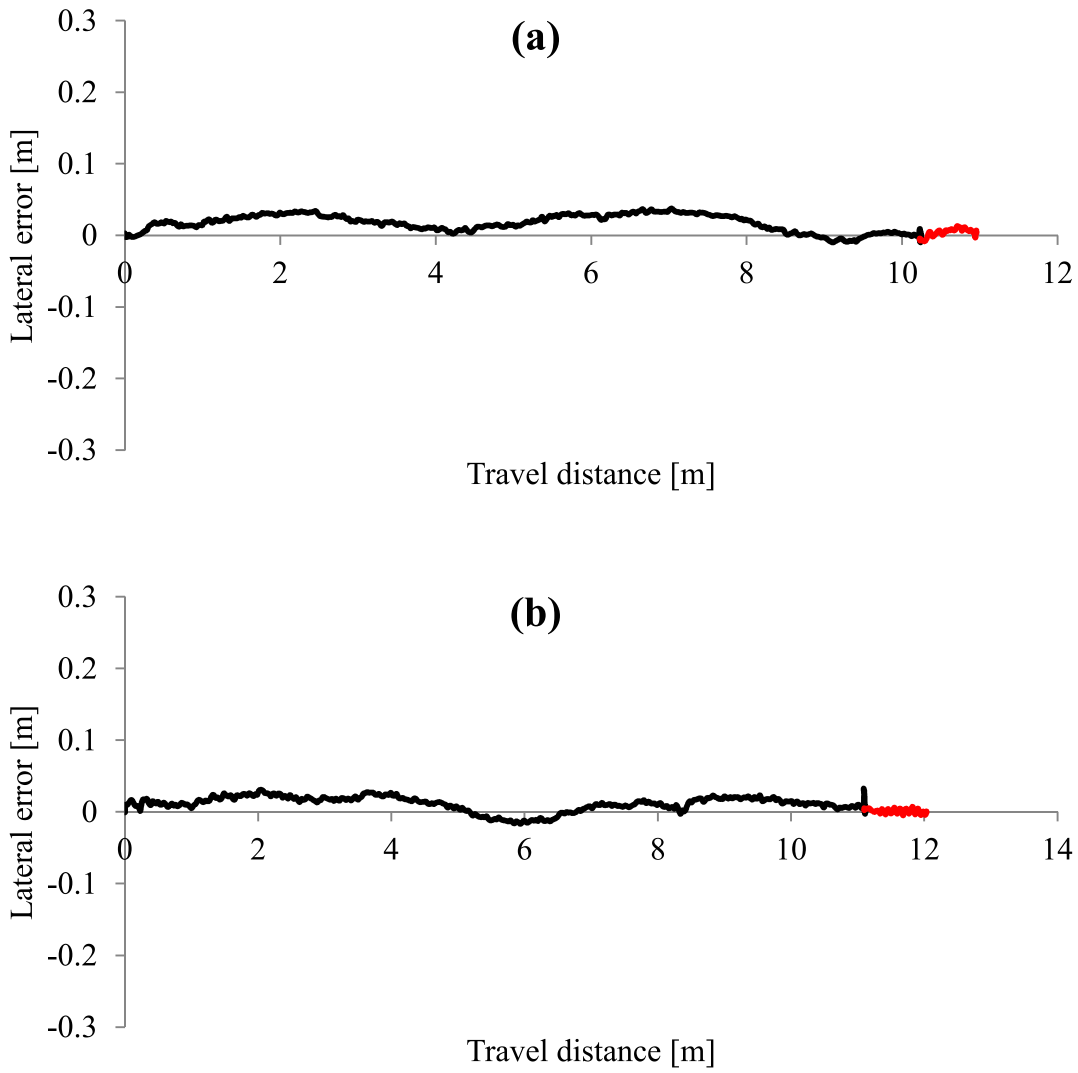

Fig. 5.13. Trajectory of combine robot for autonomous unloading (Test in Tsukuba City).

Table 5.4 also shows Z_{Error}, ΔL, travel distance, maximum error and RMSE. Note that the two indices for the lateral error are calculated based on the data during the forward travel from the home position (i.e., red line in Fig. 5.13). Rows T-(a) and T-(b) represents each result related to the trajectories in Fig. 5.13-(a) and (b).

Table 5.4. Estimated positioning error in vertical direction, calculated ΔL and actual travel distance (Test in Tsukuba City).

Test	Before or after traveling	Z_{Error} [m]	ΔL [m]	Travel distance [m]
T-(a)	before	1.30	0.72	0.00
	after	0.24	-	0.63
T-(b)	before	1.37	0.90	0.00
	after	-0.12	-	0.81

Among tests, the distance from the start position to the home position was varied. In both tests, the combine traveled to the vicinity of the home position and then stopped. After forward traveling, the auger spout was appropriately positioned and grain was successfully unloaded into the grain storage container. Figure 5.14 shows the snapshots of the autonomous unloading operation by the combine robot in Tsukuba City.

The combine starts from an initial position (**a**) and travels until reaching a point near the home position (**b**). At this location (**c**), the searching procedure is performed (**d**). After the fiducial marker is first detected (**e**), the combine travels the required distance ΔL forward (**f**) and the fiducial marker is searched for and detected again (**g**). Since the estimated Z_{Error} is less than the acceptable error ε, positioning is executed (**h**) and then the grain is unloaded (**i**). After unloading, the unloading auger returns to the default position (**j**). The video is also available at http://elam.kais.kyoto-u.ac.jp/misc/Autonomous_grain_unloading.html. In the experiment, the combine robot positioned the auger spout to the target position that the machine vision system determined, and it discharged the grain into the grain storage container without any loss.

Fig. 5.14. Scenery of autonomous unloading system actually working.

5.5. Conclusions

In this study, a machine-vision based method was developed to position the auger spout of the unloading auger to an assigned target point. First, the proposed method calculates the initial joint angles of the combine's unloading auger to position its spout to the target point horizontally. Second, it estimates the vertical error of the spout position from the target point assuming that the positioning would have been performed according to the initial joint angles. In this method, the vertical error is then corrected by the forward travel of the combine. If the estimated error exceeds the acceptable error in the vertical direction, the method estimates the required travel distance to correct the estimated vertical error. The method then calculates the required joint angles in the new position of the combine. The experimental results indicate that the combine positioned its auger spout to the target point and the vertical error was reduced by this method. Thus, the auger spout can be positioned to the target point with sufficient accuracy in three dimensions.

The searching procedure, spout positioning and homing operation were integrated into an autonomous unloading system. Field tests were conducted to examine the performance of this system in two different districts.

In actual rice paddy fields, the combine robot searched and detected the fiducial marker, and traveled forward to reduce estimated vertical positioning error. After positioning the auger spout, the combine robot discharged the grain into the grain storage container, without any loss.

REFERENCES

[1] Inoue, K., Ootsuka, K., Sugimoto, M., Murakami, N. and Li, W: Sensor fusion techniques for automatic guidance by the method of Kalmanfilter using DGPS and gyrocompass (Part 1) (in Japanese). Journal of the Japanese Society of Agricultural Machinery, vol 61, no. 4, 103-113, 1999.

[2] Takai, R., Barawid, O. Jr., Ishii, K. and Noguchi, N: Development of Crawler-Type Robot Tractor based on GPS and IMU, Preprint of the IFAC International Conference on AGRICONTROL 2010, A3-5, Kyoto, Japan, 2010.

[3] Nagasaka, Y., Umeda, N., Kanetani, Y., Taniwaki, K. and Sasaki, Y: Automated rice transplanter using global positioning and gyroscopes. Computers and Electronics in Agriculture, 43(3), 223-234, 2004.

[4] Iida, M., Uchida, R., Zhu, H., Suguri, M., Kurita, H. and Masuda, R: Path-following control for a head-feeding combine robot. Engineering in Agriculture, Environment and Food, Accepted October 12, 2012.

[5] Uchida, R., Iida, M., Zhu, H., Kurita, H., Suguri, M. and Masuda, R: Path following control for head-feeding combine robot. Transactions of the Society of Instrument and Control Engineers. vol. 49, no. 1, 119-124, 2013.

[6] Kurita, H., Iida, M., Suguri, M. and Masuda, R: Application of Image Processing Technology for Unloading Automation of Robotic Head-Feeding Combine Harvester. Engineering in Agriculture, Environment and Food, vol. 5, no. 4, 146-151, 2012.

[7] Kurita, H., Iida, M. and Suguri, M: Development of the automated auger positioning system for unloading work – searching and positioning-. *Proceedings* of the 6th International Symposium on Machinery and Mechatronics for Agriculture and Biosystems Engineering (ISMAB), 322-327, Jeonju, Korea, 2012.

[8] Kurita, H., Iida, M. and Suguri, M: Automated unloading system using image processing for head-feeding combine (in Japanese). *Proceedings* of the 55th Rengo Conference of the Institute of Systems, Control and Information Engineers, 251-255, Kyoto, Japan, 2012.

[9] Kurita, H., Iida, M. and Suguri, M: Automation of unloading work –searching and detecting a grain container and proper positioning of a harvester's spout-. *Proceedings* of the International Conference of Agricultural Engineering (CIGR-AgEng2012), 464-469, Valencia, Spain, 2012.

[10] Kato, H. and Billinghurst, M: Marker tracking and HMD calibration for a video-based

augmented reality conferencing system. *Proceedings* of the 2nd IEEE and ACM International Workshop on Augmented Reality, 85-94, CA, USA, 1999.

[11] Farbiz, F., Cheok, A. D., Wei, Liu., ZhiYing, Z., Ke, X., Prince, S., Billinghurst, M. and Kato, H: Live three-dimensional content for Augmented Reality. IEEE Transactions on Multimedia, vol. 7, no. 3, 514-523, 2005.

[12] Asada, H. and Slotine, J. –J. E: Robot Analysis and Control. Wiley-Interscience Publication, NY, USA, 15-50, 1986.

[13] Paul, R. P: Robot Manipulators. MIT Press, Cambridge, England, 41-81, 1981

[14] Yoshikawa, T: Foundations of Robot Control. Corona Publishing Co., Ltd., Tokyo, Japan, 11-68, 1988.

CHAPTER 6

CONCLUSIONS

6.1. Introduction

In this thesis, the development of an autonomous unloading system for a head-feeding combine robot was discussed. This chapter summarizes the major contributions made by this research and concludes the thesis. Then, several remaining challenges are discussed for future progress of the combine robot.

6.2. Summary of Contributions and Conclusions

A commercialized four-row head-feeding combine harvester was remodeled into a combine robot. It was equipped with a RTK-GPS and a GPS compass as navigation sensors. A VRS system was used to obtain an accurate position of the combine. To control the robot, the software of ECUs was reprogrammed and additional ECUs were newly designed for processing navigation data and control commands, and communicating with a laptop PC. By modification of the speed control mechanism, the combine robot can be fully controlled by the software running on the main PC.

For autonomous harvesting, the combine robot is required to follow a target path and to turn without running over the crop. Thus, a steering controller was designed and a turning algorithm was developed, and then the performance of the path-following algorithm and the turning algorithm were examined in actual trials of rice harvesting. The experimental results show that the combine robot followed the target path with sufficiently small lateral error and heading error, and successfully harvested the rice crop.

A machine vision system was developed for obtaining the relative position between the spout of the unloading auger and the grain storage container. Based on the visual information captured by a USB camera, the system detected a fiducial marker and identified its relative position. The unloading auger was modeled as a 2-DOF manipulator and the target joint angles for positioning were determined by solving an inverse kinematic problem. The acceptable error range for auger positioning was defined. The experiment was conducted to measure the positioning accuracy of the auger spout. The results show that the spout was positioned to the assigned target point with sufficient accuracy, which satisfied an acceptable error range in the horizontal plane.

An efficient fiducial marker searching procedure was identified through the numerical analysis of the auger camera FOV. Based upon a pinhole camera model, the FOV was computed against various sets of decisive parameters for the FOV: namely the camera's elevation angle α, the height of farm road h_{fr} and the joint angles θ_1 and θ_2. The ideal range where the fiducial marker should be to the combine was, at the same time, numerically estimated. If the fiducial marker is detected in such an ideal range, the auger spout is expected to be positioned to the target point that is defined relative to the fiducial marker.

Through the simulation, the optimal angle α was determined, such that the corresponding FOV may provide the largest coverage of the ideal range. An efficient searching procedure was proposed based on the obtained α. Incorporated with the combine control program, the fiducial marker searching and spout positioning algorithm was verified in field experiments. For the whole procedure; searching, detecting and positioning operations, the combine robot required a comparable time to that of manual operation. The results show that the combine robot efficiently searched and absolutely detected the fiducial marker.

The machine-vision-based method was presented by which the auger spout of the unloading auger was positioned to a defined target point, accurate in all three dimensions. In the method, the vertical error was estimated at the state in which the fiducial marker was firstly acquired by the camera. Then, the combine travelled forward just the required distance for reduction of the estimated vertical error. After traveling, the searching procedure was executed again and the vertical error was also estimated. The actual positioning was performed only when the estimated vertical error was less than the acceptable error in vertical direction. The experimental results show that, according to the presented method, the spout was positioned to the target point not only horizontally but also vertically with sufficient accuracy.

The presented techniques were integrated into an autonomous unloading system, and the performance of the presented system was examined in field tests. The combine robot searched and detected the fiducial marker, and then positioned its auger spout to a suitable point for unloading grain once it had travelled forward the required distance. Unloading of the grain was also successfully performed without any loss. After the completion of the unloading, the auger was returned to its default position. A homing operation was also incorporated into the system and the combine robot performed a series of tasks successfully.

6.3. Future Perspective

This thesis presents an autonomous unloading system. The combine robot demonstrated the unloading operation in which the system successfully worked. There are, however, some challenges that remain to be solved for the development of a fully autonomous combine robot, or for the development of more intelligent farming systems. Thus, a brief summary of these challenges and their prospects are presented below for future progress with the combine robot.

1. As described in Chapter 2 and Chapter 5, robotic harvesting and autonomous unloading have been developed. The combine robot autonomously harvests a rice crop and discharges the grain into a grain storage container under actual paddy field conditions. However, these functions work independently. It is absolutely necessary to integrate both of these functions into a fully automated combine robot.

2. In Section 2.3.2, the turning control was explained. The head-feeding combine requires a wide area for turning, and human operators have to manually harvest at least four laps of crops before starting the robotic harvesting. Obviously, this preparation procedure for autonomous harvesting should be reduced or eliminated as far as possible, with the use of a more sophisticated combine robot.

3. The analysis on the auger camera FOV allowed the combine robot to search and detect the fiducial marker efficiently and absolutely. Discussion made in Section 4.3.3, at the same time, suggests the difficulties and limitations of searching by the auger camera. Simulation results indicate that it becomes more difficult for the auger camera to detect the fiducial marker as the height of the adjacent farm road increases. For more a reliable and absolute searching procedure, researchers may be required to review the camera installation itself, such as the position to which the camera is attached, and the posture of the camera.

4. In the autonomous unloading system presented in this thesis, ARToolKit was utilized in the development of the machine vision system. It works with sufficient speed, accuracy and robustness, however, it contains a major drawback. It is essential for the camera in the developed machine vision to acquire the whole fiducial. When there are occlusions or only a partial view of the fiducial marker in the input images, the machine vision cannot identify it. To solve this problem, other image features, such as Speeded-Up Robust Features (SURF) [1] could be helpful. Apart from these planar fiducial methods, a promising direction for object recognition and tracking is 3D model based methods [2]. They are worth exploring for application to autonomous unloading functions in a combine robot.

5. Grain is discharged into the grain storage containers and piles up or mounds (see Fig. 6.1). In general, when a human operator controls the unloading auger the grain is not allowed build up to a pile; the discharge position is moved to disperse the grain. To automate this operation is also a challenge that needs to be addressed for a more intelligent combine robot. In order to automate the dispersion operation, the combine robot will need to obtain 3D information of the discharged grain in the container using, for instance, a range image sensor.

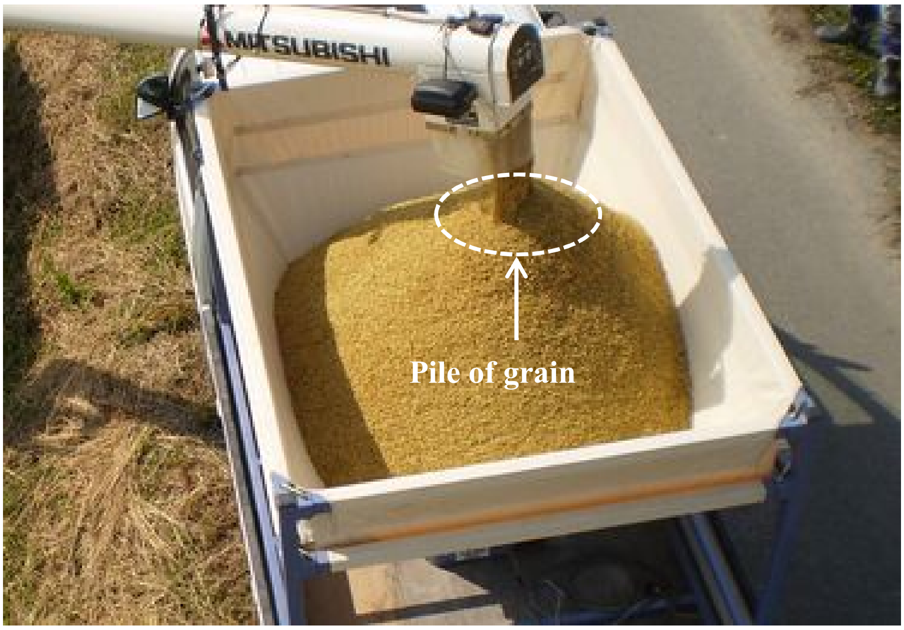

Fig. 6.1. Discharged grain piling up.

6. In the future, with advanced robotic farming systems, as introduced in Chapter 1.2, the dispatch control of transporters will be a critical factor for an efficient and comprehensive system. In actual harvesting, the combine harvester, with its tank full of grain, often has to wait for the transporter to return from the rice processing facility. Even if, in the future, fully autonomous combine robots work effectively in respective paddy fields, the efficiency of the whole harvesting system could be significantly diminished by sub-optimal dispatch control of the transporter.

REFERENCES

[1] Bay, H., Ess, A., Tuytelaars, T. and Gool, L. V: “SURF: Speeded-Up Robust Features”. Computer Vision and Image Understanding, vol. 110, no. 3, 346-359, 2008.

[2] Vacchetti, L., Lepetit, V. and Fua, P: Stable real-time 3D tracking using online and offline information. IEEE Transactions on Pattern Analysis and Machine Intelligence, vol. 26, no. 10, 1385-1391, 2004.